Active Photonic crystal fibers for high power applications

Olausson, Christina Bjarnal Thulin

Publication date:
2011

Document Version
Publisher's PDF, also known as Version of record

Active photonic crystal fibers for high power applications

PhD Thesis
Christina B. Olausson

September 20th, 2010

DTU Fotonik
Department of Photonics Engineering

DTU Fotonik
Department of Photonics
Engineering
Technical University of Denmark
Ørsteds Plads 345
DK-2800 Kgs. Lyngby
Denmark

NKT Photonics A/S
Department of Fiber
Technology
Blokken 84
DK-3460 Birkerød
Denmark

Abstract

The photonic crystal fiber technology provides means to realize fibers optimized for high power operation, due to the large single-mode cores and the unique design flexibility of the microstructure. The work presented in this thesis focuses on improving the properties of active photonic crystal fibers for high power fiber lasers and amplifiers, and on adding new functionality to the fibers – all with the purpose of pushing the technology towards high powers.

The first part of the work has been to investigate photo darkening, the mitigation of which is crucial in the quest for higher powers. The work has contributed to the compounding of new and improved material compositions. The second part is an investigation of pump absorption in photonic crystal fibers, demonstrating that the microstructure in photonic crystal fibers improves the pump absorption by up to a factor of two compared to step-index fibers. This plays an important role in high power lasers and amplifiers with respect to efficiency, packaging, and thermal handling. The third part of the work has involved developing tools for characterizing the mode quality and stability of large core fibers. Stable, single-mode fibers with larger cores are essential to the pursuit for higher powers and the tools have enabled the development of one of the largest and most stable flexible large core fibers on the market. The forth, and largest part of the work, has focused on developing a fiber amplifier with gain shaping for high power amplification at 1178 nm. Several high power records have been set using this fiber. An output power of 167 W has been achieved, which, at the time of writing, is the highest output power generated from ytterbium fibers in this wavelength region and from photonic bandgap fibers in general. The 1178 nm light has subsequently been frequency doubled to 589 nm with high efficiency. Finally, the last part of the work has been the development of the first ever tunable fiber laser based on a liquid crystal infiltrated photonic crystal fiber for operation at 1040–1065 nm.

Resumé (Danish abstract)

Krystalfiberteknologien har gjort det muligt at fremstille fibre, som er optimeret til høje effekter på baggrund af fibrenes store kerner og den designfleksibilitet, der ligger i selve mikrostrukturen. Det arbejde, som præsenteres i afhandlingen, fokuserer på at forbedre egenskaberne ved de krystalfibre, som er beregnet til højeffektlasere og -forstærkere, og på at tilføje ny funktionalitet til fibrene – med det overordnede mål at drive teknologien mod endnu højere effektniveauer.

Den første del af arbejdet har handlet om at undersøge fænomenet photo darkening, eftersom en reduktion af photo darkening er vigtig for at kunne nå højere effektniveauer. Arbejdet har bidraget til sammensætningen af nye og forbedrede materialekompositioner. Den anden del er en undersøgelse af pumpeabsorption i krystalfibre. Undersøgelsen demonstrerer at mikrostrukturen i fibrene forbedrer pumpeabsorptionen med en faktor to i sammenligning med standardfibre, hvilket spiller en væsentlig rolle for højeffektlasere og -forstærkere i forbindelse med effektivitet, pakning og termisk håndtering. Den tredje del af arbejdet har drejet sig om at udvikle redskaber til karakterisering af mode-kvalitet og stabilitet af krystalfibre med store kerner. Stabile, single-mode fibre med store kerner er essentielle i stræben mod højere effektniveauer, og redskaberne har gjort det muligt at udvikle én af markedets største og mest stabile fleksible fibre. Den fjerde – og største – del af arbejdet har fokuseret på udviklingen af en fiberforstærker med gain-shaping til forstærkning ved 1178 nm. Adskillige rekorder er sat med denne fiber – fiberen har blandt andet nået en effekt på 167 W, hvilket, i skrivende stund, er den højeste effekt fra ytterbium-fibre i dette bølgelængdeområde og fra båndgabsfibre generelt. Lyset er efterfølgende blevet frekvensfordoblet til 589 nm med høj effektivitet. Endeligt har den sidste del af arbejde handlet om at udvikle den første fiberlaser nogensinde, som er baseret på flydende krystaller infiltreret i en krystalfibers lufthuller, og som kan tunes i bølgelængdeområdet 1040–1065 nm.

Preface

The work presented in this thesis has been carried out as a part of my Industrial PhD project in the period November 1st, 2007 – October 31st, 2010.

The work mainly took place at NKT Photonics A/S. A two months research stay was spent at the Institute for Laser Science, University of Electro-Communications, Tokyo, Japan.

The project was financed by NKT Photonics and the Danish Agency for Science, Technology and Innovation and was supervised by

- Anders O. Bjarklev, Professor, Dr.Techn., DTU Fotonik, Technical University of Denmark, Kgs. Lyngby, Denmark
- Kim P. Hansen, PhD, NKT Photonics A/S, Birkerød, Denmark

Copenhagen, September 20th, 2010

Christina B. Olausson

Acknowledgements

Doing an industrial PhD project, with one foot at the university and the other foot in industry, has been a great experience with many challenges – both academically and personally. The success of the project is due to a number of people.

First of all, I would like to thank my company supervisor Kim P. Hansen for his invaluable support and input throughout the project period, for his integrity, and for always protecting the academic side of my project but at the same time upholding a good balance with the industry side. When I embarked on the project, I did not expect our very detailed plan to hold out – but I have been proven wrong by his scaringly impressive project planning skills. I would also like to thank my university supervisor Anders Bjarklev for always being encouraging and supportive.

A very special acknowledgement goes to Akira Shirakawa-san in Japan. It has been a privilege to work with Akira over the years, and I am especially grateful for having had the opportunity to go to Japan for two months to perform experiments in his lab. Our successful cooperation is a clear manifestation of the advantages of sharing knowledge and capabilities in science rather than fighting for records.

I would like to thank my fellow industrial PhD students, Danny Noordegraaf and Jens Lyngsø, for lending an ear to frustrations and an occasional car seat to a pair of lazy legs. I would like to thank Thomas Tanggaard Alkeskjold for infecting me with his enthusiasm and good mood across the table, and Kate Bing Bjørn for being a good friend. I would like to thank my boss, Jes Broeng, for creating a good atmosphere and making the Fiber Tech group a great place to work – and for allowing

me to write the thesis a couple of months earlier than scheduled. And I would like to thank Lara Scolari for inspiring team work and good friendship.

I am immensely grateful to my boyfriend, Carsten, for his support especially during the last few months of the project, for indulging me and making it possible for me to finish the thesis just in time before commencing the even bigger project of parenthood. Finally, a very special thought goes to our boy in my belly, who has been my source of discipline and perspective during the writing process.

PhD publication list

Journal publications

1. C. B. Olausson, C. Falk, J. K. Lyngsø, B. B. Jensen, K. T. Terkildsen, J. W. Thomsen, K. P. Hansen, A. Bjarklev, and J. Broeng, "Amplification and ASE suppression in a polarization-maintaining ytterbium-doped all-solid photonic bandgap fibre," Optics Express **16** (5), 13657–13662 (2008).

2. L. Scolari, C. B. Olausson, J. Weirich, D. Turchinovich, T. T. Alkeskjold, A. Bjarklev, and L. Eskildsen, "Tunable polarisation-maintaining filter based on liquid crystal photonic bandgap fibre," Electronics Letters **44** (20), 1189–1190 (2008).

3. A. Shirakawa, H. Maruyama, K. Ueda, C. B. Olausson, J. K. Lyngsø, and J. Broeng, "High-power Yb-doped photonic bandgap fiber amplifier at 1150-1200 nm," Optics Express **17** (2), 447–454 (2009).

4. C. B. Olausson, L. Scolari, L. Wei, D. Noordegraaf, J. Weirich, T. T. Alkeskjod, K. P. Hansen, and A. Bjarklev, "Electrically tunable Yb-doped fiber laser based on a liquid crystal photonic bandgap fiber device," Optics Express **18** (8), 8229–8238 (2010).

5. J. K. Lyngsø, B. J. Mangan, C. B. Olausson and P. J. Roberts, "Stress induced birefringence in hybrid TIR/PBG guiding solid photonic crystal fibers," Optics Express, **18** (13), 14031–14040 (2010).

6. C. B. Olausson, A. Shirakawa, M. Chen, J. K. Lyngsø, J. Broeng, K. P. Hansen, A. Bjarklev, and K. Ueda, "167 W, power scalable ytterbium-doped photonic bandgap fiber amplifier at 1178nm," Optics Express, Optics Express, **18** (16), 16345–16352 (2010).

7. A. Shirakawa, C. B. Olausson, H. Maruyama, K. Ueda, J. K. Lyngsø, and J. Broeng "High power ytterbium fiber lasers at extremely long wavelengths by photonic bandgap fiber technology", invited for publication in Optical Fiber Technology, Issue on Special Fiber Structures and their Applications (2011).

8. C. B. Olausson, K. P. Hansen, and A. Bjarklev "Pump absorption in step-index and photonic crystal fibers", manuscript in preparation (2010).

9. A. Shirakawa, C. B. Olausson, H. Maruyama, K. Ueda, J. K. Lyngsø, and J. Broeng, "High power second harmonic generation at 589 *nm*", manuscript in preparation (2010).

Invited conference contributions

1. K. P. Hansen, C. B. Olausson, J. Broeng, K. Mattsson, M. D. Nielsen, T. Nikolajsen, P. M. W. Skovgaard, M. H. Sørensen, M. Denninger, C. Jakobsen, and H. R. Simonsen, "Airclad fiber laser technology," in Proceedings of SPIE **6873**, paper 687307 (2008).

2. A. Shirakawa, H. Maruyama, K. Ueda, C. B. Olausson, J. K. Lyngsø, and J. Broeng, "30W, 1178nm Yb-Doped Photonic Bandgap Fiber Amplifier," in *Conference on Lasers and Electro-Optics/International Quantum Electronics Conference*, OSA Technical Digest (CD) (Optical Society of America, 2009), paper CThGG3.

3. J. Broeng, C. B. Olausson, J. K. Lyngsø, H. Maruyama and K. Ueda, "Actively Doped Solid Core Photonic Bandgap Fiber," in *Optical Fiber Communication Conference*, OSA Technical Digest (CD) (Optical Society of America, 2010), paper OWK5.

Conference contributions

1. L. Scolari, C. B. Olausson, D. Turchinovich, T. T. Alkeskjold, A. Bjarklev, and L. Eskildsen, "A polarization maintaining filter based on a liquid-crystal-photonic-bandgap-fiber," in Proceedings of *European Conference on Optical Communication ECOC 2008*, paper P.1.10, pp. 19–20 (2008).

2. H. Maruyama, A. Shirakawa, K. Ueda, C. B. Olausson, J. K. Lyngsø, B. Mangan, and J. Broeng, "High-Power Yb-Doped Solid-Core Photonic Bandgap Fiber Amplifier at 1150-1200nm," in *Frontiers in Optics*, OSA Technical Digest (CD) (Optical Society of America, 2008), paper FTuG5.

3. C. B. Olausson, C. Falk, J. K. Lyngsø, B. B. Jensen, K. T. Terkildsen, J. W. Thomsen K. P. Hansen, A. Bjarklev, and J. Broeng, "Amplification and ASE suppression in a polarization-maintaining ytterbium-doped all-solid photonic bandgap fibre," in Proceedings of SPIE **7195**, paper 71950M (2009).

4. P. M. W. Skovgaard, J. Broeng, M. D. Nielsen, T. Nikolajsen, M. H. Sørensen, T. T. Alkeskjold, K. P. Hansen, K. E. Mattsson, S. N. Knudsen, and C. B. Olausson, "Towards 10s of kW fiber lasers based on PCF technology," in *Solid State Diode Laser Technology Review Technical Digest* (2008).

5. C. B. Olausson, K. P. Hansen, A. Bjarklev, "Pump Absorption in Air-clad Step Index and Photonic Crystal Fibres for High Power Applications", in *CLEO/Europe and EQEC 2009 Conference Digest*, (Optical Society of America, 2009), paper CJ1_6.

6. H. Maruyama, A. Shirakawa, K. Ueda, C. B. Olausson, J. K. Lyngsø, and J. Broeng, "1178 nm All Yb-fiber Laser Source Power-scaled by Solid-core Photonic Bandgap Fiber for 589nm Generation," in *CLEO/Europe and EQEC 2009 Conference Digest*, (Optical Society of America, 2009), paper CJ4_2.

7. C. B. Olausson, L. Scolari, L. Wei, D. Noordegraaf, J. Weirich, T. T. Alkeskjold, K. P. Hansen, and A. Bjarklev, "Electrically tunable liquid crystal photonic bandgap fiber laser," in Proceedings of SPIE **7580**, paper 75801D (2010).

8. C. B. Olausson, A. Shirakawa, H. Maruyama, K. Ueda, J. K. Lyngsø, and J. Broeng, "Power-scalable long-wavelength Yb-doped photonic bandgap fiber sources," in Proceedings of SPIE **7580**, 758013 (2010).

9. A. Shirakawa, C. B. Olausson, M. Chen, K. Ueda, J. K. Lyngsø, and J. Broeng, "Power-Scalable Photonic Bandgap Fiber Sources with 167

W, 1178 nm and 14.5 W, 589 nm Radiations," in *Advanced Solid-State Photonics*, OSA Technical Digest Series (CD) (Optical Society of America, 2010), paper APDP6.

10. C. B. Olausson, A. Shirakawa, M. Chen, J. K. Lyngsø, J. Broeng, K. P. Hansen, A. Bjarklev, and K. Ueda, "167 W, 1178 nm Ytterbium-Doped Photonic Bandgap Fiber Amplifier with Power Scalability," in *Conference on Lasers and Electro-Optics*, OSA Technical Digest (CD) (Optical Society of America, 2010), paper CTuC2.

11. E. Coscelli, F. Poli, D. Passaro, A. Cucinotta, S. Selleri, C. B. Olausson, L. Leick, J. Broeng, "Bending-Induced Single-Mode Behaviour of a Polarizing Double-Clad Yb-Doped Photonic Crystal Fiber," in Proceedings of *European Conference on Optical Communication ECOC 2010*, paper P1.07 (2010).

Other publications

1. C. B. Olausson, J. K. Lyngsø, H. Marukami, A. Shirakawa, "Photonic bandgap fiber reaches for the stars," World News article in Laser World Focus, http://www.optoiq.com/index/display/article-display.articles.optoiq2.photonics-technologies. technology-products.fiber-optics.communications-systems.2009.12.fiber-amplifiers-photonic-bandgap-fiber-amplifier-reaches-for-the-stars.html.

Contents

Chapter 1

Introduction

Guiding light inside a hair-like strand of glass is a concept that was first put into use in the 1950s, although the idea of guiding light by refraction was demonstrated in water in the nineteenth century. With the advent of the internet the development of the optical fiber technology has progressed rapidly during the past 40 years.

As a bi-product from the exploding telecom industry in the late 1990s, the photonic crystal fiber was developed. The photonic crystal fiber is a general term for a class of optical fibers in which the waveguiding is due to microstructuring of the fiber cross section, typically airholes running along the length of the fiber. The technology was initiated by the wish to put the photonic bandgap technology into fiber form. The concept of controlling the emission of light by the photonic bandgap effect was suggested in 1987 independently by John [1] and Yablonovitch [2] and the idea was experimentally realized in optical fibers more than ten years later in 1998 by Russell and co-workers [3]. Russell and co-workers also introduced the use of airholes as a means of index control a couple of years earlier as they demonstrated the first index-guiding photonic crystal fiber in 1996 [4].

In the early days, at the peak of the telecom boom, the focus of photonic crystal fiber development was on nonlinear, dispersion compensating and large core fibers for communication purposes. Today, however, most of the development has moved into the field of fiber lasers and amplifiers. As the field expands and new applications emerge – for example, in material processing and in defense industry – good beam quality and increasingly

high power levels are required. Due to the large single-mode cores and unique design flexibility of the microstructure, photonic crystal fibers has become very attractive for high power lasers and amplifiers. The first photonic crystal fiber based laser was reported in 2000 [5] and since then a large number of high-performance laser and amplifier systems has been developed using the technology. A few of the most recent achievements are found in [6–12].

The work presented in this thesis has embraced a wide range of topics within the growing field of active photonic crystal fibers. The work focuses on improving the properties of active photonic crystal fibers for high power fiber lasers and amplifiers, and on employing new functionality in the fibers – all with the purpose of pushing the technology towards high powers. Nonlinear effects are some of the main limiting factors for high power fiber lasers and amplifiers and as nonlinear effects depend on length and core size, it is critical to optimize these parameters. Thus, the overall task has been to pave the road towards larger cores and shorter fibers by investigating photo darkening, building up test systems for characterizing and improving large core fibers, and employing new features, such as filter function, in the fibers.

The active photonic crystal fibers studied in this thesis are all realized with ytterbium-doped cores. Ytterbium-doped fibers, however, are known to suffer from photo darkening, which is a pump induced loss mechanism resulting from high doping concentration [13, 14]. The mitigation of photo darkening is crucial in the pursuit for higher powers, since high doping concentrations may be required to reduce nonlinear effects through shorter fiber lengths, and – more importantly – since industry requires good long-term reliability of the fibers. Part of the work in this thesis has been to investigate photo darkening with the aim of developing a procedure for benchmarking fibers in order to compound new and improved material compositions. The work is presented in chapter 4.

Furthermore, efficient pump absorption is required in order to ensure the shortest possible fiber length. It has been suggested that the microstructure in photonic crystal fibers improves the pump absorption compared to standard fibers. A part of the work in this thesis has been to investigate the effect of the microstructure on the pump absorption [15] as

this plays an important role in high power lasers and amplifiers with respect to efficiency, packaging and thermal handling. The work is discussed in the first section of chapter 5.

Besides shorter fibers, reduction of nonlinearities also entails larger core sizes. Moreover, many applications require a stable, diffraction-limited output – for example, for frequency conversion. Obtaining stable fundamental mode operation in some of the largest flexible fibers on the market – fibers with core sizes up to 40 μm – has been a part of the work in this thesis. The work is described in the last part of chapter 5 and has involved developing methods and setups for characterizing and optimizing design parameters of large core fibers with focus on beam quality, stability and bending properties.

Photonic crystal fibers can also include filter functions due to the photonic bandgap effect. For example, combining a doped core with a photonic bandgap structure enables gain shaping and filtering of amplified spontaneous emission and nonlinear effects. Work on fibers with filters is the subject of chapter 6. The largest part of the work in this thesis has been the development of a high power photonic bandgap fiber amplifier with built-in gain shaping for operation at 1178 nm and subsequent frequency doubling to 589 nm – a wavelength of interest for various medical applications, for high-resolution spectroscopy and for laser guide star applications [12, 16].

Finally, a second filtering concept has been tested, which involves infiltrating the airholes of an index-guiding photonic crystal fiber with high-index liquid crystals and thereby giving rise to guidance by the photonic bandgap effect in a part of the fiber. The liquid crystals exhibit large electro-optic effects, thus by applying an electric field to the liquid crystal infiltrated fiber inside a laser cavity, the bandgap properties can be changed, resulting in laser tunability in the wavelength region 1040–1065 nm. This device holds potential as a low-cost tunable seed source for ytterbium fiber amplifiers.

Chapter 2

Photonic Crystal Fibers

Photonic crystal fibers (PCFs) is a general term for a class of optical fibers that are made of a microstructured arrangement of material distributed in a background material of a different refractive index. A typical PCF is made from silica with a hexagonal arrangement of airholes running along the length of the fiber. The material arrangement in the fiber is not restricted to a crystal-like pattern, thus, the term microstructured fiber might be more accurate. However, for historical reasons the acronym PCF is used in this thesis.

PCFs are divided into two subclasses: index-guiding PCFs and photonic bandgap (PBG) fibers. Index-guiding PCFs guide light in a solid core by the principle of modified total internal reflection, similar to conventional fibers. The total internal reflection is enabled by the lower effective cladding index arising from the airholes. PBG fibers constitute the subclass of PCFs in which light is guided by the PBG effect. The PBG effect makes propagation in the microstructured cladding impossible in certain wavelength regions thus light can be guided in a low-index core.
Due to the relatively large refractive index contrast between glass and air, and due to the structural flexibility of the airhole arrangement, the optical properties of PCFs can be controlled by the designer to a much larger extent than in standard fibers. This opens a door to a wide range of unique guidance properties as well as the possibility to improve conventional fiber properties. For example, extremely small or extremely large mode areas are possible as well as single-mode guidance over a very wide range of wavelength regions.

In this chapter the fundamental properties of PCFs, such as the waveguiding mechanism, the criterion for single-mode operation, and the polarization properties, will be introduced and compared to the properties of standard step-index fibers. Furthermore, the advantages of airclad fibers over traditional double-clad fibers for high power applications will be discussed.

2.1 Index-guiding photonic crystal fibers

In a standard step-index fiber a mode is confined to a high-index core by total internal reflection at the core-cladding interface. A schematic drawing of a typical step-index fiber is shown in 2.1, where a is the core radius. In a step-index fiber the cladding material is pure silica, while the core is typically made of germanium-doped silica, restricting the core-cladding refractive index contrast to $\sim$0.05.

Index-guiding PCFs consist of a doped or undoped silica core region surrounded by a microstructured arrangement of airholes, which in most cases are organized in a periodic hexagonal lattice. Figure 2.2 shows a schematic drawing of a typical PCF cross section. The cladding structure is defined by the hole diameter, d, the pitch, Λ, which is the inter-hole distance, and the number of airholes, expressed by the number of airhole "rings" around the core. A larger core area can be introduced by omitting more than one central hole, and the core size is therefore defined by both Λ, d, and the number of missing holes. The microscope images in figure 2.3 show two types of photonic crystal fibers made possible by the microstructuring process. Image (a) is a large-mode-area (LMA) fiber and (b) is a highly nonlinear fiber, both of which are index-guiding but with very different properties.

Waveguiding properties

The waveguiding properties of the PCF is quite different from those of a standard fiber and need to be treated numerically for an accurate description. Literature suggests that the effective index is extracted from the periodic lattice surrounding the core and is in fact a special case of bandgap guidance [17]. The effective refractive index is equivalent to the index of the lowest order mode that can propagate in the cladding, also known as the

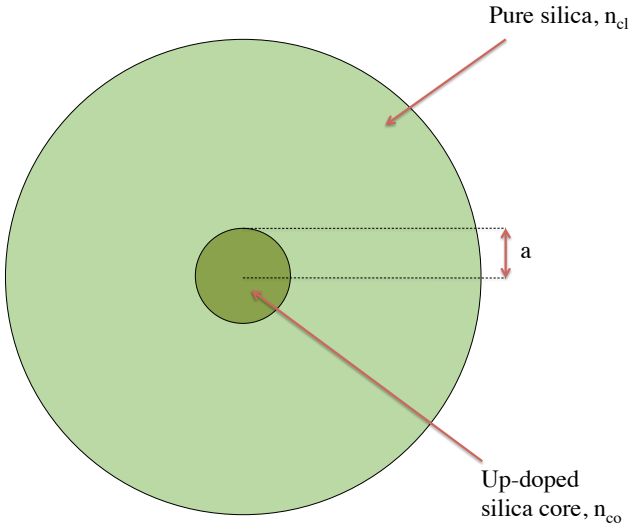

Figure 2.1: Cross section of a standard silica fiber with an up-doped core. The main design parameters in standard step index fibers are the core radius, a, the core index, n_{co}, and the cladding index, n_{cl}.

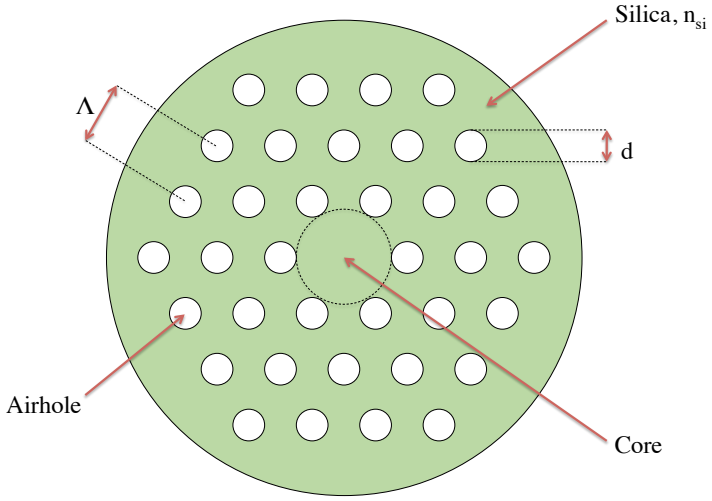

Figure 2.2: Cross section of a silica PCF. The main design parameters in PCFs are the hole diameter, d, the pitch, Λ, and the index of the background material, n_{si}. The core is realized by omitting one or more central holes.

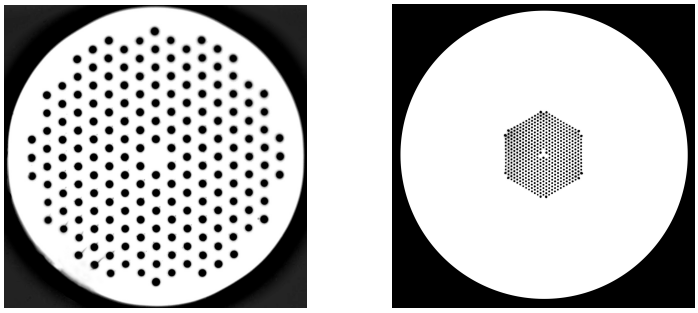

(a) (b)

Figure 2.3: Microscope images of (a) a large mode area fiber and (b) a highly nonlinear fiber.

fundamental space filling mode (FSM) [18]. The effective index is defined as

$$n_{eff} = \frac{\beta_{FSM}}{k}, \tag{2.1}$$

where β_{FSM} is the propagation constant of the fundamental space filling mode and $k = 2\pi/\lambda$ is the free-space wave number. Modes that are supported by the core must obey the following relation

$$n_{eff} < \beta/k < n_{co}, \tag{2.2}$$

where β is the propagation constant of the guided mode. By analogy with a standard fiber, the effective index value can be used for the cladding index to predict a number of basic properties of index-guiding PCFs such as the cut-off wavelength and the number of guided modes.

The guidance mechanism in index-guiding PCFs can also be understood qualitatively by considering the behavior of the optical field in different fiber designs. If the PCF is designed with very small airholes or is operated in the long-wavelength region such that $\lambda \gg d$, the optical field in the cladding region is only weakly affected by the individual airholes. In this case the cladding can be approximated by a homogeneous material with an index defined by the area average of the index of air and silica. However, for shorter wavelengths or larger holes where $\lambda \sim d$ the field will move out of the airholes and into the cladding region. This will increase the effective index and thus reduce the index difference between core and cladding. It

is this wavelength dependence of the effective refractive index that makes PCFs so fundamentally different from standard step-index fibers.

Single-mode operation

With a core size, a, core index, n_{co} and cladding index, n_{cl}, the number of guided modes in the core of a step-index fiber is determined by the V-parameter,

$$V_{SI} \equiv \frac{2\pi a}{\lambda} NA, \tag{2.3}$$

where λ is the wavelength of the light. NA is the numerical aperture which follows from Snell's law of refraction [19] and is given by

$$NA = sin(\theta) = \sqrt{n_{co}^2 - n_{cl}^2}, \tag{2.4}$$

where θ is the acceptance angle of the fiber. The fiber is single-mode provided that equation 2.3 yields a value smaller than 2.405 [18, 20]. The index step between core and cladding can only be controlled with a finite precision in a step-index fiber, thus single-mode behavior in step-index fibers is limited to core sizes around 15 μm at a wavelength around 1 μm.

The single-mode criterion for an index-guiding PCF is different from that of the step-index fiber. An effective V-parameter can also be defined for a PCF [18, 21],

$$V_{PCF} \equiv \frac{2\pi\Lambda}{\lambda} \sqrt{n_{co}^2 - n_{eff}^2}, \tag{2.5}$$

where n_{co} in most cases is the index of silica. However, single-mode operation will not be defined by V_{PCF} larger than 2.405 as for the step-index fiber. Due the wavelength dependence of the effective index, n_{eff}, it is no longer evident that the fiber will become multimoded in the short-wavelength limit. In fact, as $\Lambda/\lambda \to \infty$, V_{PCF} approaches a finite value. It has been shown numerically that if this asymptotic value of V_{PCF} is smaller than π the fiber is single-mode [20]. This is in contrast to a step-index fiber where $V_{SI} \to \infty$ as $\lambda \to 0$, resulting in multimode operation.

The single-mode range of the PCF is analyzed by considering the relative hole size, d/λ. If d/λ increases, more higher-order modes will be guided and as a consequence the number of guided modes can be determined solely by the cladding geometry, independent of wavelength and

core diameter. It has been shown that when d/Λ is smaller than $\sim$0.41 the PCF is single-mode at all wavelengths [20], however for many practical purposes, fibers with $d/\Lambda < 0.45$ can be regarded as single-mode at all wavelengths. Since the single-mode criterion is only dependent on d/Λ, the pitch can in principle be scales to any value and theoretically the core can become arbitrarily large, only limited by bending losses [18]. In reality the limitations to the core size are defined by macro- and micro-bending losses [22–25], where macro-bending losses are related to actual bending of the fiber and micro-bending losses are a result of microscopic disturbances in the fiber caused by fabrication imperfections or externally applied stress.

In most cases PCFs are designed such that they are not endlessly single-mode, but only single-mode in the wavelength range of operation. An important characteristic of a fiber is the cut-off wavelength which determines the wavelength above which the fiber behaves as a single-mode fiber. The cut-off wavelength is usually defined as the wavelength at which the ratio of the total power to the fundamental mode power is 0.1 dB. According to this definition the second-order mode undergoes 19.3 dB more attenuation than the fundamental mode [26]. Several techniques for measuring the cut-off exist, the most common ones being the bend reference technique and the multimode reference technique [27]. Recently, a method using spatially resolved spectral interferometry has been developed [28].

When the core size of the fiber is increased, the spacing between modes in the fiber decreases accordingly. Although direct scaling of all dimensions of a PCF is theoretically feasible, the decrease in mode spacing makes the fabrication tolerances increasingly tighter. The fiber becomes more sensitive to nonuniformities in the index profile and it becomes much more difficult to achieve a sufficiently small index step to prevent higher order modes. In addition, due to the smaller index step, the guiding in these fibers becomes relatively weak, making the fibers more sensitive to bend losses.

In some cases strictly single-mode operation in large core fibers is not necessary. Instead it is possible to use fibers which support a few transverse modes. Typically, higher-order modes exhibit higher bend-induced loss compared to the fundamental mode, and thus bending of these fibers is often used to suppress higher-order modes from propagating [29]. When

bent, a few-moded fiber behaves effectively single-mode. Alternatively, the fiber can be designed with an extremely thick outer cladding such that it becomes unbendable and thus more insensitive to macro-bending losses. A mechanically stable large core fiber resistant to bending losses is found in the rod-type fiber design, which has an outer diameter in the range of a few millimeters and a strongly reduced fiber length. The largest rod-type fiber at present features a 100 μm core [10, 11].

2.2 Photonic bandgap fibers

Photonic bandgap (PBG) fibers is the subclass of PCFs which guide light in a low-index core by the photonic bandgap effect. It can be shown that in a two-dimensional array of scatterers, light propagation in certain wavelength intervals can be inhibited by interference effects, provided that the index contrast between the background material and the scatterers is sufficiently large, essentially like a two-dimensional Bragg mirror. These wavelength intervals are called photonic bandgaps. If the periodicity of the scatterers is broken, for example, by removing a single scattering point, modes with frequencies within these photonic bandgaps may be trapped in the defect – the core. The spectral position of the photonic bandgaps can be modelled based on the periodicity of the cladding structure [30].

There are two different types of photonic bandgap fibers, the hollow core fiber and the solid core PBG fiber. In figure 2.4 the cross section of a hollow core fiber is illustrated. In a hollow core fiber light is guided in air and the main design parameters are the cladding pitch, Λ, the air filling fraction, defined by the thickness of the silica bridges separating the airholes, and the index of the background material, n_{si}. In figure 2.5 the cross section of a solid core PBG fiber is illustrated. The main design parameters are the size of the high-index rods, d, the pitch, Λ, the index of the background material, n_{si}, and of the high-index material, n_{hi}. The core is realized by replacing one or more high-index rods in the central region with silica. The microscope images in figure 2.6 show the two types of photonic bandgap fibers, where image (a) is a hollow core fiber and (b) is a solid core PBG fiber.

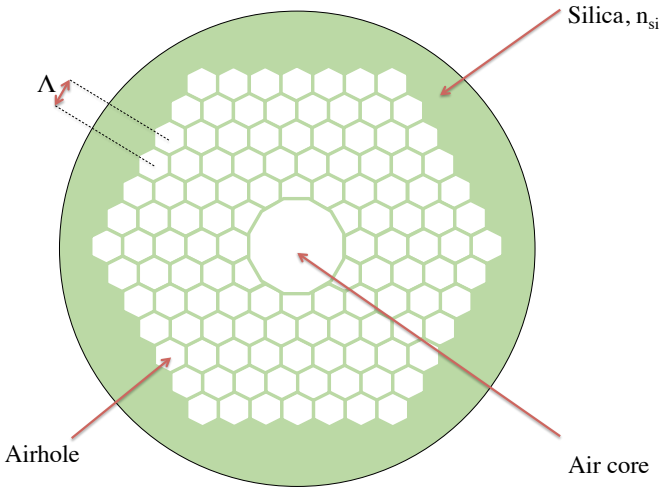

Figure 2.4: Cross section of a hollow core fiber. The main design parameters in hollow core fibers are the cladding pitch, Λ, the air filling fraction, defined by the thickness of the silica bridges separating the airholes, and the index of the background material, n_{si}.

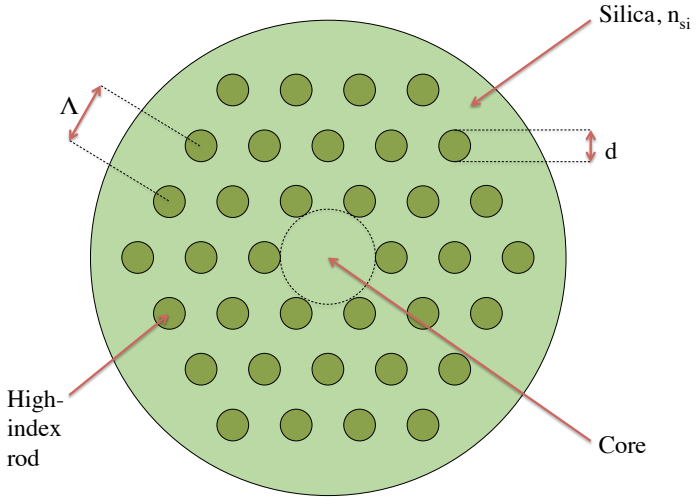

Figure 2.5: Cross section of a solid core PBG fiber. The main design parameters are the diameter of the high-index rods, d, the pitch, Λ, the index of the background material, n_{si}, and of the high-index material, n_{hi}. The core is realized by omitting one or more central high-index rods.

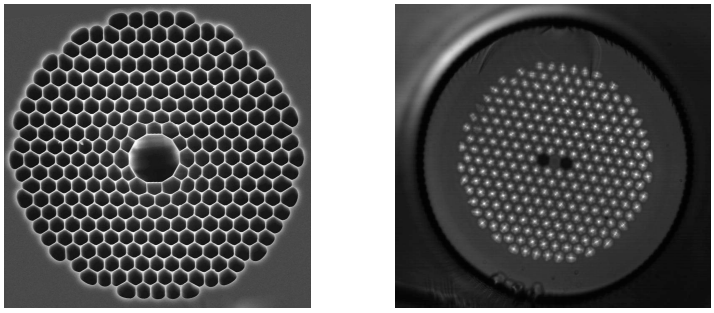

(a) (b)

Figure 2.6: Microscope images of (a) a hollow core fiber and (b) a solid core photonic bandgap fiber.

Antiresonant reflecting optical waveguide model

The confinement mechanism of solid core PBG fibers can also be understood in terms of antiresonant reflections in the individual high-index rods, where periodicity is not a prerequisite. Thus, the much simpler antiresonant reflecting optical waveguide (ARROW) model can be used to identify the spectral position of the bandgaps [31, 32]. According to the ARROW model the m^{th} minima in the transmission spectrum is given by

$$\lambda_m = \frac{2d}{m + \frac{1}{2}} \sqrt{n_{hi}^2 - n_{si}^2}. \tag{2.6}$$

At these wavelengths the refractive index of the cladding approaches the refractive index of silica, the entire structure becomes transparent and light can therefore no longer be guided in the core. According to equation 2.6 the spectral position of the bandgaps can varied e.g. by changing the diameter of the high-index rods. An example of a transmission spectrum of a 18 mm long solid core PBG fiber is shown in figure 2.7. The diameter of the high-index rods is 7.7 μm and the indices are $n_{hi} = 1.4773$ and $n_{si} = 1.4483$. The transmission minima calculated from the ARROW model are included in the figure as the red dashed lines. The small deviations between model and measurement may be due to the fact that the fiber is not infinitely short and that the high-index rods have a parabolic index profile rather than a step-index profile.

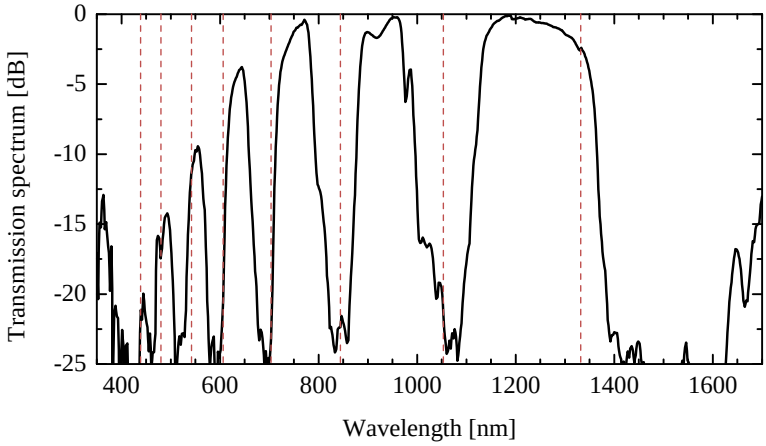

Figure 2.7: Transmission spectrum of a 18 *mm* long solid core PBG fiber. The red dashed lines are the transmission minima calculated from the ARROW model.

2.3 Polarization properties

In most single-mode fibers – both PCFs and standard step-index fibers – there are two degenerate modes with orthogonal polarization due to the symmetry of the cladding structure. However, all fibers exhibit some degree of internal birefringence and as a consequence the polarization of light propagating in the fibers will change in an uncontrolled manner. This means that when polarized light is launched into a fiber the polarization is generally not preserved due to this random coupling between the two polarization states caused by even the smallest external perturbations and imperfections in the symmetry. This phenomenon is known as polarization mode dispersion. In order to avoid coupling between the two polarization states, a fiber can be designed such that the two polarization modes have different propagation constants and are no longer degenerate.

The polarization properties originate from birefringence in the fiber, which can be controlled by incorporating so called stress applying parts in the fiber design. The idea is to create a birefringence in the fiber which is larger than the internal birefringence due to symmetry imperfections.

The stress rods are made of a modified glass composition with a different degree of thermal expansion in the preform compared to pure silica. The stress rods used in PCFs are typically doped with B_2O_2 and are places on opposite sides of the core. The expansion properties of boron makes the material shrink more than the surrounding silica, when the fiber is drawn and thus freezes the core in tension. This tension induces the two different indices of refraction in the core, the higher index parallel and the low index perpendicular to the applied stress. Light polarized along the direction with the lower index travels faster and thus this axis is termed the fast axis. The other axis is the slow axis.

When the fiber no longer supports coupling of light between the two polarization states, the fiber is said to be polarization-maintaining. Figure 2.8 illustrates the cross section of a polarization-maintaining solid core PBG fiber design with a stress rods on either side of the core. Polarization-maintaining fibers require polarized input in an amplifier configuration and in laser configuration, one cannot be certain that there is enough preferential gain to ensure lasing in only one of the polarization directions. These limitations are eliminated in the single-polarization or polarizing fiber which is designed such that only one of the two polarization states is supported, while the fiber is a leaky waveguide for the other polarization. In these fibers the cut-off wavelength is polarization dependent and in many cases, single-polarization guidance occurs in only a limited wavelength range. Figure 2.9 illustrates the cross section of a polarizing fiber design, where several holes have been substituted by stress rods. Combining large core fibers with high-birefringence designs one can obtain polarizing fibers with a bandwidth, where the fibers act as traditional polarization-maintaining fibers for wavelengths longer than the polarizing cut-off. Figure 2.10 shows the polarization properties of a polarizing, high NA, LMA fiber. The polarization properties are controlled by the exact bending radius and orientation of the fiber.

The better the polarized light is launched into either the fast or slow axis, the better the polarization is maintained and controlled within the system. Misalignment even by a small angle with respect to one axis, will cause a small amount of light to be transmitted along the other axis. Therefore, there will always be some residual random polarization present in the output light. To measure the quality of the polarized output from

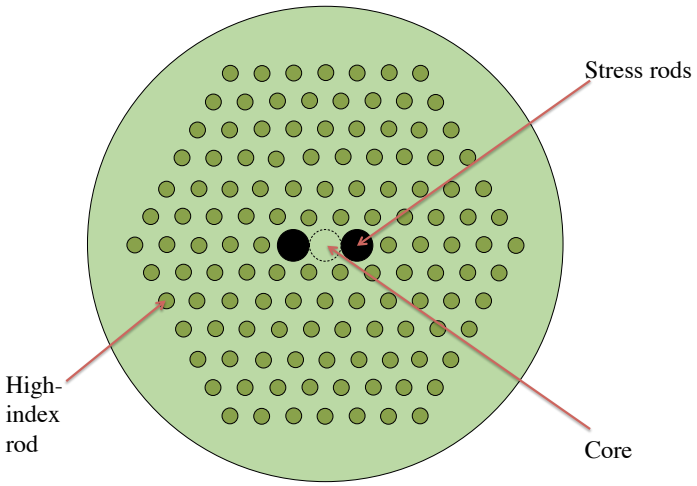

Figure 2.8: Cross section of a polarization maintaining solid core PBG fiber where two high-index rods on either side of the core have been substituted with stress rods.

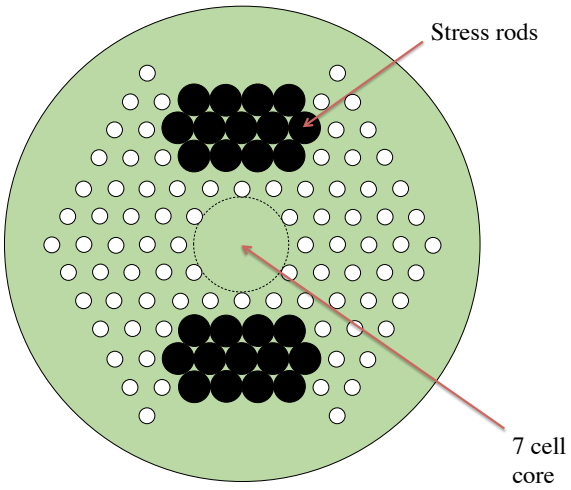

Figure 2.9: Cross section of a polarizing LMA fiber, where several of the holes have been substituted by stress rods.

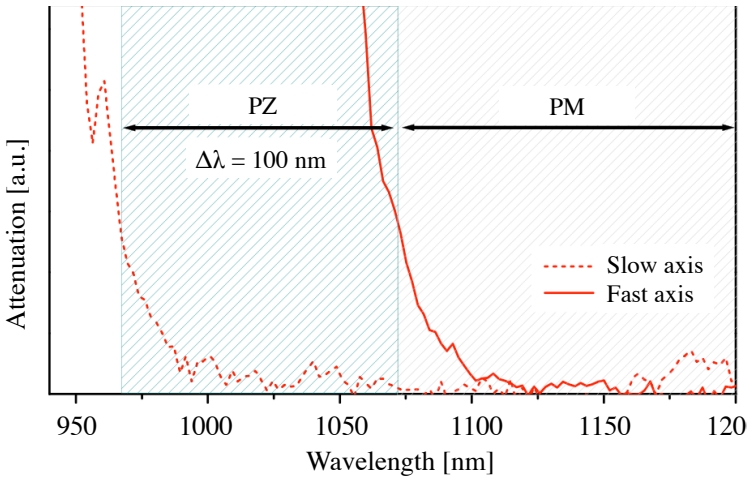

Figure 2.10: Polarization properties of a large mode area, high NA, airclad fiber containing stress applying part for polarization control. The polarization properties are controlled by the exact bending radius and the orientation of the fiber.

a fiber one must measure the polarization extinction ratio (PER) [33]. Whereas birefringence is a design parameter of the fiber, the PER is a measure of the quality of the polarized light from the fiber, not exclusively depending on the internal birefringence. The PER measures the extent to which an originally pure polarization state has been degraded, based on the ratio between the optical power in the two polarization states. There is some confusion in the fiber community as to whether the term PER can be used for polarization-maintaining fibers or should be reserved for polarizing fibers only. The term polarization cross talk (PCT) is preferred by some for polarization-maintaining fibers, however, the measurement procedure for the two types of fibers is identical, and the term PER will be used for all types of birefringent fibers in this thesis.

2.4 Airclad fibers

Traditional active fibers, like those used for telecommunication amplifiers, are preferably pumped with single-mode pump lasers directly in the signal core. The power limitations of single-mode pump sources make this type of fiber unsuitable for high power applications. Consequently, high power

fibers are designed with a double-clad structure, where a second low-index region acts as cladding for a large multimode pump core. Thus, the cladding immediately surrounding the core serves both as a waveguide for the pump light and as cladding for the active core. The major advantage of the double-clad design over the more traditional core pumped variety, is the large pump area and high NA, enabling pumping with low-cost multimode diodes [34].

An illustration of the cross section of a typical double-clad fiber is shown in figure 2.11. Standard double-clad fibers utilize a low-index polymer coating to create the cladding for the pump core. The obtainable refractive index of the polymer limits the NA of the fiber – in practice to below 0.48 – which in turn limits the pump power absorption per fiber length and thereby how short a fiber laser can be made. Moreover, the polymer material itself poses a challenge in high power systems due to the risk of degradation at high pump powers and elevated temperatures [35, 36].

The PCF equivalent to the double-clad fiber is the airclad LMA fiber shown in figure 2.12. The fiber consists of an LMA structure with an active, doped core placed inside an airclad pump guide, which is a ring of closely spaced airholes [37]. Due to the large index contrast between air and silica, the airclad can provide very large NA determined by the bridge width of the airclad as shown in figure 2.13. Consequently, the NA is only limited by the practical handling of the fibers where cleaving of the fibers becomes increasingly challenging at NAs above 0.6 – the exact limit depends on fiber design and cleaving equipment, and can, for some designs, be as high as 0.7 while still maintaining good cleavability.

Moreover, as the fiber is all-glass, the thermal handling is greatly improved compared to polymer-clad fibers, and there is no material degradation [38]. The power density is only limited by the damage threshold of silica.

The combination of a very large mode field diameter and high NA makes it possible to create lasers and amplifiers with very short fiber lengths, drastically reducing the unwanted nonlinear effects and making PCFs very attractive for high power lasers and amplifiers. Microscope images of a typical airclad PCF is shown in figure 2.14.

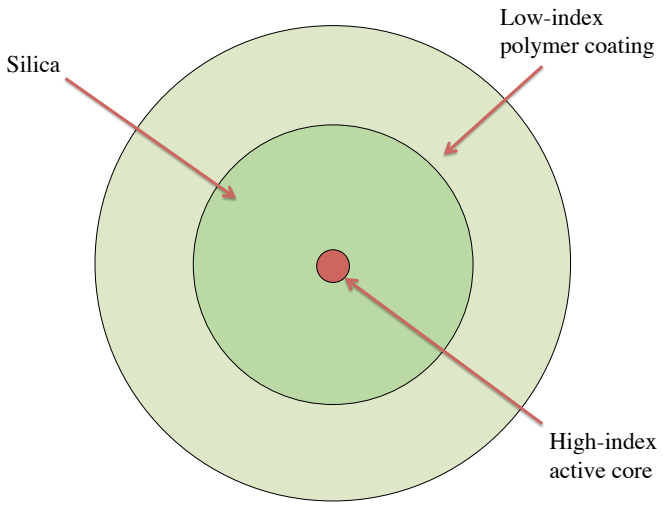

Figure 2.11: Cross section of a active double-clad fiber. The structure is comprised of a high-index active core surrounded by a silica cladding, and a low-index polymer coating.

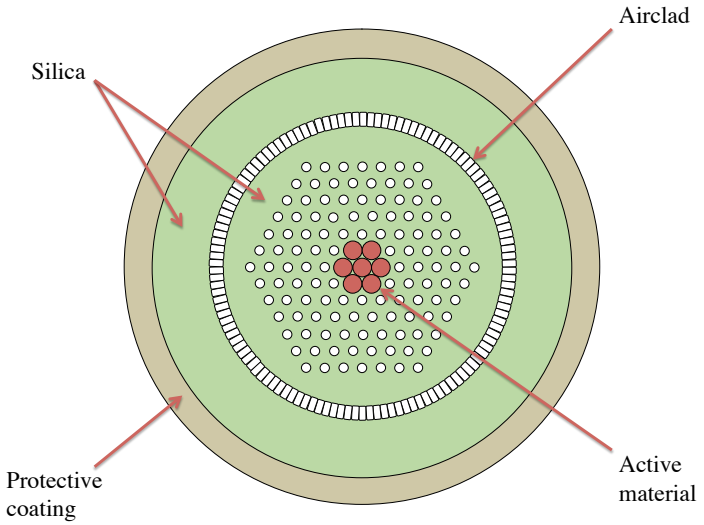

Figure 2.12: Cross section of an active airclad fiber for high power applications. The structure is comprised of the active core surrounded by a single-mode LMA structure, a multimode pump core, and an airclad. The all-glass fiber is protected by a thin layer of polymer coating.

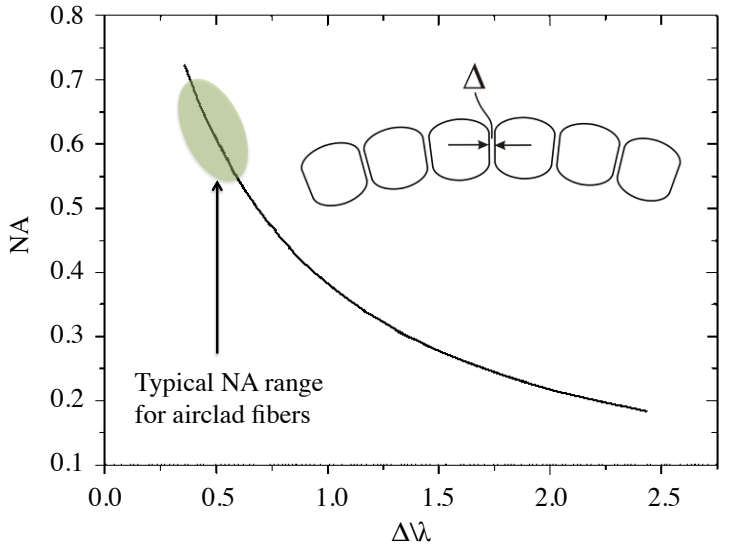

Figure 2.13: The numerical aperture of the airclad is determined by the bridge width, Δ, and is typically chosen to be in the range 0.55-0.65. Higher numerical apertures are possible but at the expense of cleavability and handling of the fibers.

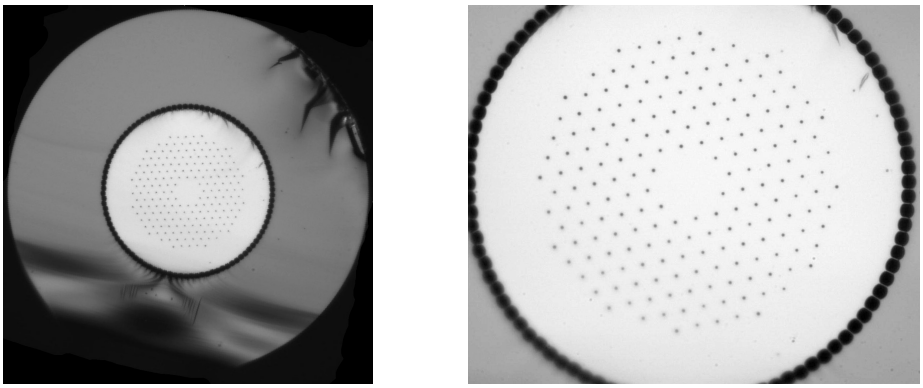

(a) (b)

Figure 2.14: Microscope images of a typical airclad PCF, where (a) is the full fiber cross section and (b)is an enlargement of the pump cladding section.

Chapter 3

High power fiber lasers and amplifiers

Different rare-earth materials are used in active fibers, allowing for amplification in different wavelength regions [39]. While erbium has traditionally been used in telecommunication applications around 1550 nm, ytterbium is now used in most high power lasers and amplifiers at around 1060 nm [40, 41]. Ytterbium has a very broad absorption spectrum spanning from 800 nm to above 1070 nm and the fibers can therefore be pumped by a wide range of lasers. Furthermore, the absorption and emission cross section of ytterbium is very compared to e.g. erbium, allowing for efficient pump absorption and thus short fibers [40]. Recently, development of high power thulium lasers and amplifier around 2 μm has progressed [42]. The bandwidth of thulium is extremely large and ranges from $\sim$1.7 μm to $\sim$2.1 μm. These IR wavelengths are more eye-safe and find a multitude of applications within sensing and surgery. Ytterbium is used as laser active material in all fibers discussed in this thesis.

This chapter will introduce the properties and limitations of ytterbium-doped fibers used in high power fiber lasers and amplifiers. Furthermore, a fiber amplifier model will be presented. The model has been used for the development of a long-wavelength solid core PBG fiber amplifier, which is more complex than a traditional ytterbium based fiber amplifier due the low gain in the long-wavelength region.

3.1 Ytterbium absorption and emission

Amplifiers and lasers operate through the process of stimulated emission, where a pump photon is absorbed, bringing a rare-earth ion from its ground state to an excited state. The absorbed energy is then released as a signal photon through stimulated emission.

The trivalent ion Yb^{3+} is used as the dopant in ytterbium-doped fibers. The only ground state of Yb^{3+} is the $^2F_{7/2}$ state and the only excited state of relevance is the metastable state $^2F_{5/2}$. The ground state is split into four Stark levels, while the excited state is split into three Stark levels. The excited state Stark manifold is separated from the ground state Stark manifold by $\sim$1 μm and this simple structure of the electronic levels inhibits excited state absorption for both the pump and laser wavelengths. The energy level diagram is shown in figure 3.1, where the green arrows refer to pump light transitions and the red arrows refer to laser transitions.

When Yb^{3+} ions are placed in a glass host, the exact energy splitting within the two Stark manifolds depends strongly on both the host material and the co-dopant. The active fibers used in this thesis are generally based on silicate glass with aluminium co-doping in order to dilute the ytterbium and avoid ion clustering. Literature offers a wide range of values for the energy splittings, however they all correspond to a specific fiber composition, and therefore the wavelength assignments to the transitions in figure 3.1 are only approximate [40, 43, 44]. Besides being individual to a specific material composition, the energy values of the Stark levels can be very difficult to measure due to broadening of the optical transitions by phonon-induced transitions within the Stark manifolds. In a glass host material like silica, the spectral broadening blurs information about the Stark level splittings. Instead, information about the effective cross section from absorption and emission measurements is used, so that exact knowledge of the Stark levels and specific transition cross sections is not required. The measured absorption and emission cross section of an ytterbium-doped aluminosilicate fiber is shown in figure 3.2.

Transitions from the lowest lying ground states to the upper levels in the excited state gives rise to the broad absorption spectrum centered around 915 nm. Absorption at longer wavelengths is formed by transitions

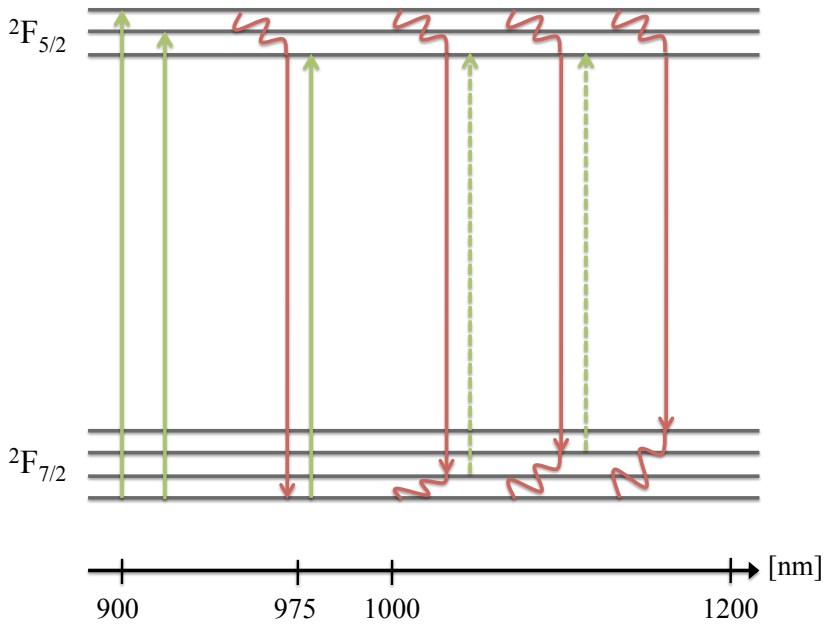

Figure 3.1: Energy level diagram for Yb_{3+} with possible absorption and emission lines.

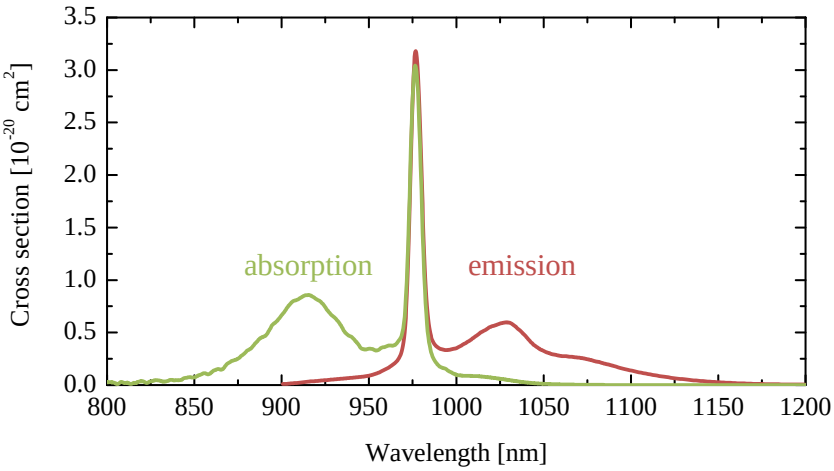

Figure 3.2: Absorption and emission cross section of an ytterbium-doped aluminosilicate fiber.

from the second lowest ground state level. After excitation to the upper levels of the excited states a fast, non-radiative phonon-induced transition to the lower level of the excited state occurs. The strongest transition is between the lowest lying states of the two manifolds at ∼975 nm – this is the zero-phonon line, because there are no phonon rethermalization processes at this transition. From the lowest level of the excited state, transitions to all sublevels of the ground state manifold can occur, giving rise to the broad emission spectrum above 1000 nm. The peaks around 1030 nm and 1080 nm are due to transitions to the second and third lowest ground state levels respectively. After transition to one of the higher sublevels in the ground state a second fast phonon-induced transition back to the lowest lying ground state rethermalizes the system. A prerequisite for obtaining gain in a fiber is that the laser transition is at longer wavelengths than the pump. The pump wavelength generally spans from 800 nm to 1070 nm, while the laser wavelength can extend from 970 nm to 1200 nm.

Since the separation of the sublevels are on the order of k_BT, the effective cross sections are temperature dependent. The lower the temperature, the more populated are the lowest lying sublevels, while higher

temperatures will increase the occupation probability of the higher lying sublevels and allow for increased absorption at longer wavelengths. This temperature dependence is used to enable lasing at long wavelengths above 1100 nm [45].

3.2 Power limitations

Besides stimulated emission, spontaneous emission also occurs and contribute to the noise in the signal. Furthermore, the spontaneous emission can be amplified to high power levels and thereby limit the gain of the amplifier or laser at the desired wavelength. This is especially detrimental in systems that operate at weak transitions, e.g. at very long wavelengths near the edge of the ytterbium emission band. Problems with amplified spontaneous emission (ASE) can be overcome by optimizing the fiber design, by exploiting the temperature dependence of the emission spectrum or by optimizing the laser or amplifier design.

Restriction on the power in fiber lasers and amplifiers are mainly due to nonlinear effects, which scale as the product of power density and fiber length, thus progress in the reduction of nonlinearities entails shorter fibers and larger mode areas in order to reduce the power density. The main nonlinearities to limit the output power of fiber lasers and amplifiers are stimulated Brillouin scattering (SBS) and stimulated Raman scattering (SBS) [46].

Brillouin scattering occurs when incident light in a fiber generates an acoustic wave, which modulates the refractive index of the medium. This index grating scatters light in the backward direction through Bragg diffraction. For high optical powers, the effect becomes stimulated and can reflect most of the power of an incident beam. The stimulated Brillouin scattering (SBS) threshold depends strongly on the spectral width of the incident beam and becomes a serious problem in narrowband amplifiers. SBS is the lowest threshold nonlinearity in fibers, and the threshold power, P_{SBS}, is given by

$$P_{SBS} = \frac{21 A_{eff}}{g_B(\Delta\nu) L_{eff}}, \tag{3.1}$$

where

$$L_{eff} = \frac{1}{\alpha}(1 - e^{-\alpha L}), \tag{3.2}$$

$$A_{eff} = \pi \left(\frac{MFD}{2} \right)^2, \tag{3.3}$$

and

$$g_B(\Delta\nu) = \frac{g_B}{1 + \frac{\Delta\nu}{\Delta\nu_B}}. \tag{3.4}$$

Here MFD is the mode field diameter of the core, L is the length of the amplifier, α is the loss in the fiber, $\Delta\nu$ is the bandwidth of the signal laser, g_B is the Brillouin gain and $\Delta\nu_B$ is the Brillouin gain bandwidth [46]. The Brillouin gain is typically on the order of 5×10^{-11} m/W and the Brillouin gain bandwidth is on the order of 50 MHz [46]. SBS can be mitigated by modulating the phase of the incoming light, by increasing the bandwidth of the light or by inducing variations in the acoustic velocity across the core. Recently SBS suppression has been achieved in a so called acoustically modified PCF where the core is made from segments with different acoustic properties [47].

Stimulated Raman scattering (SRS) is the scattering of a photon by a molecule to a lower-frequency photon as the molecule makes a transition to a different vibrational state. Due to the noncrystalline nature of silica glass the Raman gain in a fiber extends continuously over a broad range of frequencies. The frequency shift is called a Stokes shift and it is possible to observe several Stokes orders if the pump intensity is sufficiently high. SRS is mostly a problem in high power pulsed fiber amplifiers. It can transfer the pulse energy into a wavelength range where amplification does not occur, and this will limit the peak power of the device. It is possible to design fibers which suppress the Raman scattering by filtering the Raman-shifted wavelength component [48, 49]. The threshold for SRS in the forward direction is approximately given by

$$P_{SRS} = \frac{16 A_{eff}}{g_R L_{eff}}, \tag{3.5}$$

where the Raman gain g_R is on the order of 10^{-13} m/W for silica at $\sim$1 μm [39]. Since SBS is the lowest threshold nonlinearity, SRS is typically not the limiting factor in high power fiber lasers and amplifiers.

In addition, self focusing is thought to impose the ultimate limit to the obtainable output power from a fiber laser or amplifier. High intensity in the center of a beam will cause an increase in the refractive index in the

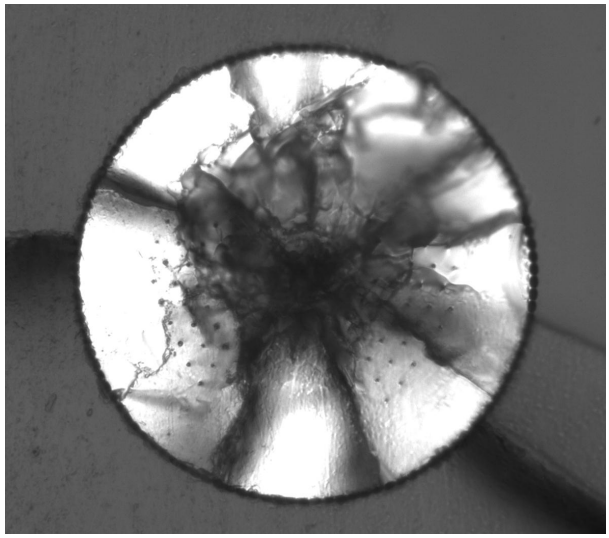

Figure 3.3: Microscope image of a fiber which has been damaged by a high intensity pulse.

center of the core through a Kerr process. The modified refractive profile will act as a focusing lens and trigger a run-away process eventually leading to optical damage. The power threshold is independent of core size and has been calculated to be 4.3 MW at a wavelength of 1 μm [50]. This power level, however, has already been reached without damage in a rod-type PCF [10]. Figure 3.3 shows a microscope image of a fiber which have been damaged by a high intensity pulse.

3.3 Fiber amplifier model

The dynamics of an amplifier is governed by the rates of change of the population densities as a result of pumping and seeding. Considering a two atomic levels, assuming that ASE does not extract significant power and assuming a homogeneous system, the rate equations for the population densities are simple [39]. The rate equation for the ion density in the upper

level is given by

$$\begin{aligned}\frac{\delta N_2}{\delta t} = &\left(\frac{\Gamma_p \sigma_{ap} P_p(z) \lambda_p}{hcA_{core}} + \frac{\Gamma_s \sigma_{as} P_s(z) \lambda_s}{hcA_{core}}\right) N_1 \\ &- \left(\frac{\Gamma_p \sigma_{ep} P_p(z) \lambda_p}{hcA_{core}} + \frac{\Gamma_s \sigma_{es} P_s(z) \lambda_s}{hcA_{core}}\right) N_2 \\ &- \frac{N_2}{\tau},\end{aligned} \tag{3.6}$$

where the first section of the equation corresponds to the rate of absorption from the lower level, the second section to the rate of stimulated emission from the upper level, and the third section to the rate of spontaneous emission from the upper level. $P_p(z)$ and $P_s(z)$ are the power levels of the pump and signal light; A_{core}, h, and c denote the area of the core, Planck's constant and the speed of light; σ_{ap} and σ_{as} the absorption cross section at the pump and signal wavelength; and σ_{ep} and σ_{es} the emission cross section at the pump and signal wavelength. Γ_s is the signal overlap factor, accounting for the amount of signal power that propagates through the doped region, Γ_p the equivalent pump overlap factor, and τ is the upper state life time, which is on the order of a millisecond.

The signal overlap factor, Γ_s, is given by

$$\Gamma_s = 2\pi \int_0^R i(r) r dr = 1 - e^{-R^2/\omega^2}, \tag{3.7}$$

where $i(r)$ is the normalized transverse mode intensity profile, R the radius of the core and ω is the mode radius of the field. In a highly multimode pump cladding, the pump intensity is assumed to be constant within the pump cladding and the pump overlap factor, Γ_p, is given by

$$\Gamma_p = \frac{A_{core}}{A_{cladding}}, \tag{3.8}$$

where $A_{cladding}$ is the cladding area. Similarly, the rate equation for the ion density in the lower level is given by

$$\frac{dN_1}{dt} = -\frac{dN_2}{dt}. \tag{3.9}$$

Within an infinitesimal length of the amplifier, the pump and the signal power levels will be attenuated or amplified by absorption from ions in level

1 and stimulated emission from ions in level 2. The power propagation equations are given by

$$\frac{dP_p(z)^{\pm}}{dz} = \pm\left[\Gamma_p(\sigma_{ep}N_2 - \sigma_{ap}N_1) - \alpha_p\right]P_p(z)^{\pm}, \tag{3.10}$$

$$\frac{dP_s(z)}{dz} = \left[\Gamma_s(\sigma_{es}N_2 - \sigma_{as}N_1) - \alpha_s\right]P_s(z), \tag{3.11}$$

where $P_p(z)^+$ corresponds to co-propagating signal and pump light, while $p_p(z)^-$ corresponds to counter-propagating signal and pump light, and α_p and α_s are the loss rates at the pump and signal wavelength, respectively.

Equations 3.10 and 3.11 can be simplified by introducing the total ion density, N, which is a known parameter,

$$N = N_1 + N_2, \tag{3.12}$$

and solving equation 3.6 for N_2 under steady state conditions. Doing this one obtains the equations

$$N_2(z) = \frac{\left[\frac{\Gamma_p\sigma_{ap}P_p(z)^{\pm}\lambda_p + \Gamma_s\sigma_{as}P_s(z)\lambda_s}{hcA_{core}}\right]}{\left[\frac{\Gamma_p(\sigma_{ap}+\sigma_{ep})P_p(z)^{\pm}\lambda_p + \Gamma_s(\sigma_{as}+\sigma_{es})P_s(z)\lambda_s}{hcA_{core}}\right] + \frac{1}{\tau}}N, \tag{3.13}$$

$$\pm\frac{dP_p(z)^{\pm}}{dz} = \Gamma_p\big[\left[(\sigma_{ap}+\sigma_{ep})\,N_2 - \sigma_{ap}N\right] - \alpha_p\big]P_p(z)^{\pm}, \tag{3.14}$$

$$\frac{dP_s(z)}{dz} = \Gamma_s\big[\left[(\sigma_{as}+\sigma_{es})\,N_2 - \sigma_{as}N\right] - \alpha_s\big]P_s(z). \tag{3.15}$$

In the case of co-propagating signal and pump the equations are solved numerically by propagating the power from the input to the output end. The case of counter-propagating signal and pump is slightly more involved – the equations are solved numerically by propagating the input pump power and an estimate for the output signal power from the pump input end to the other end, while refining the output signal power estimate in iterations [51].

The total gain G achieved in a length of fiber is given by

$$G = e^{\int_0^L g(z)dz}, \tag{3.16}$$

where

$$g(z) = N_2\sigma_{es} - N_1\sigma_{as}. \tag{3.17}$$

Equation 3.16 can be solved using equations 3.12 and 3.14. In [43] the gain is calculated to

$$G = 4.34 \cdot \left[\frac{(\sigma_{es} + \sigma_{as})\tau(P_p(0) - P_p(L))\lambda_p}{hcA_{core}} - N\sigma_{as}L \right] dB. \tag{3.18}$$

ASE can be included in the model by adding a term to equation 3.15. The ASE power is given by

$$P_{ASE} = 2h\nu\Delta\nu, \tag{3.19}$$

where $\Delta\nu$ is a specific frequency bandwidth. The growth of ASE must be calculated for several frequency bandwidths $\Delta\nu$ separately and the effect of the ASE back on the population inversion has to be taken into account in an iterative manner, considering all boundary conditions for the pump, signal and ASE power in both ends of the fiber. The propagation equation 3.15 becomes

$$\begin{aligned} \pm\frac{dP_k(z)^{\pm}}{dz} &= \Gamma_s\big[[(\sigma_{ak} + \sigma_{ek})\, N_2 - \sigma_{ak}N] - \alpha_k\big]P_k(z)^{\pm} \\ &\quad + P_{ASE,k}N_2\sigma_{ek}, \end{aligned} \tag{3.20}$$

where k corresponds to the k^{th} frequency bandwidth for which the ASE is calculated. The $\pm$-sign in equation 3.20 accounts for the fact that ASE occurs in both the forward and backward direction. Although ASE does pose a limitation to high power systems, ASE usually does not have a significant effect below gain levels of 30 dB [40], and therefore has not been included for calculations in this thesis.

The fiber amplifier model is used for analyzing the parameters and results of the high power solid core photonic bandgap fiber amplifier for 1178 nm amplification, described in chapter 6.

Chapter 4

Photo darkening

Power scaling of ytterbium-doped fiber lasers and amplifiers introduces several challenges with nonlinear effects. Most of the nonlinear effects limiting the achievable output power are intensity related and can be overcome e.g. by reducing the fiber length and increasing the core size and the core material absorption. Increasing the material absorption is done by increasing the doping concentration, however, from a power scaling point of view increasing the doping concentration is not always ideal as too high a doping concentration may lead to ion clustering, which can seriously degrade the gain and efficiency of a laser or amplifier. Aluminium and phosphor are typically used to dilute ytterbium in order to avoid clustering.

Highly doped ytterbium fibers are known to suffer from induced optical losses, known as photo darkening. In general, photo darkening in ytterbium-doped silica fibers is associated with a high population density of the ytterbium ions in the upper Stark manifold, which is known to be related to the emission of green light, typically observed in pumped ytterbium-doped fibers as shown in figure 4.1 [52].

Photo darkening is found to increase and subsequently to saturate following prolonged exposure to pump radiation [53]. Obvious approaches to keeping the population density down are reducing the ytterbium concentration in the fiber or operating systems in a safe regime with respect to photo darkening. Reducing the doping concentration will adversely affect many applications that require short fiber lengths and will limit the power scaling options. Therefore it is important to understand the

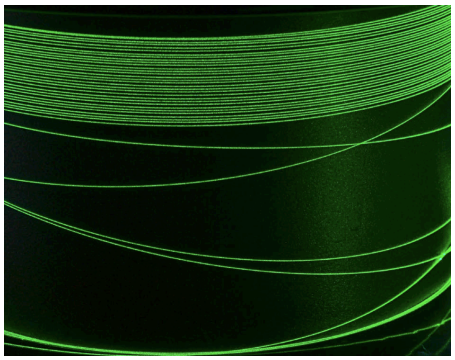

Figure 4.1: Emission of green light from a pumped ytterbium-doped fiber. The green light emission is related to ion clusters in the ytterbium material.

photo darkening mechanisms and to develop means for mitigating photo darkening without sacrificing the overall performance of the fiber laser or amplifier. This can involve developing special fiber designs and new material compositions.

This chapter will present an introduction to the basic mechanisms of photo darkening. Several different approaches to the understanding of photo darkening have been proposed [54], however, the present description is based on a model developed at NKT Photonics [53, 55]. Results from an investigation of fibers with different material compositions will be presented – mainly a comparison between co-doping with aluminium and phosphor. The purpose of the investigation has been to support the development of the photo darkening model and to benchmark different material compositions.

4.1 Color center formation

Photo darkening in ytterbium-doped fibers is associated with color centers created during the amplification process [53]. A color center is a defect in the glass which produces optical absorption bands in the otherwise transparent material over time. The absorption bands are extremely wide and absorbs both pump and signal light, thus reducing the power conversion efficiency of the fiber and generating excess heat. The reduced power efficiency leads to a reduced reliability and lifetime of the fiber, an issue of concern for most industrial fiber laser manufacturers [56].

Si^{4+} ions in general are organized in silica tetrahedrons with one ion of Si and four ions of O as shown in figure 4.2(a). Both Yb^{3+} and Al^{3+} ions are organized in octahedrons networks as shown in figure 4.2(b). When the glass material is dominated by SiO_2, the ytterbium oxide and aluminium oxide is forced into the tetrahedron structure of silica and as a consequence part of the oxygen can become non-binding, resulting in a number of lone electrons on the oxygen atoms. Examples of non-binding oxygen (NBO) sites are illustrated in figures 4.2(c) and 4.2(d), where the singlet NBO complex has a single bridging oxygen atom and the triplet NBO complex has three bridging oxygen atoms. The NBO sites are found at the interface between the octahedron and tetrahedron network.

When a non-binding oxygen is subjected to pump radiation, there is a probability that the atom will absorb a pump photon and excite an electron in the triplet spin state. When ytterbium is subjected to pump radiation, the excess energy is radiated as phonons. These phonons can transfer the excited triplet electron into a vibrational singlet state. In the singlet state, the electron can get excited by an additional pump photon and get transferred to a nearest neighbour non-binding oxygen atom. This creates a negatively charged NBO site (a hole) and a positively charged NBO site (a trap) and results in a Coulomb field between the two neighbouring oxygen atoms. Color centers are associated with these trap/hole pairs and the large number of energy states in the Coulomb field is responsible for the large absorption cross section of the color centers. Thus two pump photons in combination with a phonon is needed to create a color center. Additional phonons can either bleach the color center or shift the lone electron further away from the hole, and thereby increase the stability of the color center.

The possibility of finding NBO sites increase with the size of ion clusters in the material and the distribution of NBO sites depends strongly on the exact composition of the material. Different co-doping materials are used to dilute the ytterbium and reduce the size of ion clusters in the material. The most common co-dopings are aluminium and phosphor. Increasing the aluminium concentration relative to the ytterbium concentration will reduce the photo darkening [57], however too high a concentration will cause the glass to crystallize.

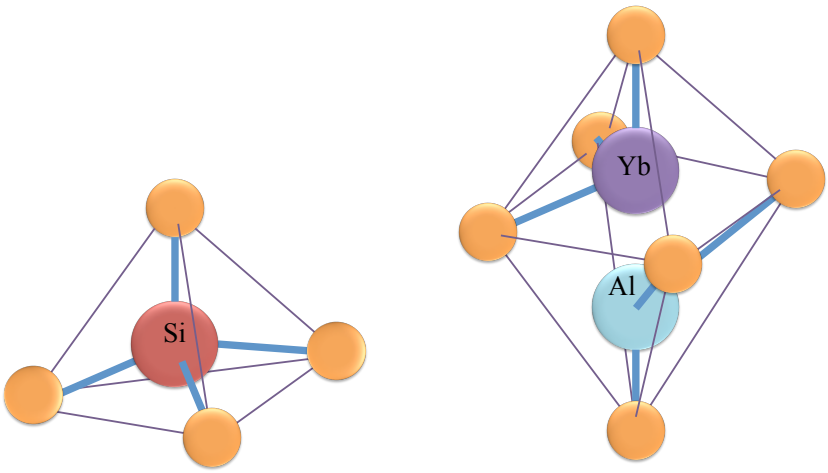

(a) Silica tetrahedron

(b) Yb:Al octahedron network

(c) Singlet NBO complex

(d) Triplet NBO complex

Figure 4.2: Illustration of the ion networks. The silica network accommodates clusters through non-binding oxygen (NBO) complexes. Electron exchange among NBO sites creates color centers.

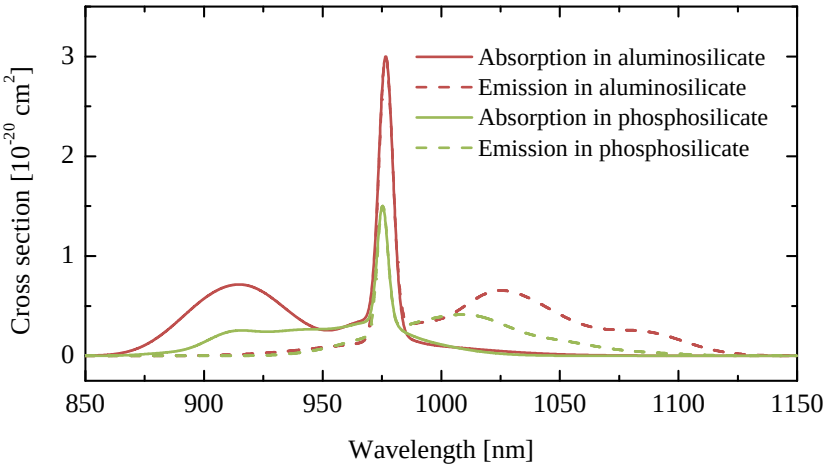

Figure 4.3: Emission and absorption cross sections for ytterbium in aluminosilicate and phosphosilicate fibers.

P^{5+} ions, on the other hand, are organized in tetrahedrons rather than octahedrons. Phosphor therefore accommodates part of the ytterbium directly in the tetrahedral silica network and thereby lowers the number of NBO sites. Furthermore, due to its chemical similarity to hydrogen, phosphor binds the oxygen, thus reducing the number of NBO sites even further. Generally, phosphor co-doped fibers show limited or no photo darkening over time [58]. One possible drawback of the phosphor co-doping is that the absorption is significantly reduced compared to aluminium co-doped fibers as shown in figure 4.3. To compensate for this a higher ytterbium concentration is needed, which in turn leads to a higher refractive index contribution. This can be diluted by fluorine, but complicates the fabrication process. The long stability is also a concern due to the increasing water absorption.

4.2 Accelerated photo darkening test setup

Measurements of the induced loss due to photo darkening be realized either by measuring the properties of a full fiber laser or amplifier system over an

extended period of time or by measuring the properties of a short sample of the fiber of interest. For benchmarking purposes a fast and repeatable method is preferred. The time of a measurement can be decreased by maximizing the population inversion to rapidly induce photo darkening, while repeatability requires control and tunability of the inversion, which is easier in a short sample.

Different measurement techniques have been proposed for benchmarking ytterbium-doped fibers. One requires core pumping of the sample and has the advantage that the inversion can be saturated and thereby independent of pump power [57, 59]. This approach, however, is limited to small core sizes. As the core size is increased, the inversion becomes harder to saturate and the subsequent pump power dependence of the inversion could induce an intensity dependent photo darkening profile across the core. A second approach involves cladding-pumping of the fiber [60, 61]. The inversion is now dependent on pump power, however, due to the much larger multimode pump cladding, the intensity distribution is flat over the whole core area, thus reducing intensity related effects. Furthermore, keeping the population inversion below the saturation level allows for measurements at several different inversion levels by varying the pump power. In addition, parasitic lasing must be avoided, as this will otherwise reduce the population inversion.

The present investigation covers CW operation of an unseeded amplifier and the population inversion N_2/N can be determined from equation 3.13. The inversion is given by

$$\frac{N_2(z)}{N} = \frac{\left[\frac{\sigma_{ap} P_p(z) \lambda_p}{hcA_{cladding}}\right]}{\left[\frac{\sigma_{ap} P_p(z) \lambda_p}{hcA_{cladding}} + \frac{1}{\tau}\right]}. \tag{4.1}$$

where $\tau \approx 0.83\ ms$ in aluminosilicate fibers and $\tau \approx 1.45\ ms$ is phosphosilicate fiber [62] while $\sigma_{ap} \approx 0.7 \cdot 10^{-20}\ cm^2$ in aluminosilicate fibers and $\sigma_{ap} \approx 0.25 \cdot 10^{-20}\ cm^2$ in phosphosilicate fibers at the pump wavelength 915 nm as shown in figure 4.3.

A typical test fiber is designed with a step index core, which is single-mode at the lasing wavelengths of ytterbium around 1000-1100 nm. A solid multimode pump cladding is surrounded by an airclad, providing the pump

cladding with an NA above 0.58 and enabling cladding-pumping in the setup. The cross section of a typical step-index airclad test fiber is shown in figure 4.4. The pump cladding is typically 150 μm in diameter, while the core ranges from 9 to 20 μm.

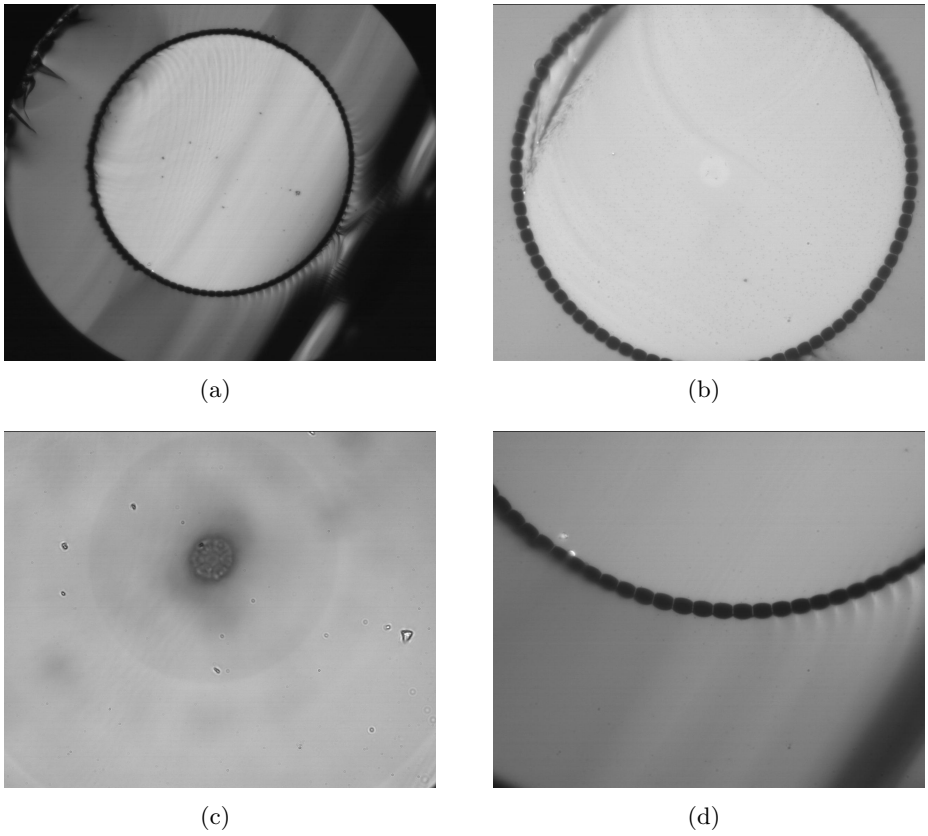

(a) (b)

(c) (d)

Figure 4.4: Microscope images of a typical photo darkening test fiber. (a) The total fiber cross section. (b) The pump cladding with a diameter of 150 μm, surrounded by an airclad. (c) The step-index core with a diameter ranging from 8 μm to 19 μm. (d) The airclad providing an NA above 0.58.

The experimental setup for characterizing the fiber samples is shown in figure 4.5. The purpose of the setup is to provide information about the spectral shape of the induced color centers in the visible and near infrared wavelength region and their temporal evolution. Pump power is provided

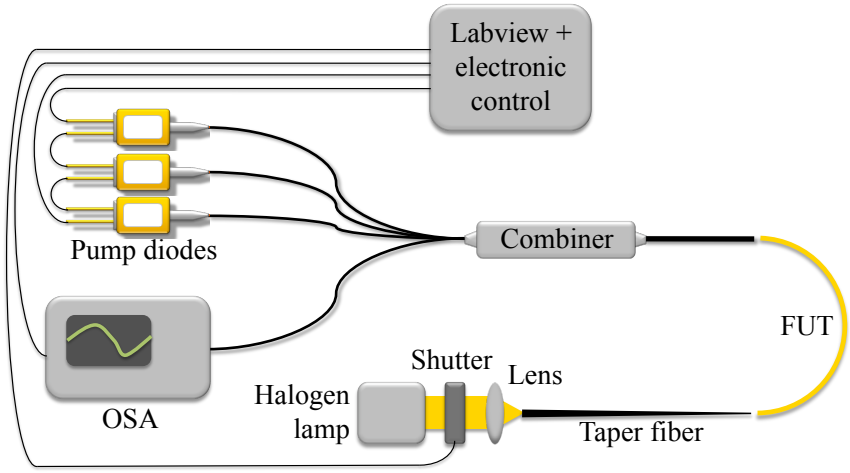

Figure 4.5: Schematic drawing of the experimental setup for measuring accelerated photo darkening.

by three 915 nm multimode laser diodes with 105/125 μm, 0.22 NA pigtails spliced onto a standard 7:1 multimode power combiner with a 125 μm, 0.45 NA output port. The output port is butt-coupled to the ytterbium-doped fiber under test (FUT), which is typically 40–50 cm long. The test fiber is cladding pumped and the pump power is limited to 10 W in the setup. In order to prevent lasing at high population inversion levels, the test fibers are cleaved at an angle of $\sim 5^\circ$ in both ends and the pump power is kept below the lasing level at all times as lasing will otherwise reduce the population inversion.

Probe light is provided by a 100 W halogen lamp. The collimated light from the halogen lamp is coupled by a microscope objective into the large core, low NA end of a 4 m long taper fiber. The taper fiber has a core of 400 μm in the low NA end and is tapered down to 150 μm with an NA of up 0.65 in the opposite end. The purpose of the taper fiber is to optimize coupling of probe light into the test fiber. The small core, high NA end of the taper fiber is butt-coupled to the test fiber. The probe light is collected from one of the unused input port of the power combiner, which is connected to an optical spectrum analyzer (OSA), capable of measuring in the wavelength region from 350 nm to 1750 nm.

The measurement is started with the pump diodes turned off. A broadband reference scan is performed on the OSA with only the probe light present, and subsequently the probe light is blocked by a shutter and the pumps are turned on for a specific period of time. Afterwards, the pump diodes are turned off, the shutter is opened and a new broadband OSA scan is performed. The sequence is repeated seven times during the first hour of the measurement, due to the initial fast increase in photo darkening, and hereafter every 30-60 minutes for a total duration of at least 48 hours. With respect to the transmitted probe light, the stability of the setup is typically better than 0.2-0.3 dB over 48 hours.

4.3 Experimental investigation

It has been shown that there is a linear correlation between the induced loss at visible wavelengths and the induced loss at typical signal wavelengths of 1040-1070 nm [53, 59]. Furthermore, the color centers have an absorption peak in the visible wavelength region which is roughly 70 times larger than in the signal wavelength region. Therefore one can rely on transmission changes at visible wavelengths as an indicative measure of photo darkening at the signal wavelengths, which is an obvious advantage when measuring fibers with low photo darkening rates. The growth of the absorption peak in the visible wavelength region is evident in figure 4.6. The graph shows the induced loss as function of wavelength at different times during a measurement of an aluminium co-doped fiber.

The initial photo darkening rate is seen to follow a power low with a seventh order dependence on the population inversion [61]. However, in spite of the very high order dependence on population inversion, the photo darkening is found to saturate following prolonged exposure to radiation and it is found that the actual saturation level depends on the population inversion [14, 53, 60]. Figure 4.7 shows the induced loss at 605 nm as a function of time for an aluminium co-doped fiber at three different inversion levels. The wavelength 605 nm is chosen for practical reasons. The loss rate is initially fast during the first 5-10 hours, but subsequently slows down. The population inversion levels in these measurements are not high enough to support the assumption of a saturated induced loss, however, the asymptotic behavior indicates a population inversion dependence.

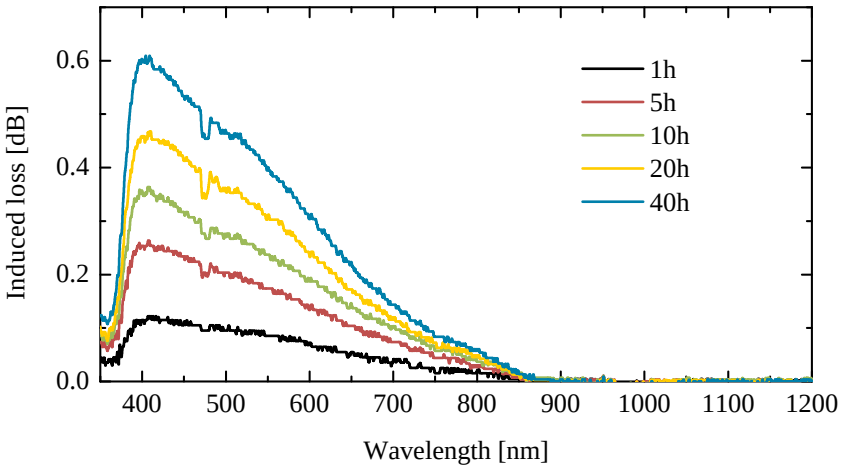

Figure 4.6: Induced loss as a function of wavelength at different times during a measurement of an aluminium co-doped fiber with a Yb:Al ratio of 0.35:1.5.

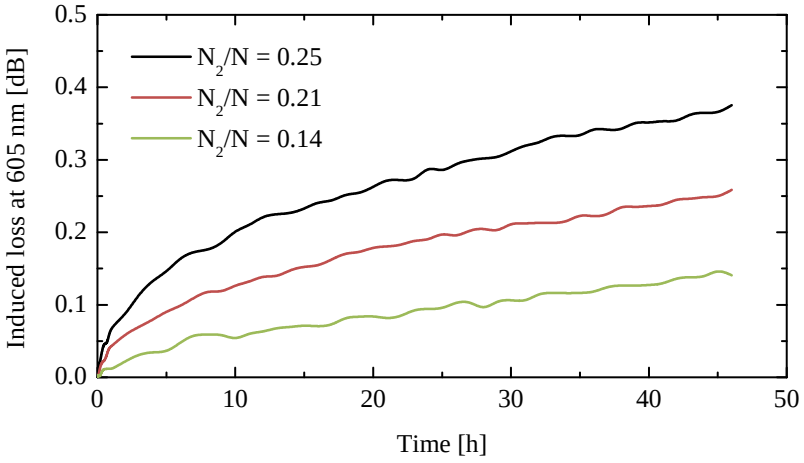

Figure 4.7: Induced loss as a function of time at different inversion levels for an aluminium co-doped fiber with a Yb:Al ratio of 0.35:3.4.

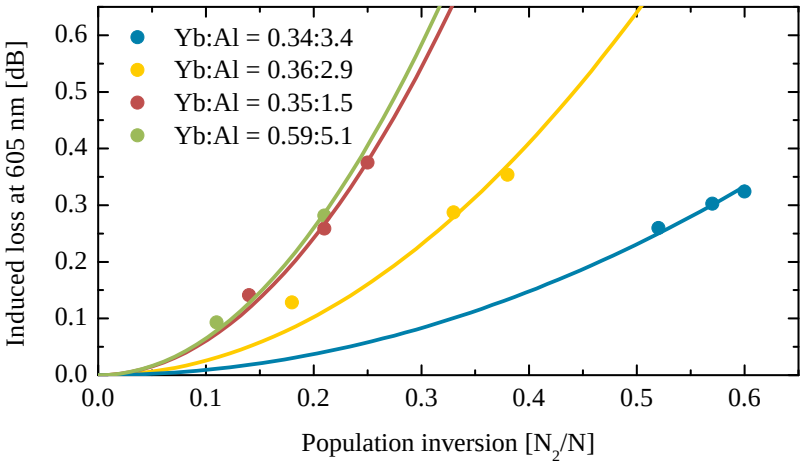

Figure 4.8: Induced loss at 605 *nm* for three aluminium co-doped fibers as a function of population inversion. Second-order power functions are fitted to the measured data.

In [57] it has been suggested that the photo darkening of ytterbium-doped fibers has a second-order power dependence on the population inversion. Figure 4.8 shows the induced loss at 605 *nm* after the test as a function of population inversion for four different aluminium co-doped fibers. The solid curves in the graph are second-order power functions fitted to the measurement data, consistent with the second-order power correlation. Three of the fibers – the red, yellow, and blue curves – have nearly the same ytterbium concentration, but increasing aluminium concentration. It is apparent from the graph that with a constant ytterbium concentration an increase in aluminium concentration will reduce the photo darkening as suggested in [57]. The last fiber shown in green has higher concentrations of both ytterbium and aluminium compared to the other fibers, however, the relative concentration of aluminium to ytterbium is twice as high for this fiber (0.59:5.1) as for the red curve (0.35:1.5), suggesting that an increase in ytterbium concentration requires an even larger increase in aluminium concentration. In figure 4.9 the induced loss at 605 *nm* after the test for the three fibers with the same ytterbium concentration is plotted as function of aluminium concentration at a population inversion level of 0.5. The graph

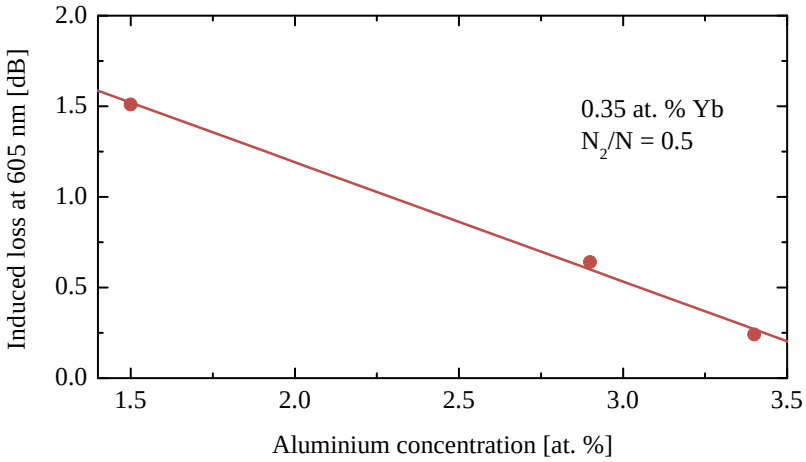

Figure 4.9: Induced loss at 605 *nm* as a function of aluminium concentration for three aluminium co-doped fibers with the same ytterbium concentration at a population inversion level of 0.5.

suggests a linear correlation between the aluminium concentration and the induced loss.

A comparison between fibers with nearly the same ytterbium concentration but co-doped with either aluminium or phosphor confirms that the induced loss mechanisms are quite different in the two cases. Figure 4.10(a) shows the induced loss after the 48 hour test as a function of wavelength for the aluminium co-doped fiber with a Yb:Al ratio of 0.34:3.4 (red curve) and the phosphor co-doped fiber with a Yb:P ratio of 0.39:3.27. Both fibers have been kept at a population inversion level of ∼0.4 during the measurement. The phosphor co-doped fiber is shown alone in figure 4.10(b) where negative values of the induced loss exists for some wavelengths in the visible region. The negative loss value is consistent with measurements on other phosphor co-doped fibers – this could indicate that color centers already exist in the material prior to the measurement and are bleached by the pump photons. The model in [53] discusses the possibility of pre-existing color centers in phosphor co-doped material.

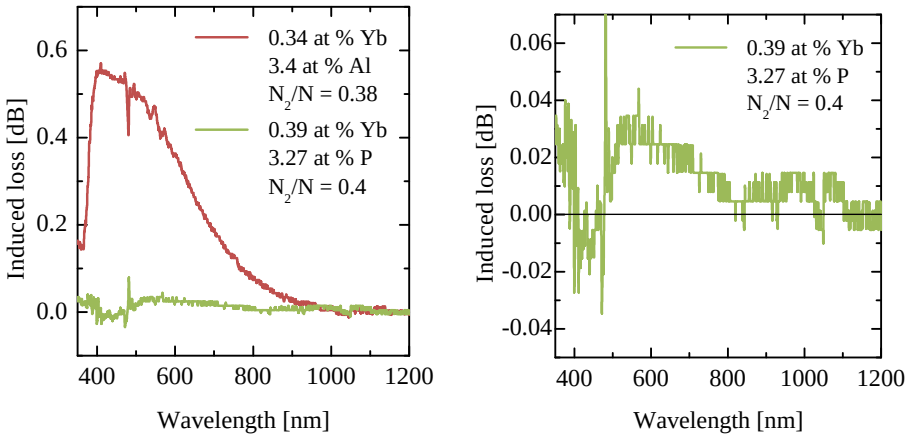

(a) (b)

Figure 4.10: Induced loss after the 48 hours test as a function of wavelength (a) for an aluminium co-doped fiber and a phosphor co-doped fiber and (b) for the phosphor co-doped fiber alone.

In figure 4.11 the induced loss at 605 *nm* after the test is shown as a function of ytterbium concentration for three phosphor co-doped fibers with the same phosphor concentration at a population inversion level of ∼0.4. The results confirm that an increase in ytterbium concentration increases the induced loss, however a loss level below 0.1 *dB* for high ytterbium concentrations is still more than an order of magnitude lower compared to fiber with aluminium co-doping.

In spite of the overall picture indicating that phosphor co-doping will decrease the photo darkening rate significantly, it has been suggested that the slope efficiency of these fibers is reduced by 10% compared to aluminium co-doped fibers after saturation of the photo darkening has been reached [53, 63]. Measurements on the phosphor co-doped fibers resulted in slope efficiencies below 50%, while the pure aluminium co-doped fibers had efficiencies of around 70%. The addition of aluminium to a phosphor co-doped fiber should improve the slope efficiency while still retaining a low photo darkening rate [64].

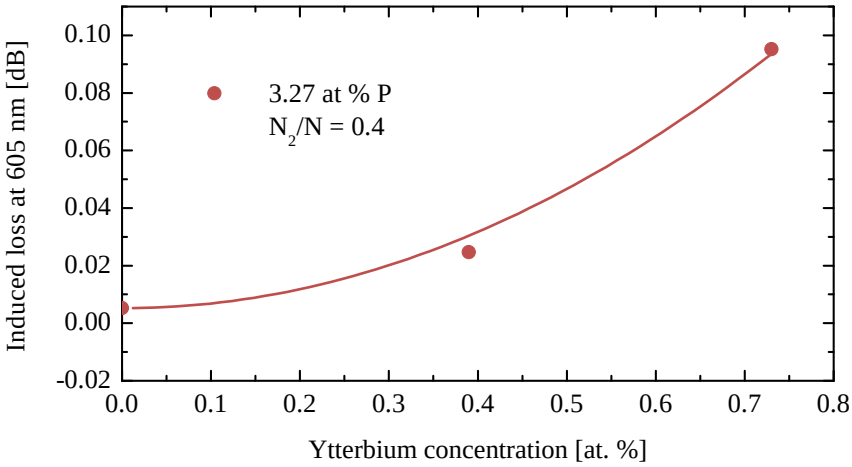

Figure 4.11: Induced loss at 605 *nm* after the test as a function of ytterbium concentration for the three fibers with the same phosphor concentration.

Figure 4.12 summarizes the investigation by showing the induced loss at 605 *nm* after the test as a function of population inversion for all fibers in the investigation including some fibers with unknown concentration ratios. Each color represents one type of material composition and for each composition there are multiple fibers with different composition ratios. The exact composition ratios are not specified in the plot. The red dots are fibers with aluminium co-doping, the green dot are fibers with phosphor co-doping and the black dots are fibers with aluminium/phosphor co-doping. The phosphor and aluminium/phosphor fibers show almost no induced loss even at very high inversion levels, while the pure aluminium co-doped fibers show a consistently higher induced loss at all inversion levels. Due to the lower absorption cross section of the pure phosphor co-doped fiber, these fibers have not been tested at very high inversions levels.

In addition to phosphor co-doping recent investigations have suggest cerium as a possible candidate for mitigating photo darkening in ytterbium-doped fibers [65]. An initial test of a cerium co-doped solid core PBG fiber has been performed in a seeded amplifier configuration. The test showed great improvements of the photo darkening characteristics and the results are discussed in more detail in chapter 6.

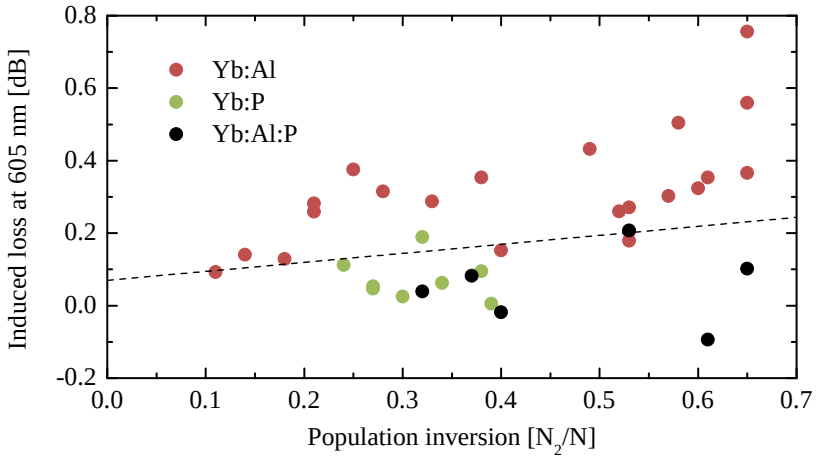

Figure 4.12: Induced loss at 605 *nm* after the test as a function of population inversion. The red dots are fibers with aluminium co-doping, the green dot are fibers with phosphor co-doping and the black dots are fibers with aluminium/phosphor co-doping.

Summary

The aim of the photo darkening investigation was to develop a procedure for benchmarking different material compositions and to support the development of a model describing the photo darkening process. Fibers with aluminium and phosphor co-doping and varying doping concentrations have been tested in the investigation and have supported the general presumptions from the model and literature. The main conclusions are that photo darkening has a second-order power dependence on population inversion, that photo darkening increases with ytterbium concentration and decreases with aluminium concentration, that co-doping with phosphor improves the photo darkening by more than order of magnitude compared to aluminium, but at the expense of a high slope efficiency. A decrease in slope efficiency of 20% has been observed, however, the right combination of aluminium and phosphor co-doping should feature the benefits of phosphor without compromising the slope efficiency. The measurements have contributed to the model, which is now used to compound new material compositions that are subsequently benchmarked experimentally in the accelerated setup.

Chapter 5

Large core fibers

Besides mitigation of photo darkening, the road towards higher powers in shorter fibers with a high nonlinear threshold is through more efficient pump absorption and larger cores. The microstructuring process enables both better pump absorption and larger cores compared to step-index fibers, which makes PCFs very well suited for high power applications. This chapter investigates these features of large core fibers.

It has been suggested that the microstructure in photonic crystal fibers improves the pump absorption compared to standard fibers [66], which in turn enables the use of shorter fibers and increases the nonlinear threshold. The first part of this chapter is an investigation of the effect of the microstructure on the pump absorption as this plays an important role in high power lasers and amplifiers with respect to efficiency, packaging and thermal handling.

The pursuit for higher powers also requires larger core sizes. Furthermore, many applications require a stable, diffraction-limited output, which is increasingly challenging to obtain as the core size is increased. The next section of this chapter describes the development of methods for characterizing and improving large core fibers with focus on beam quality, stability, and bending properties. Obtaining stable, fundamental mode operation in one of the largest flexible fibers on the market is the aim of the investigation.

In addition, the chapter contains a short section introducing the rod-type fiber design, which can be fabricated with a 100 μm core size and with

lengths as short as 50 *cm* for a significant increase in nonlinear threshold. Finally, the chapter contains a short section introducing the S^2 method for characterizing the higher-order mode content in fibers.

5.1 Pump absorption

Cladding-pumped fibers with high NA are commonly used in high power lasers and amplifiers that require capture of pump light from low-brightness laser diodes. The optical efficiency of these lasers depends on the coupling of pump light from the pump cladding to the active core. A very high NA is desirable as is it enables the use of a smaller pump cladding, thus improving the pump absorption by increasing the overlap between the pump light and the doped core. Due to the large index contrast between air and silica, airclad fibers provide the highest possible NA and therefore the highest pump absorption values and the shortest fiber lengths [37]. However, investigations show that pump light launched off-center with a small angle into cladding-pumped fibers are less efficiently absorbed [66, 67]. These so-called skew rays follow a helical off-center path, have no overlap with the doped core and are therefore not absorbed by the active ions in the core. Figures 5.1(a), 5.1(b) and 5.1(c) illustrate how pump light entering off-center with a small angle (red beam path) may not get absorbed while pump light entering with a large angle (blue beam path) is more likely to get absorbed by the core.

Experiments show that skew rays can be suppressed by breaking the cylindrical symmetry of the inner cladding either by changing the shape of the pump cladding [68, 69] or by using the technique of periodic bending of the fiber [41, 70], for example in a 'figure 8' coil. Furthermore, it has been suggested that the pump absorption efficiency can be increased by including a small circular scatterer, which changes the ray pattern and induces chaotic dynamics in the fiber [66]. Suppression of skew rays is an important issue in the optimization of high power fiber lasers and amplifiers – inefficient absorption of the pump power inevitably leads to a poor slope efficiency and for high power lasers in the kilowatt range thermal handling of unabsorbed pump light becomes a serious challenge.

Photonic crystal fibers inherently contain several small circular scatterers due to the hole structure in the pump cladding and are therefore

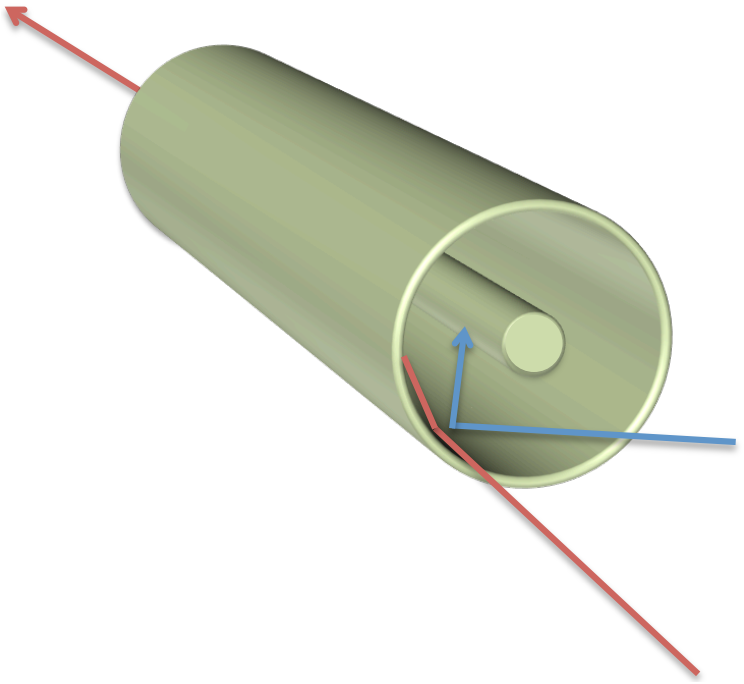

(a)

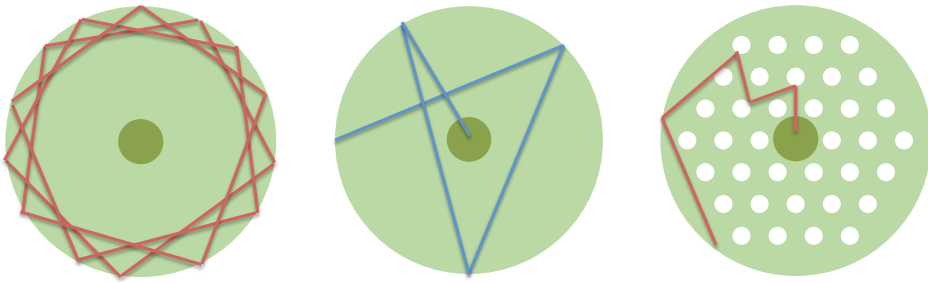

(b) (c) (d)

Figure 5.1: Illustration of off-center small (red) and large (blue) angle beam paths in a cladding-pumped fiber. In (b) pump light entering off-center with a small angle (red beam path) may no get absorbed while in (c) pump light entering with a large angle (blue beam path) is more efficiently absorbed. In (d) the airholes of the cladding structure induces chaotic dynamics in the fiber, thus improving the pump absorption.

expected to be less sensitive to skew rays than a traditional step-index fiber. This is illustrated in figure 5.1(d). The aim of the investigation is to identify the NA of the less efficiently absorbed pump light, secondly to investigate the skew ray scrambling effect of the hole structure in photonic crystal fibers compared to the commonly used periodic bending method for step-index fibers, and finally to compare the pump absorption of airclad and polymer-clad fibers.

Pump absorption measurement procedure

In all experiments of the investigation standard pump absorption measurements have been performed [71]. Determining the amount of skew rays by comparing absolute values of the pump absorption would require that all test fibers have completely identical absorption coefficients and geometrical dimensions. Instead the amount of skew rays can be determined by evaluating the improvement in pump absorption when the fiber is periodically bend in a 'figure 8' coil compared to a circular coil. If the ratio between the pump absorption in a 'figure 8' coil and the pump absorption in a circular coil is close to unity, the periodic bending has no effect. This means that the fiber design does not suffer from skew rays because all the pump light is efficiently absorbed in a circular coil. The higher the ratio the more the fiber design suffers from skew rays.

The pump absorption is measured using the setup in figure 5.2. White light from a halogen lamp is coupled into a multimode taper fiber with a 400 μm core and an NA of 0.21 at the input end, and a 130 μm core and an NA of 0.64 at the output end. The coupling of light into the taper fiber is either done straight or at an angle as shown by the dashed drawing in figure 5.2. By coupling light into a taper fiber at an angle one can produce an output beam with a flat near field pattern and a ring structure in the far field pattern corresponding to only a specific divergence angle as shown in the top left inserts of figure 5.2. Straight coupling into the taper fiber produces the traditional flat far field pattern shown in the top right insert. The reason for coupling pump light with only specific divergence angles into the test fiber is the advantage of being able to investigate the effect of high NA pump light without any low NA pump light present.

With an iris diaphragm between the two lenses the maximum divergence angle can be controlled such that several different divergence angles

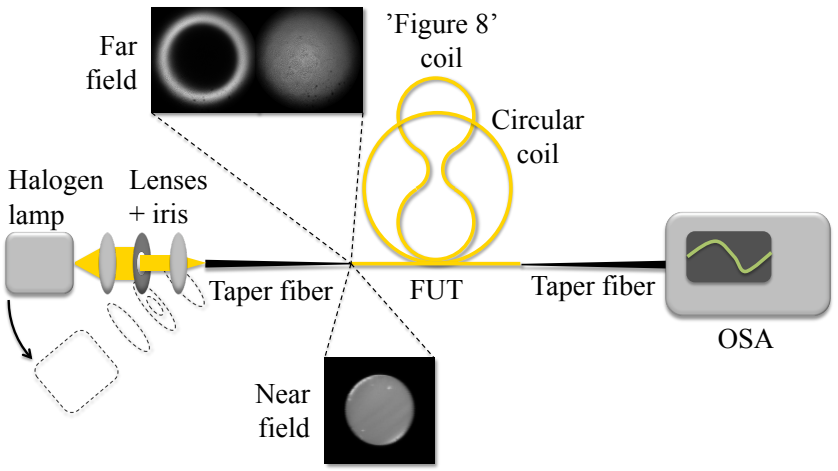

Figure 5.2: Experimental setup for measuring the NA dependent pump absorption of an ytterbium-doped high NA fiber. The left taper fiber produces a flat near field pattern and a ring structured far field pattern where the NA depends on the angle of the incoupling optics. During the pump absorption measurement the fiber is coiled either in a circular coil or in a 'figure 8' coil in order to suppress skew rays.

can be investigated. Figure 5.3 shows the different output far field patterns which can be produced using this coupling scheme. The images correspond to NAs between 0.17 and 0.7 measured at 950 nm. The near field image shown in the bottom insert of figure 5.2 is flat for all the different coupling angles and iris settings.

The output of the taper fiber is butt-coupled to 5 m of active high NA fiber, which in turn is butt-coupled to the high NA end of a taper fiber. The low NA output end of the taper fiber is connected to an OSA. The second taper fiber is added to the setup because the OSA has an acceptance angle below the divergence angle of the double-clad fibers. The pump absorption is measured in dB/m using the cut-back method as in [69], where the absorption spectrum is recorded after each cut-back, keeping the launch conditions unchanged.

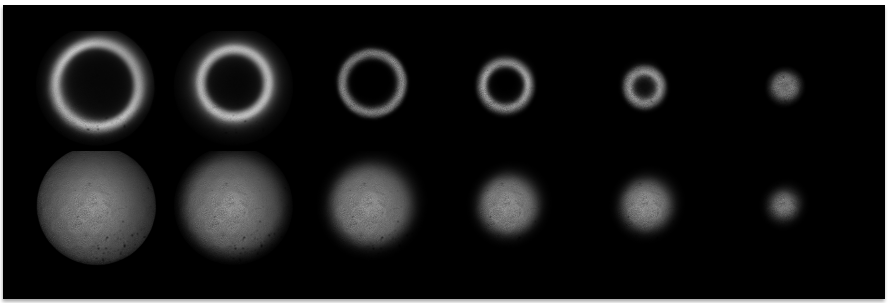

Figure 5.3: Different output far field patterns which can be produced using the angled and straight coupling schemes. The images correspond to NAs between 0.17 and 0.7 measured at 950 nm.

Pump absorption and 976 nm reemission

The first pump absorption measurement is performed as a reference on a 17 m long large core airclad PCF in a circular coil with a diameter of 25 cm. The measurement is performed with straight coupling into the taper fiber and without iris – that is, with an overfilled NA which is standard procedure for this type of fiber. The fiber is cut in 11 steps. Before the first cut-back and after every cut-back a transmission spectrum is recorded. Figure 5.4 shows the 12 transmission spectra. The green dots point to transmission values at the wavelength 915 nm, the blue dots to 940 nm and the red dots to 976 nm. For each of the three wavelengths the transmission values are plotted as a function of fiber length as shown in figure 5.5, and the pump absorption is subsequently determined by the slope of the plots. From figure 5.5 it is evident that the pump absorption at 915 nm is only linear at fiber lengths shorter than 6–7 m. The nonlinear behavior at longer lengths is due to skew rays, however, the level of this unabsorbed light is very low for all practical purposes. For 915 nm and 940 nm the nonlinear behavior start below -20 dB when 99% of the light has been absorbed. The pump absorption at 915 nm is 3.2 dB/m in the linear region, which means that for laser applications a realistic length of this fiber is shorter than 5 m.

At 976 nm the theoretical value of the pump absorption is $\sim$3.2 times larger than at 915 nm according to the absorption cross section – around 10 dB/m for this fiber. However, the measured value is far below that value and is seen to decrease with length even for very short fiber pieces. In

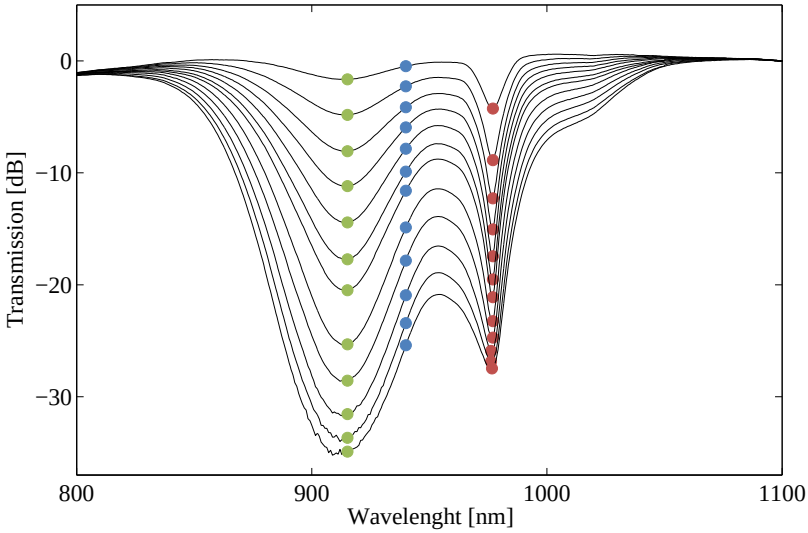

Figure 5.4: Transmission spectra for the 12 different fiber lengths of a cut-back measurement. The green dots point to the transmission values at the wavelength 915 *nm*, the blue dots at 940 *nm* and the red dots at 976 *nm*

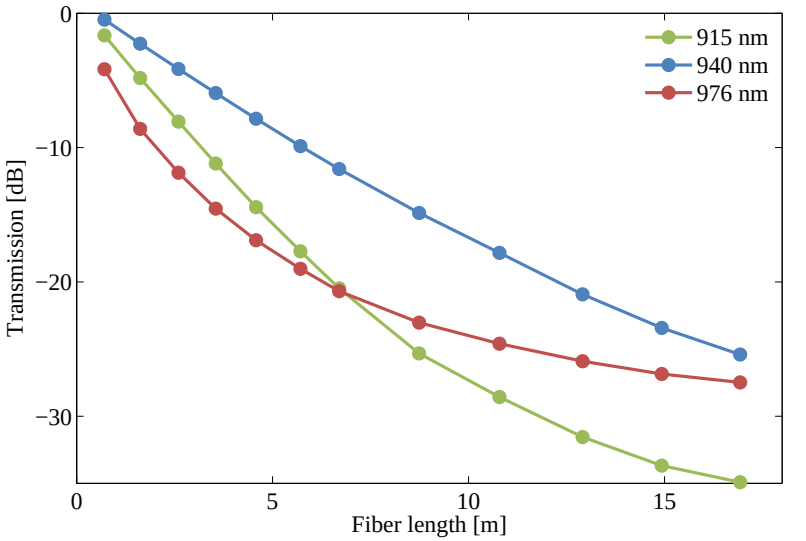

Figure 5.5: Transmission as a function of fiber length for the wavelengths 915 *nm*, 940 *nm* and 976 *nm*. The pump absorption is determined by the slope of the plots and is seen to decrease with length.

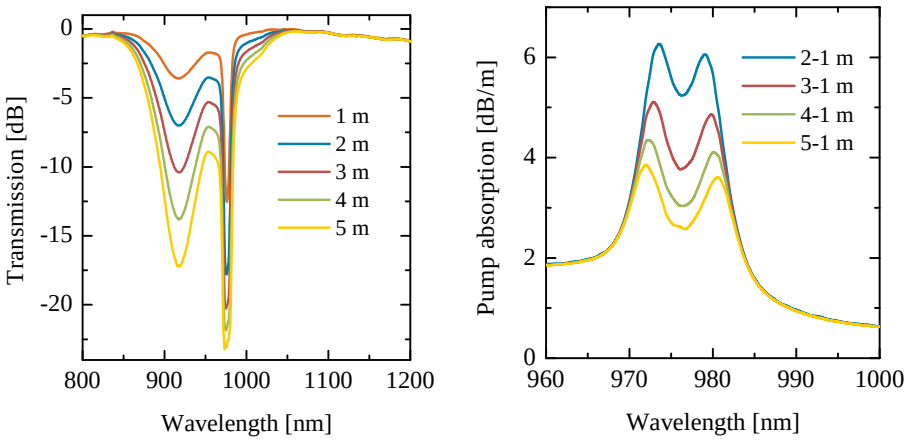

(a) (b)

Figure 5.6: (a) Transmission spectra for 5 different fiber lengths. (b) Pump absorption for 4 different fiber lengths calculated according to equation 5.1. The pump absorption is seen to decrease with length.

figure 5.6 we take a close look at this phenomenon. Figure 5.6(a) shows the transmission spectra at five different fiber lengths of the same fiber. The pump absorption α is calculated for each of the fiber pieces according to

$$\alpha = \frac{P_n - P_1}{l_n - l_1}, \tag{5.1}$$

where P_n is the transmitted power and l_n is the length of the n^{th} fiber piece. The pump absorption in the wavelength region around 976 nm is shown in figure 5.6(b) – it is seen to be well below the nominal 10 dB/m and to decrease for longer fiber lengths. Furthermore, the pump absorption spectra show a dip in the center which is due to reemission of pump light at the zero-phonon wavelength 976 nm.

It has to be emphasized that the decrease in measured pump absorption due to reemission is an artifact of the measurement and not the fiber or the material. The dip in the pump absorption only appears when the population inversion is very high, which is the case when the fiber is pumped without a seed signal since much of the absorbed pump light

will be stimulated to reemit at 976 nm. The amount of reemission scales with the fiber length and will lead to a decrease in the measured pump absorption per meter when the fiber length is increased. Introducing a seed signal will decrease the population inversion and stimulate transmission at the laser wavelength rather than the zero-phonon wavelength 976 nm. Subsequently, the measured pump absorption will increase to the expected levels. For that reason the pump absorption at 976 nm is always specified as a multiple of the pump absorption at 915 nm rather than the measured value.

Numerical aperture dependency

The aim of the second part of the investigation is to evaluate the influence of the pump light NA on the pump absorption of ytterbium-doped high NA fibers, in order to identify if low NA skew rays are disposed to higher losses and to which extend the hole structure in photonic crystal fibers is able to scramble these skew rays. Measurements are performed with two ytterbium-doped, high NA fibers in both circular coil and in 'figure 8' coil as illustrated in figure 5.2. One fiber is a PCF with a 40 μm core and a 200 μm pump cladding with a four period hexagonal lattice structure of airholes, a cladding pitch of 10 μm and a relative hole size of 0.1. The NA of 0.61 is determined by the airclad bridge width. The second is a step-index fiber with a 20 μm core, a 150 μm pump cladding and an NA of 0.60. The two fiber designs are illustrated in figure 5.7. Figure 5.7(a) shows the PCF, while figure 5.7(b) shows the step-index fiber.

Pump absorption measurements with two cut-backs for the two fibers using pump light with a ring structured far field, corresponding to an NA of 0.20, are shown in figure 5.8 for both circular and 'figure 8' coils. Very little effect of periodic bending is found for the PCF in figure 5.8(a), while the periodic bending more than doubles the absorption in the step-index fiber in figure 5.8(b). A slightly different doping concentration in the two fibers explains the difference in shape and extrema of the two absorption spectra.

In an additional experiment, 5 m pieces of the two fibers are cut back in 7-9 steps and pump absorption measurements are repeated for six different ring structured far field patterns, corresponding to NAs in the range 0.18-0.51. All ring structures have a FWHM of 0.07. Pump

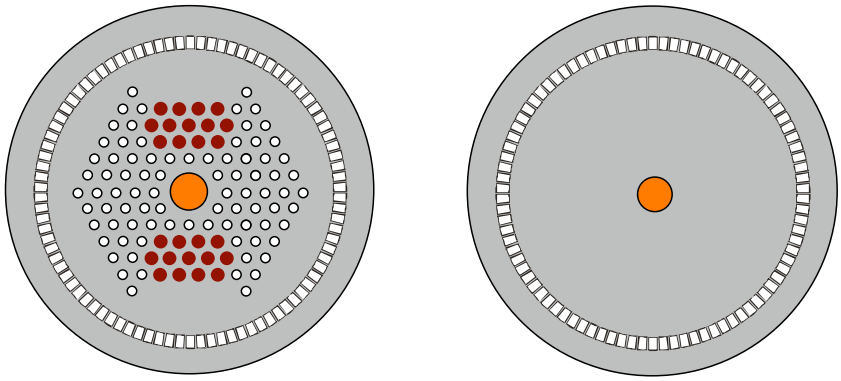

(a) (b)

Figure 5.7: Illustration of the two types of airclad fiber used in the second experiment. (a) The first fiber is a PCF with a 40 μm core and a 200 μm pump cladding. (b) The second fiber is step-index fiber with a 20 μm core and a 150 μm pump cladding. Both fibers have an NA of ∼0.6.

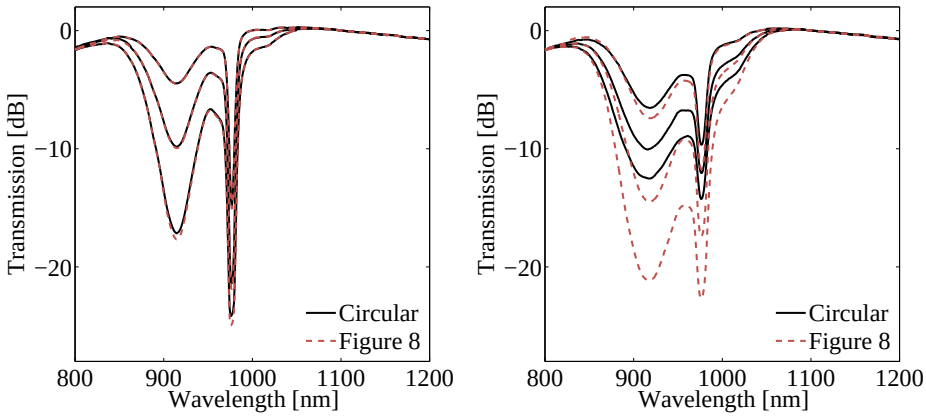

(a) (b)

Figure 5.8: Absorption spectra for (a) the PCF and (b) the step-index fiber in circular (black solid) and 'figure 8' (red dashed) coils. The skew ray suppressing effect of the periodic bending is only effective for the step-index fiber, while skew rays are already suppressed in the PCF.

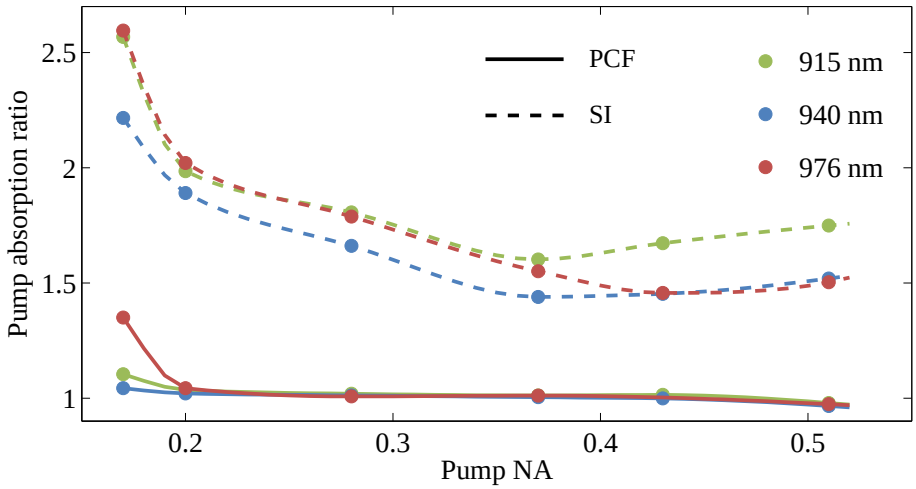

Figure 5.9: Ratio between the measured pump absorption using a 'figure 8' coil and a circular coil for the step-index fiber (dashed curve) and the PCF (solid curve) as a function of pump light NA at 915 *nm* (green), 940 *nm* (blue) and 976 *nm* (red).

absorption was measured for both fibers in circular and 'figure 8' coils. The ratio of the pump absorption using 'figure 8' coiling to the pump absorption using circular coiling is shown in figure 5.9 as a function of pump light NA. Measurements are shown for the PCF and the step-index fiber at the relevant pump wavelengths 915 *nm*, 940 *nm*, and 976 *nm*. Results show that for a PCF the ratio is close to unity except for a slight increase at very low NAs. This confirms the efficient skew rays scrambling effect of the hole structure in the PCF. For the step-index fiber the ratio is much higher for all NAs and an increase from 1.5 to 2.5 is observed as the NA decrease. The results suggest that especially low NA light is only efficiently absorbed in a step-index fiber if some skew ray suppressing technique is used. For the step-index fiber the very slight increase in pump absorption ratio at high NAs and the discrepancy between the pump absorption ratios at different wavelengths can be attributed to measurement uncertainties.

Pump absorption in step-index fibers with scrambler holes

Observations from the comparison between the step-index fiber and the PCF leads to the question whether a full PCF structure is necessary or if a small

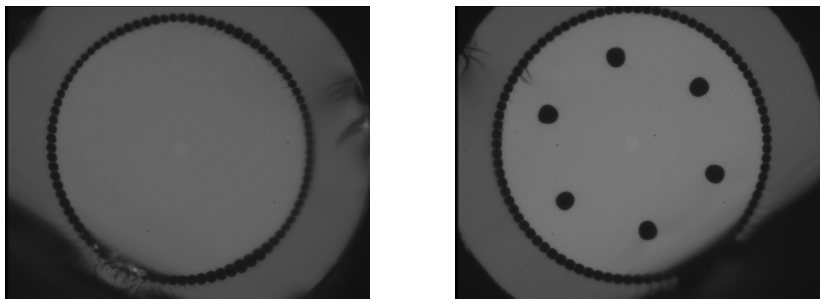

(a) (b)

Figure 5.10: Microscope images of two identical step-index airclad fibers, where fiber (a) has a standard pump cladding, while fiber (b) has 6 scrambler holes placed symmetrically in the cladding.

amount of larger scrambler holes is enough to create a chaotic beam path in the fiber as suggested in [66], for example, in cases where a step-index structure is preferred over a PCF structure. Pump absorption measurements are performed with the two step-index fibers shown in figure 5.10, which both have an 8 μm core and a 120 μm pump cladding. The fiber in figure 5.10(a) has a standard pump cladding while the fiber in 5.10(b) has 6 scrambler holes placed symmetrically in the cladding. The nominal pump absorption in both fibers are $\sim$1 dB/m at 915 nm and the measurements are performed on 20 m long fiber pieces for which the pump absorption is linear at 915 nm. The measurements are done with straight coupling into the taper fiber and with a fully open iris diaphragm for both the circular and the 'figure 8' coil. A pump absorption ratio of $\sim$1.3 at 915 nm is measured for the fiber with scrambler holes and $\sim$1.5 for the fiber without scrambler holes, indicating that the scrambler holes do have an effect but that the effect is not as pronounced as the scrambling effect from the full PCF structure, which has a pump absorption ratio close to unity.

Pump absorption in a straight PCF

In the next part of the investigation we look at the difference between a straight and a circular coiled PCF. The reason for performing this experiment is to clarify whether unbendable PCFs such as rod-type PCFs will experience problems with skew rays. The pump absorption measurements are performed with straight coupling into the taper fiber. The ratio of the

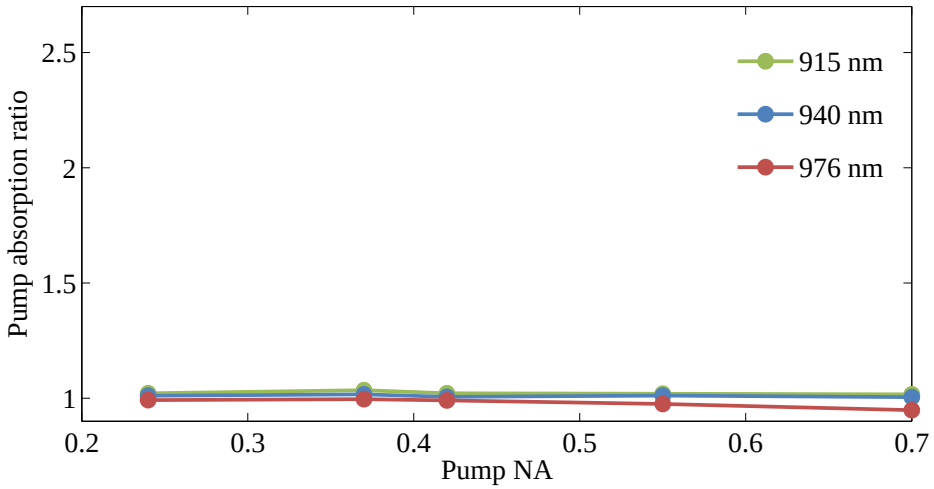

Figure 5.11: Ratio between the measured pump absorption using a circular coil and a straight PCF as a function of pump light NA at 915 *nm* (green), 940 *nm* (blue) and 976 *nm* (red).

pump absorption using circular coiling to the pump absorption of a straight PCF is shown in figure 5.11 as a function of pump light NA at the wavelengths 915 *nm*, 940 *nm*, and 976 *nm*. The pump absorption ratio is close to unity for all pump NAs, indicating that there is no significant effect of coiling the fiber and therefore a negligible amount of skew rays in the straight PCF.

Pump absorption in airclad and polymer clad fibers

In the last part of the investigation we look at the difference between the pump absorption in a polymer-clad fiber and an airclad fiber in order to understand whether the airclad itself has an effect on the scrambling of the skew rays. It has been suggested that the roughness on the boundary of the pump cladding in airclad fibers causes chaotic scattering of rays and that airclad fiber should scramble skew rays more efficiently than completely circular symmetric cladding structures, such as polymer-clad fiber [72]. On the other hand, it has also been shown theoretically that while the convex features of the airclad does promote some degree of chaotic dynamics, a highly circular symmetric airclad may not sufficiently scramble all low NA skew rays [66].

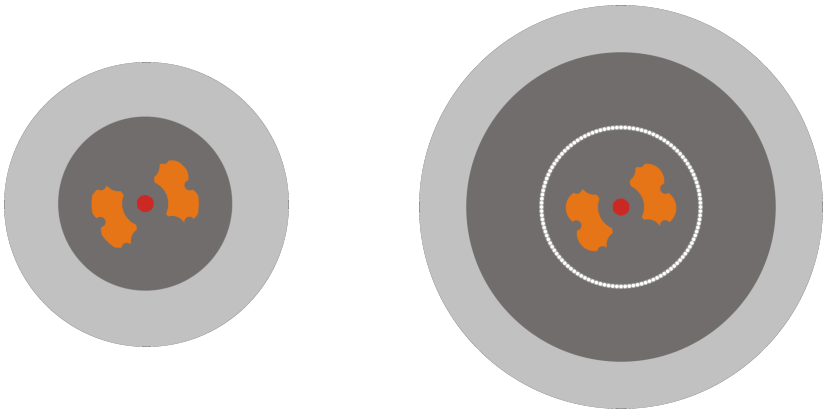

(a) (b)

Figure 5.12: Illustration of (a) a polymer clad fiber and (b) an airclad fiber. Both fibers have identical inner cladding regions with a 15 μm step-index core and a 250 μm pump cladding. The orange regions in the fiber drawing are stress elements.

The two fibers in the experiment are identical except for the over-cladding structure. They are illustrated in figure 5.12. They both have a 15 μm step-index core and a 250 μm pump cladding and the orange regions in the fiber drawings are stress elements. Figure 5.12(a) is an illustration of the polymer-clad fiber and figure 5.12(b) is an illustration of the airclad fiber. Pump absorption measurements are performed with both straight and angled coupling into the taper fiber and the ratio between the pump absorption in a 'figure 8' coil and in a circular coil is plotted for the wavelength 915 nm in figure 5.13. The results show no significant difference between airclad and polymer clad fibers, supporting the theoretical conclusions from [66]. Furthermore, since the pump absorption ratio is above unity there is a small amount of skew rays in both fibers, and based on the measurements with angled coupling it can be confirmed that the skew rays are due to low NA light. The fact that both fibers show a relatively low pump absorption ratio of $\sim$1.3 compared to the step-index fiber in figure 5.9 is due to the presence of the large regions with stress elements.

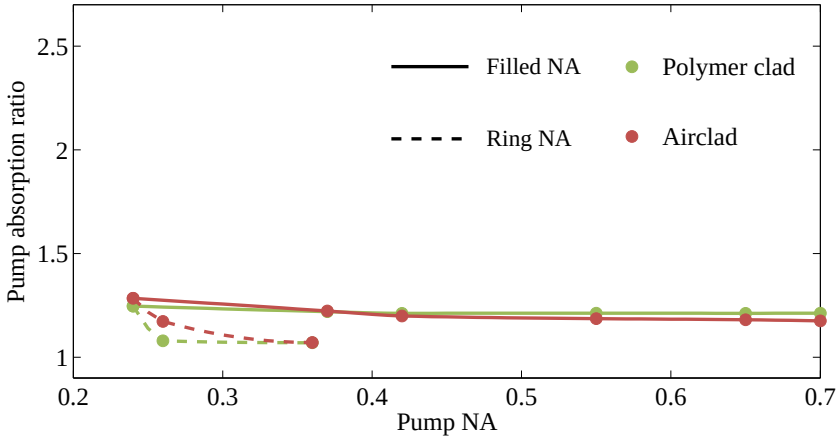

Figure 5.13: Ratio between the measured pump absorption using a 'figure 8' coil and a circular coiled for both a polymer-clad fiber (green) and an airclad fiber (red) and with both filled (solid curve) and ring (dashed curve) structured far field coupling.

Summary

The investigation has shown that rays without a significant overlap with the core are less efficiently absorbed in a step-index airclad fiber compared to a PCF. Especially low NA skew rays remain unabsorbed. Periodic bending of a PCF has very little influence on the pump absorption, suggesting that the skew rays are inherently suppressed by the airhole structure. The skew ray suppressing effect combined with a large core makes PCFs well suited for high power applications. Periodic bending of a step-index fiber improves the pump absorption overall but especially for low NA pump light by more than a factor of two, suggesting that without any skew ray scrambling mechanism, cladding-pumping of step-index airclad fibers can be very inefficient. This is very relevant for high power applications as coiling of the fibers play a significant role when packaging and thermal handling is to be optimized in the manufacturing of high power lasers and amplifiers. The scrambling effect of a small amount of holes in a step-index fiber have also been investigated and is found to be somewhat effective, with an improvement of 0.2 in the pump absorption ratio compared to a step-index fiber, but not as effective as a full PCF structure – these fibers still benefit from a 'figure 8' coil. In addition, results indicate that even straight PCFs do not suffer from

problems with skew rays. This is relevant for rod-type PCFs which cannot be bend to an extend that would scramble the skew rays. Finally, results have shown that there is no significant difference between polymer-clad and airclad fibers – i.e. that the airclad itself has no influence on the skew rays – and that stress elements in the cladding have a scrambling effect similar to the effect of a few scrambler holes.

5.2 Flexible fibers

As previously mentioned, in order to reach the highest powers, the core area of the fiber needs to be large, since the optical intensities would otherwise become too high. Although the possibilities to scale the core of a PCF is superior to those of a standard step-index fiber, the scaling entails challenges with respect to mode quality and stability. Two large core fibers have been investigated in this section, both containing stress rods. The presence of stress rods in the fibers induce a cladding index difference between the direction parallel to the stress rods and the direction perpendicular to the stress rods and as a consequence, the bend sensitivity in the two directions differ substantially. If the stress rods are not parallel to the bend plane, the beam quality and stability is considerably reduced.

The following section contains a description of how single-mode operation is investigated for coiled fibers in an amplifier configuration and a discussion of the importance of correct coiling of the fibers. Secondly, the section contains a description of how the output stability is investigated and how the stability is strongly effected by coiling and the correct orientation of the stress rods. Finally, the section contains a description of a fiber design in which the stress rods fall naturally into the optimum position when the fiber is coiled.

Fiber design

The first fiber is the DC-200-40-PZ-Yb fiber which is an ytterbium-doped airclad fiber with a signal core diameter of 40 μm and an inner cladding diameter of 200 μm. It features a mode area of more than 650 μm^2 while retaining single-mode beam quality. Moreover, the fiber is polarizing, resulting in improved PER compared to normal polarization-maintaining fibers due to the increasing attenuation of the wrong polarization. The second fiber is the

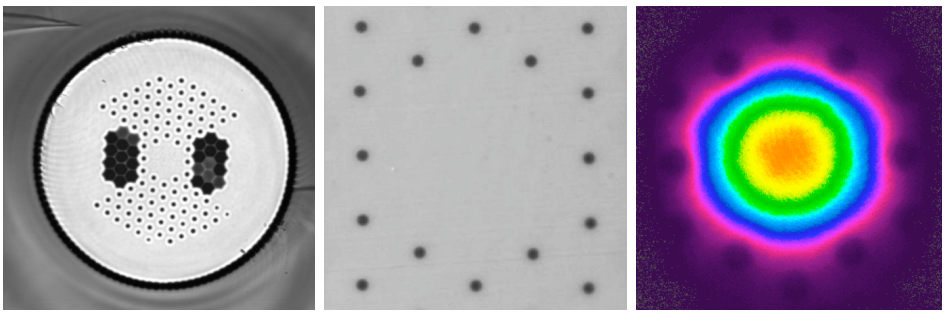

(a) (b) (c)

Figure 5.14: Fiber characteristics of the DC-200-40-PZ-Yb fiber. (a) Optical microscope image of the whole structure, (b) the structure immediately surrounding the core, and (c) a near field image recorded at 1064 nm. The mode field diameter is measured to 30 μm resulting in a mode field area of 650 μm^2. The characteristics of the DC-150-30-PM-Yb are downscaled compared to the DC-200-40-PZ-Yb fiber but otherwise identical.

DC-150-30-PM-Yb fiber, which is a downscaled version of the DC-200-40-PZ-Yb fiber. The signal core diameter is 30 μm and the inner cladding diameter is 150 μm. It features many of the same properties: large mode area, good PER, and single-mode beam quality, but is polarization-maintaining and designed for a smaller coiling diameter for applications where a smaller package size is needed. The fiber characteristics of the DC-200-40-PZ-Yb fiber is shown in figure 5.14. 5.14(a) showns an optical microscope image of the whole structure, 5.14(b) the structure immediately surrounding the core, and 5.14(c) a near field image recorded at 1064 nm. The mode field diameter is measured to 30 μm. The properties of the two fibers are summarized in table 5.1.

Active characterization setup

It is a great challenge to obtain as large a core as possible combined with the smallest possible coiling diameter, with single-mode operation, and with a sufficiently high slope efficiency and PER. For that reason each new fiber design has to be tested in an amplifier configuration. The setup in figure 5.15 is a general amplifier setup used for all flexible ytterbium-doped fibers. The setup entails 1064 nm CW seed system with an output power of approximately 1 W. The collimated seed is coupled through an optical isolator

Table 5.1: Overview over the optical and physical properties of the two fibers of the investigation.

Fiber	**DC-200-40-PZ-Yb**	**DC-150-30-PM-Yb**
Optical properties		
Signal core		
Mode properties	Single-mode	Single-mode
M^2 @ 1064 nm	< 1.3	< 1.25
Mode field diameter	$\sim$29 μm	$\sim$22 μm
Mode field area	650 μm^2	380 μm^2
NA @ 1064 nm	$\sim$0.03	$\sim$0.04
Multimode pump core		
Numerical aperture @ 950 nm	0.55	0.6
Pump absorption @ 920 nm	$\sim$3 dB/m	$>$3 dB/m
Pump absorption @ 976 nm	$\sim$10dB/m	$\sim$10dB/m
Polarization parameters		
Birefringence Δn	$1 \cdot 10^{-4}$	$1{\cdot}10^{-4}$
Polarization extinction ratio	$>$15 dB	$>$15 dB
Physical properties		
Signal core diameter	40 μm	30 μm
Inner cladding diameter	200 μm	150 μm
Outer cladding diameter	450 μm	330 μm
Coating diameter	650 μm	440 μm
Outer and inner cladding material	Pure silica	Pure silica
Coating material, single layer	HT acrylate	HT acrylate

and into the test fiber (FUT). The input polarization can be rotated by a $\lambda/2$-plate. The test fiber is pumped backwards by six 915 nm diodes. The signal output from the test fiber is collimated and coupled out through a long-wave pass filter (PR), which transmits the signal wavelength and reflects the pump. A short-wave pass filter (SR) is placed between the pump reflector and the pumps for protection the diodes against pulses. The signal output is send via a second short-wave pass filter to a power meter for slope efficiency measurements, while a small fraction of the light is coupled to a CCD camera by a 1% beam sampler (BS). An iris diaphragm (I) is placed before the power meter to ensure that only core light is measured. All lenses in the setup is chosen according to the fiber collimation equation

$$f = \frac{\pi d(MFD)}{4\lambda}, \tag{5.2}$$

where f is the focal length of the lens, d is diameter of the collimated beam between two lenses, and MFD is the mode field diameter of the test fiber core mode.

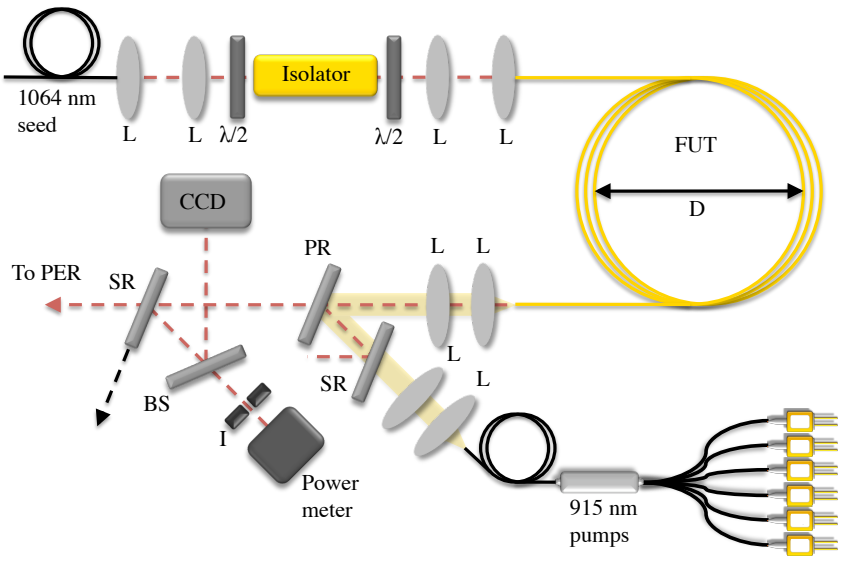

Figure 5.15: Schematic illustration of the setup for characterization of large core flexible fibers in a backward pumped amplifier configuration.

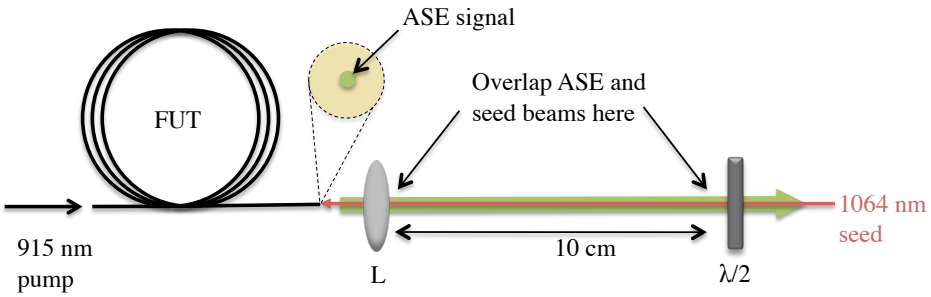

Figure 5.16: Illustration of the seed coupling procedure where an ASE signal from the test fiber core is overlapped with the seed beam.

Coupling of the seed has proven to be cumbersome when the core size is large and the core NA becomes increasingly small, and in order to facilitate the coupling a simple procedure has been developed. The seed coupling procedure is illustrated in figure 5.16. When a small fraction of pump light is coupled through the test fiber, an ASE spot can be observed from the seed input end of the test fiber. A lens is inserted immediately before the seed input end, reducing the divergence of the ASE spot. The seed light is collimated using a set of lenses, coupled through the isolator and the polarization of the light is rotated to the slow axis of the fiber using the $\lambda/2$-plate. The ASE spot and the seed beam are now made to overlap at two separate points e.g. close to the test fiber and close to the isolator. Subsequently, the last lens is inserted and the two collimated beams are overlapped again. Seed coupling can finally be optimized for maximum power in the core.

Single-mode operation

To get more robust guidance and more compact devices, standard double-clad fibers are often designed to be multimode when operated uncoiled. Coiling the fiber on a spool introduces macro-bending loss which will be higher for the less tightly bound higher-order modes, whereby one can strip them and improve the beam quality [73]. This kind of mode tuning requires a careful balance between bending radius and the induced losses,

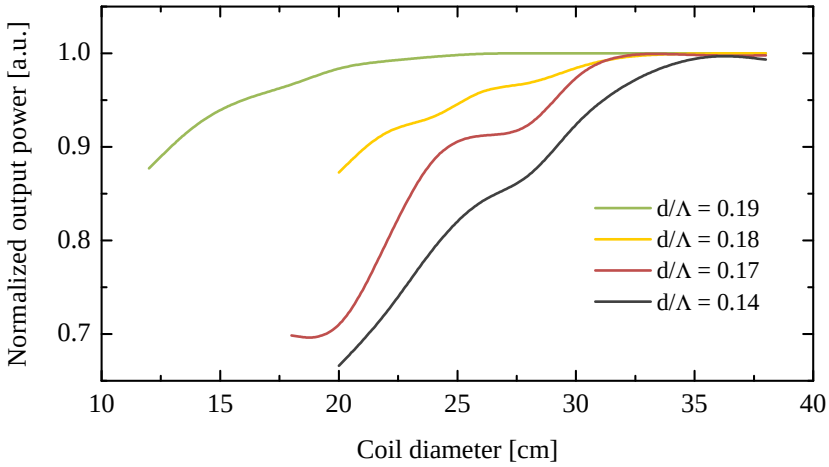

Figure 5.17: Normalized output power as a function of coil diameter for the DC-200-40-PZ-Yb fiber for four different relative hole sizes.

as too tight coils will also induce high losses for the fundamental mode and thereby reduce the efficiency of the laser. Due to preferential gain and the generation of light over the entire fiber length, the modal properties of a fiber laser or amplifier can be very different from the modes one would encounter with passive characterization of the fiber itself. Moreover, it is important to be able to easily quantify how much the higher order modes are suppressed compared to the desired fundamental mode – especially if one wishes to tune the modal properties by coiling. Furthermore, when coupling light to the fiber for passive mode characterization, part of the light will also be guided in the multimode pump-guide, thereby obscuring the modal properties of the core. For that reason all modal characterization is done in an amplifier configuration.

In figures 5.17 and 5.18 the normalized output power is measured as a function of coil diameter for the DC-200-40-PZ-Yb fiber design and the DC-150-30-PM-Yb fiber design, fabricated with several different relative holes sizes. In the measurements each fiber is coiled to the maximum diameter and subsequently squeezed from two sides, making the coil oval where the coil diameter denotes the minor diameter of the oval. This procedure is used in order to avoid a complete recoiling of the fiber and the subsequent

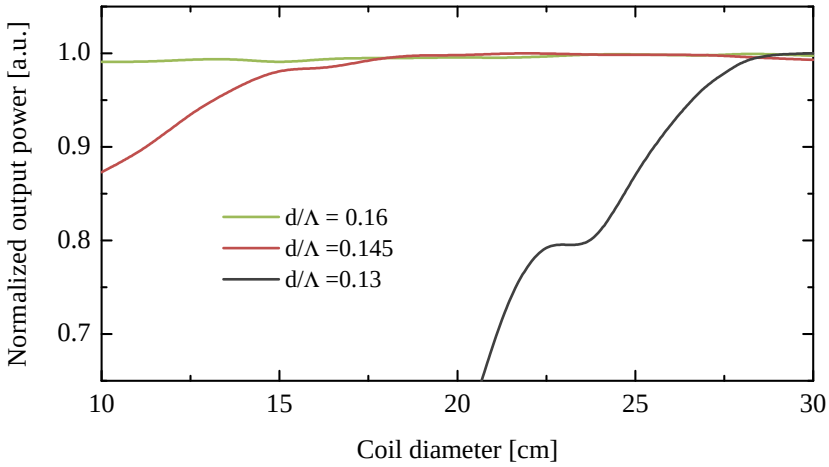

Figure 5.18: Normalized output power as a function of coil diameter for the DC-150-30-PZ-Yb fiber for four different relative hole sizes.

changes in seed and pump coupling, which would otherwise distort the measurement. The measurements are all done with approximately 1 W of seed power and 10 dB gain, and the output power is recorded, while the diameter is decreased in steps of $\sim$2 cm. Since the refractive index of the core material is only known with an accuracy of 10^{-5} and variations can occur, this type of measurement is used in the design process to fine-tune the index step by finding the optimum relative hole size for each new core material composition. If the fiber is fabricated with too large a relative hole size, the fiber will remain multimode even for small coil diameters. Moreover, if the fiber is coiled too tightly, the effective cladding index is raised on the outside of the coil, causing mode compression [74]. On the other hand, a fiber with too small a relative hole size will experience fundamental mode loss even at large coil diameters, making the fiber impractical for industrial application where compact packaging is an issue. For the DC-200-40-PZ-Yb fiber the optimum relative hole size is found to be 0.17-0.18 for a coil diameter of $\sim$ 30 cm, while for the DC-150-30-PM-Yb fiber the optimum relative hole size is found to be 0.14-0.15 for a coil diameter of $\sim$20 cm.

The mode index spacing in the DC-200-40-PZ-Yb fiber is on the order of 10^{-4}, however, if the flexible fiber design were to be scaled beyond

a 40 μm core size, the mode spacing would decrease significantly. Doubling the mode field diameter would decrease the mode spacing by an order of magnitude, making the fiber much more sensitive to macro- and micro-bending losses and essentially impossible to use, thus, for this type of flexible fiber design a 40 μm core size is close to being the limit. The rod-type fiber design, on the other hand, is mechanically stable and resistant to bend losses and can be used if the core size is to be scaled beyond 40 μm. This design will be described in more detail in a later section.

In the previous measurements the fibers are always coiled with the stress rods in the bend plane. Young's modulus of the boron rods, comprising the stress elements in the fiber, is typically 60-64 GPa, whereas Young's modulus of fused silica is 73 GPa. Therefore the fiber should naturally coil in the plane parallel to the stress rods if no other asymmetries are affecting the stress and strain properties of the glass [73]. In addition to providing birefringence and a naturally preferred bend direction, the presence of the stress rods are also responsible for an anisotropic NA with a difference of $\sim$0.005 between the NA in the direction parallel to the stress rods compared to the other direction, due to the lower index of boron-doped rods as $n_b = n_{si} - 0.006$. Therefore, if the fiber were to be coiled in the plane perpendicular to the stress rods the mode losses would increase compared to the other direction, as modes are better confined in the direction with the higher index step.

Even if the fiber is coiled properly with respect to the orientation of the stress rods, the difference in bend sensitivity in the two orthogonal planes has to be considered for handling of the input and output end of the fiber in packaging of the full system. A DC-200-40-PZ-Yb designed for a coil diameter of 30 cm with the stress rods parallel to the bend plane, will only be able to operate with a bend diameter of 40–45 cm in the out-of-plane direction as illustrated in figure 5.19. The out-of-plane bend diameter has been measured by coiling a DC-200-40-PZ-Yb fiber with the stress rods perpendicular to the bend plane and measuring the amplified output power as a function of coil diameter. The measurement result is shown in figure 5.20, where the output power of a fiber with stress rods parallel to the bend plane starts to decrease at around 30 cm, while the output power of a fiber with stress rods perpendicular to the bend plane starts to drop at around 40 cm. In both cases the polarization of the seed

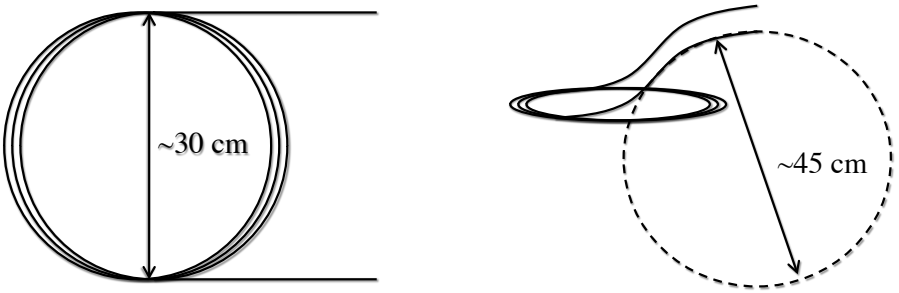

Figure 5.19: Illustration of the recommended coil diameter for both (a) in-plane coils and (b) out-of-plane bends.

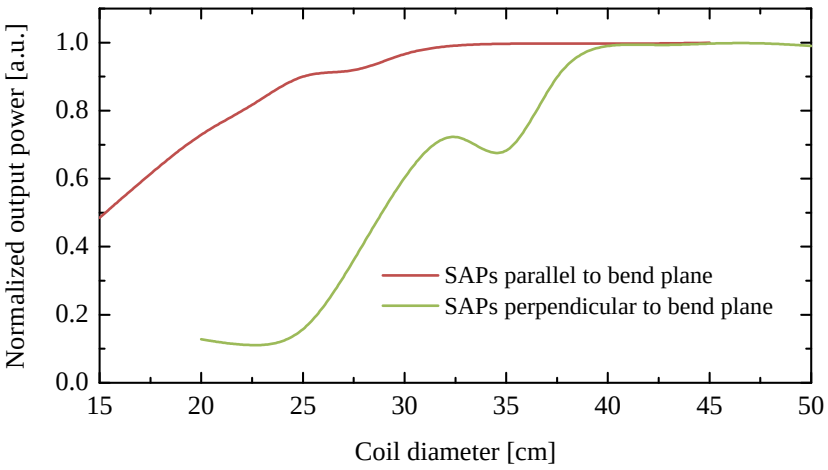

Figure 5.20: Normalized output power as a function of coil diameter for a fiber with the stress rods parallel to the bend plane (red curve) and a fiber with the stress rods perpendicular to the bend plane (green curve). In both cases the seed light polarization is aligned parallel to the slow axis of the fiber.

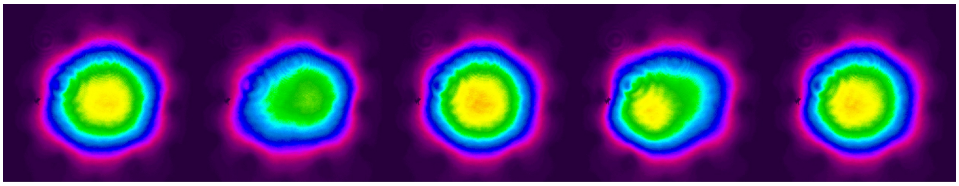

Figure 5.21: Near field images of the output from the DC-150-30-PM-Yb fiber coiled to a diameter of 30 *cm*. In the images the seed coupling is scanned in the x-direction. The fiber clearly supports at least one higher order mode at this coil diameter. The holes of this particular test fiber are slightly too large, as the target coil diameter of the fiber design is 20–30 *cm*.

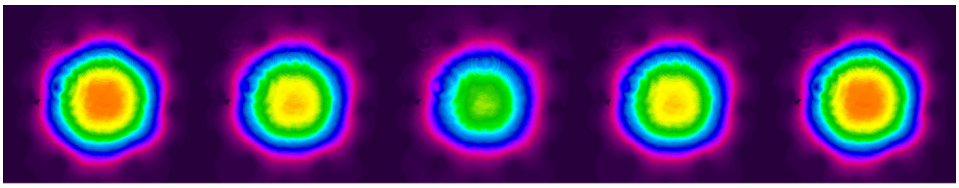

Figure 5.22: Near field images of the output from the DC-150-30-PM-Yb fiber coiled to a diameter of 20 *cm*. In the images the seed coupling is scanned in the x-direction. The fiber does not support higher order modes at this coil diameter.

light is aligned with the slow axis of the fiber.

A commonly used qualitative method to determine if a fiber is single-mode or multimode at a specific coil diameter is to observe the near field image when the seed incoupling is scanned in both the x- and the y-direction. If the center of mass in the image is constant during the procedure and the output is overall attenuated, the fiber only supports a single mode, while a moving center of mass indicates that the fiber also supports higher-order modes. In figures 5.21 and 5.22 near field images of the output from the DC-150-30-PM-Yb fiber have been recorded by a CCD camera while the seed input coupling has been changed in the x-direction. In figure 5.21 the fiber was coiled to a diameter of 30 *cm* and the images clearly indicate that the fiber supports at least one higher-order mode in this particular coil configuration. The shifted center of mass reveals a superposition of the LP01 and LP11 modes. In figure 5.22 the fiber is coiled to a diameter of 20 *cm* and in this coil configuration the fiber displays overall attenuation and no center of mass movement, indicating that the fiber only supports

the fundamental mode. The holes of this particular test fiber are slightly too large, as the target coil diameter of this fiber design is 20–30 *cm*. While the measurement of the output power as a function of coil diameter mainly determines the lower limit of the coil diameter, this type of qualitative measurement is performed on the fibers in order to determine the upper limit of the coil diameter.

Output stability

Besides single-mode operation and enough output power in terms of slope efficiency another very important issue is the stability of the output. When the fiber is operating in the multimode regime, external perturbations to the fiber such as tapping or poking at the fiber will result in coupling between the different modes present in the fiber and the mode becomes unstable. In the single-mode regime the fiber is ideally insensitive to these external perturbation and both the output power and the mode profile will remain unaffected. When the fiber is coiled to a point where the fundamental mode loss starts to increase the fiber will again become sensitive to external perturbations.

Due to packaging restrictions, one might wish to coil the fiber tighter than the limit posed by the measurement of the output power as a function of coil diameter, knowing that the output power will be slightly lower. This is possible, but only as long as the output is stable to perturbation. Thus, the output stability provides an absolute lower limit to the coil diameter of the fiber. In figures 5.23 and 5.24 the output power from two versions of the DC-150-30-PM-Yb fiber has been recorded while the coil diameter has been reduced in steps of 1.25 *cm*. The fibers were tapped and poked heavily during the recording. Figure 5.23 shows that a DC-150-30-PM-Yb fiber with a relative hole size of 0.14 becomes unstable at a coil diameter of 15 *cm*, while a fiber with a relative hole size of 0.13 becomes unstable at a coil diameter below 25 *cm*. The stability and instability criteria are also based on observations of the near field using the CCD camera.

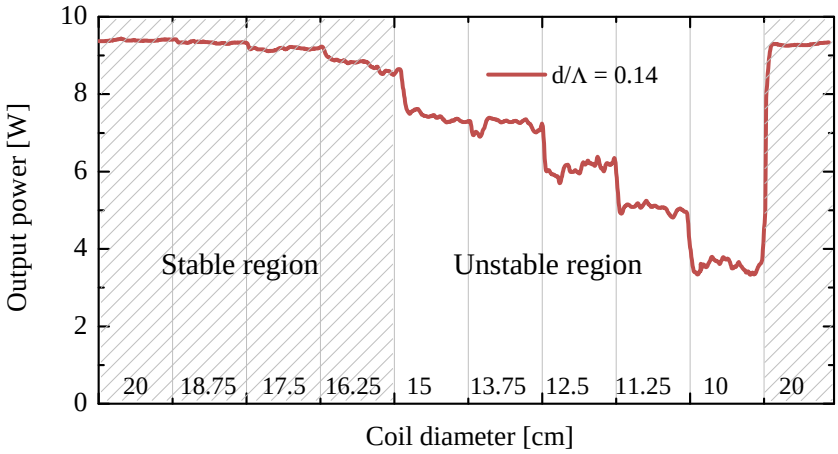

Figure 5.23: Output power of a DC-150-30-PM-Yb fiber with a relative hole size of 0.14. During the measurement the coil diameter was reduced in steps of 1.25 *cm* from 20 *cm* to 10 *cm* and back to 20 *cm* again, while the fiber was tapped and poked heavily.

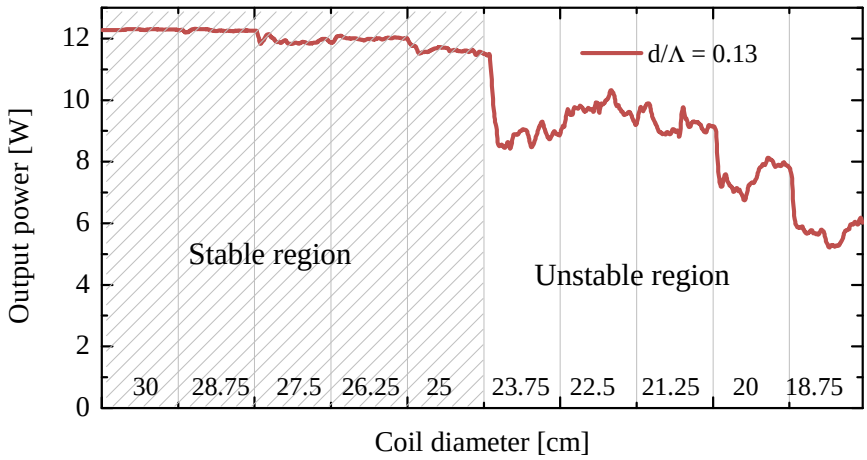

Figure 5.24: Output power of a DC-150-30-PM-Yb fiber with a relative hole size of 0.13. During the measurement the coil diameter was reduced in steps of 1.25 *cm* from 30 *cm* to 18.75 *cm*, while the fiber was tapped and poked heavily.

Figure 5.25: Graphic illustration of fiber twist. The stress rods (grey) twist around the fiber core (green) along the length of the fiber.

Fiber coiling

Since the output stability depends on the bend diameter, the stability becomes strongly dependent on the alignment of the stress rods with respect to the bend plane. As previously mentioned, the fiber ought to have a naturally preferred bend direction due to the difference in Young's modulus of boron and fused silica. This preferred bend direction is with the stress rods parallel to the bend plane, which is also the bend direction, where the fiber is the least bend sensitive due to the index. Ideal bending behavior requires a perfect symmetry in the fiber, which is not always present. Two issues have emerged in the process of optimizing the fiber design of the two large mode area fibers – fiber twist and fiber tilt, both of which affect the stability of the output negatively. Fiber twist is when the stress rods are twisting around the core along the length of the fiber as shown in figure 5.25. Twist is typically caused by asymmetrically applied pressure on the fiber during the drawing process and can be difficult to avoid all together. If the fiber is twisting more than 30° over the full length of the amplifier, the stress rods will no longer be sufficiently aligned to the bend plane in all parts of the fiber. As a result the fundamental mode will suffer from bend loss in some parts of the fiber, causing a reduction of the slope efficiency and an unstable output. If the fiber is coiled more loosely to compensate for the bend loss, the fiber will operate multimode in other parts of the fiber. As a consequence, twist in the fiber will either decrease the slope efficiency or impair the mode quality and introduce an overall instability to the output.

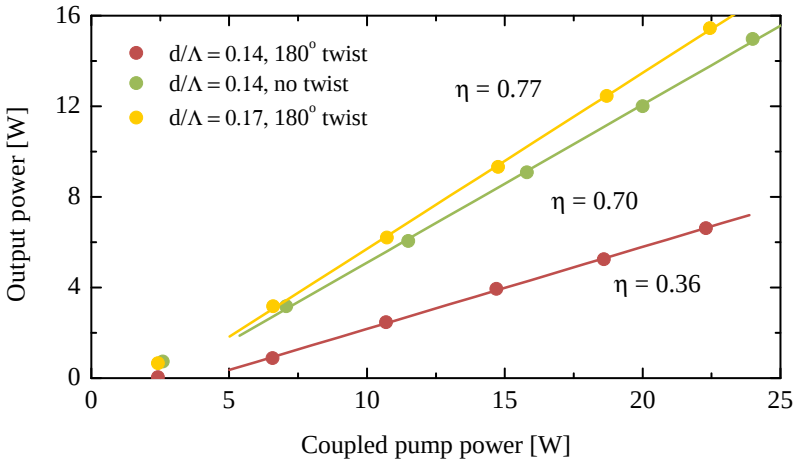

Figure 5.26: Normalized output power as a function of coupled pump power for two DC-200-40-PZ-Yb fibers. In the measurements the fibers have been forced into a 180° twist (red and yellow curves).

The degree of twist in a fiber can be measured by placing a 5 m piece of fiber straight on the ground without any bends. The orientation of the stress rods is measured every 1 m in a cut-back measurement by imaging the fiber end facet output with a CCD camera. A non-destructive twist measurement might be necessary for screening of fibers which are to be used in an amplifier. This can be done by imaging the two ends of the fiber instead of performing a full cut-back measurement, however this measurement cannot resolve twist in multiples of 180° over the length of the fiber or guarantee that the twist has not changed direction of rotation, in which case the twist will be underestimated.

Figure 5.26 shows the effect of twist on the slope efficiency for two versions of the DC-200-40-PZ-Yb fiber with relative hole sizes of 0.14 and 0.17. Both fibers are coiled at a diameter of 30 cm and are forced into a 180° twist, which means that the stress rods will pass the plane perpendicular to the bend plane once over a 5 m length. For the fiber with the larger hole size the slope efficiency is very high even with 180° twist, while for the fiber with the smaller hole size the slope efficiency drops to half. The dramatic drop in slope efficiency for the fiber with the smaller holes is due

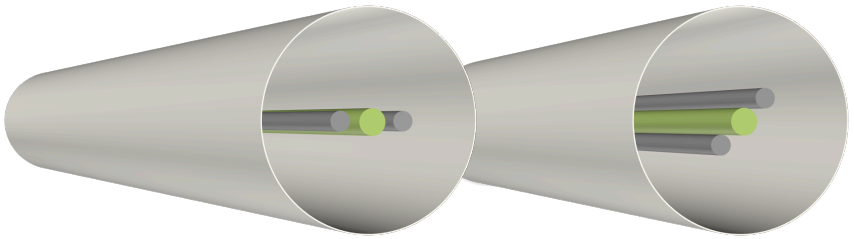

Figure 5.27: Graphic illustration of fiber tilt. The fiber to the left is without tilt. The fiber to the right is tilting – the stress rods (grey) are aligned at an angle with respect to the bend plane when the fiber is coiled.

the fact that the bend loss of the fundamental mode, when the stress rods are perpendicular to the bend plane, is much larger for this fiber compared to the fiber with the larger holes.

The issue of twist has been solved in the fabrication process, and the elimination twist in the fibers subsequently revealed the issue of fiber tilt. Fiber tilt is when the stress rods do not align themselves in the naturally preferred plane parallel to the bend plane, when they are coiled. Figure 5.27 is a graphic illustration of fiber tilt. The fiber to the left is without tilt, while the fiber to the right has a tilt of 45°. Tilt in the fiber can be due to some asymmetries in the outer cladding geometry or due to asymmetries in the heating and cooling process during the drawing process, causing uneven stress in the glass. The preferred bend direction is determined by the area momentum of inertia, and the ratio between the area moment of inertia in the two axis of an elliptical tube is given by a^2/b^2, where a and b are the lengths of the two axis, thus even small ovalities of a few percent will have a pronounced effect. When the tilt angle is above a certain value, the bend behavior changes significantly as indicated by the measurement in figure 5.20, where the output power is plotted as function of coil diameter for a fiber with horizontal stress rods and a fiber with vertical stress rods. The critical angle is found experimentally to be $\sim$30°. Without complete control of the tilt angle, designing and fabricating a fiber with optimum bending and mode properties becomes increasingly difficult.

Fiber tilt can be measured on a twist free fiber by coiling the fiber to the diameter of typical operation and measuring the orientation of the stress rods in a cut-back measurement similar to the twist measurement.

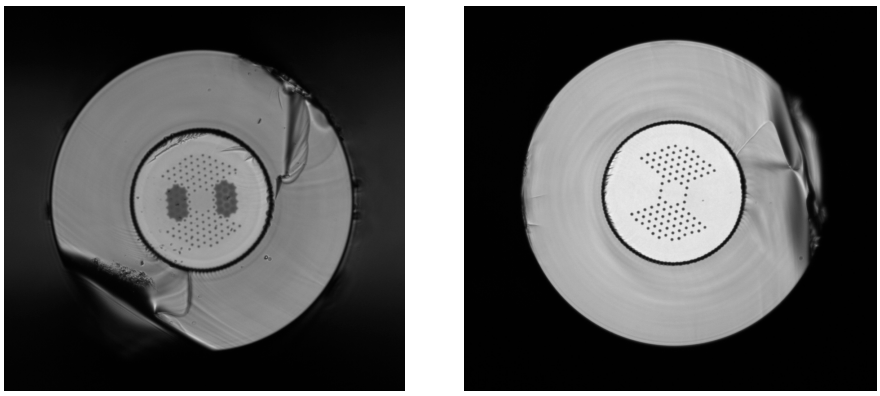

(a) (b)

Figure 5.28: Passive versions of the DC-200-40-PZ-Yb fiber (a) with stress rods and (b) without stress rods.

The degree of tilt can change through the length of the fiber, and therefore cut-back measurements are important in the test phase. A non-destructive tilt measurement for fiber screening can be done in a similar way to the twist measurement by coiling the fiber and imaging the two ends of the fiber.

In order to test the effect of the stress rods on the preferred bend direction, two passive versions of the DC-200-40-PZ-Yb fiber were fabricated with and without stress rods. Microscope images of the two fibers are shown in figure 5.28. As previously mentioned, the stress rods should impose a naturally preferred bend direction on the fiber due to the difference in Young's modulus for boron and silica. Simplified calculations of the effect of the stress rods on the bending stiffness indicate that in the current design of the DC-200-40-PZ-Yb as shown in figure 5.28(a) the lower Young's modulus of boron (62 GPa) may be counter balanced by the higher Young's modulus of the solid silica rods (73 GPa) on the outside of the stress rods compared to the silica tubes (71 GPa) constituting the hole structure. The effect of replacing the stress rods with solid silica rods as in figure 5.28(b) would induce difference of 3% in the bending stiffness, equivalent to a 1.5% ovality of the overcladding tube – an ovality which is not unusual to find. Thus, the assumption of a preferred bend direction may be contingent on the fiber having a sufficiently circular outer geometry.

Tests showed that replacing the stress rods with solid silica rods had no significant effect – positive or negative – on the tilt, indicating that other contributions supersede the effect of the stress rods. Removing the coating, on the other hand, had a pronounced effect, making the degree of tilt more constant over the length of the fiber. However, the tilt was still present without coating, indicating that the tilt effect is mainly from silica but with an additional coating contribution. Coiling the fiber directly after the drawing introduced additional tilt, which was partly removed by keeping the fiber straight for a period of time. This effect is most likely related to the plasticity of the coating and can be reduced by using larger spools or a thinner coating layer.

A solution to the tilt issue was found in the fiber design. Due to the large contributions from asymmetries, different fibers were fabricated with built-in asymmetry in the outer part of the overcladding . The asymmetry was made by polishing part of the circular overcladding tube flat before the drawing process, and the best results were obtained by polishing one side by 26 μm or by polishing two sides by half the value. The two fiber designs are shown in figures 5.29 and 5.30. By polishing one or two opposite sides the area momentum of inertia in one direction is reduced sufficiently for the fiber to prefer bending in that direction regardless of the stress rods alignment or coating irregularities. In both cases the ratio of the area momentum of inertia in the two directions is approximately 10%. The tilt angle measurements in figures 5.31(a) and 5.31(b) show a 0° tilt angle with very small deviations within measurement uncertainties for both fibers. With smaller polishing depths the tilt angle was more inconsistent.

The DC-200-40-PZ-Yb fiber is used in conjunction with a special curved mirror combiner [75], where 14 pump fibers are fused together around the fiber, and therefore the design with two polished sides from figure 5.30 is preferred, since the deformation of the circular shape is smallest. A microscope image of the double-polished DC-200-40-PZ-Yb fiber surrounded by 14 pump fibers for the curved mirror combiner is shown in figure 5.32.

Summary

This section described how large core fibers with different relative hole sizes are evaluated for mode quality and stability using an amplifier setup. By

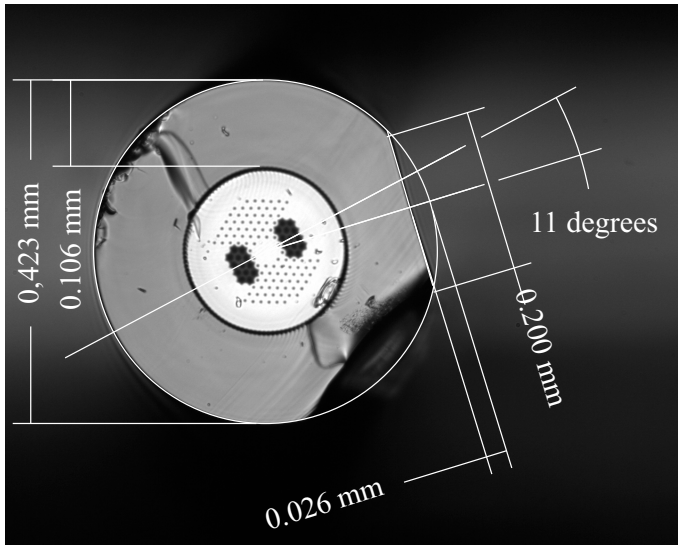

Figure 5.29: DC-200-40-PZ-Yb where one side is polished by 26 μm.

Figure 5.30: DC-200-40-PZ-Yb where two sides are polished by 13 μm.

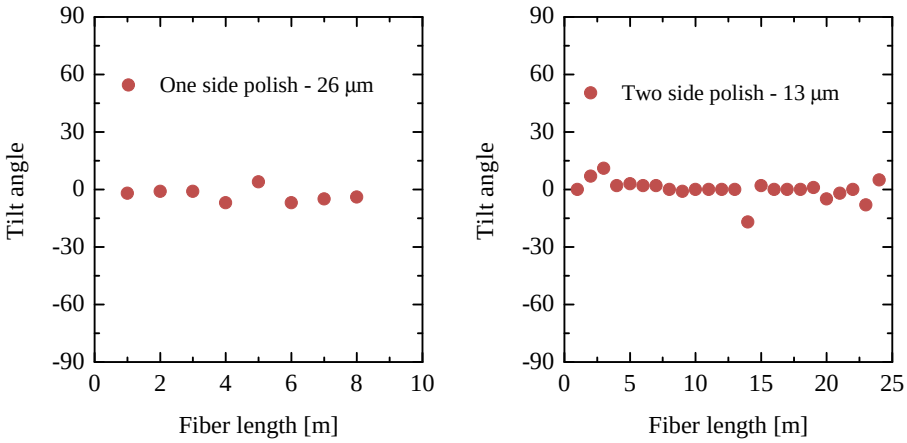

Figure 5.31: Tilt angle measurements of the DC-200-40-PZ-Yb with (a) one side polished by 26 μm and (b) two sides polished by 13 μm.

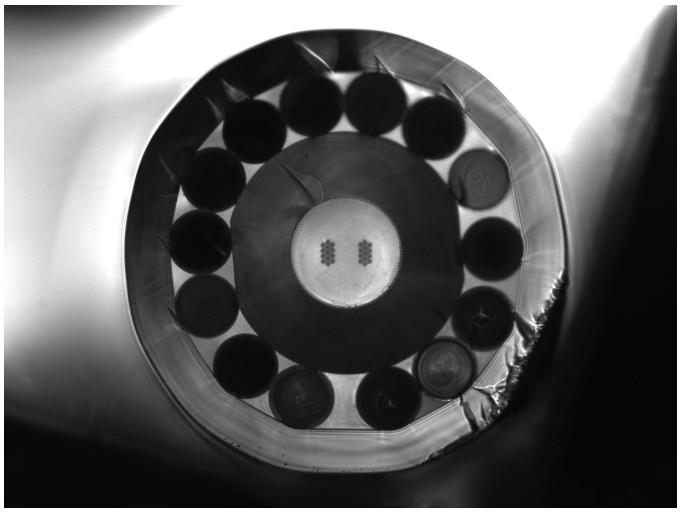

Figure 5.32: Microscope image the double-polished DC-200-40-PZ-Yb fiber surrounded by 14 pump fibers for the curved mirror combiner.

observing the output power, output stability, and center of mass movement as a function coil diameter, the design limits are found for which the fiber is operating single-mode at a practical coil diameter. For the DC-200-40-PZ-Yb a relative hole size of 0.17-0.18 and a coil diameter of 30 *cm* is optimum, while for the DC-150-30-PM-Yb a relative hole size of 0.14-0.15 and a coil diameter of 20 *cm* is optimum. These are some of the largest flexible fibers currently on the market. Furthermore, issues related to the orientation of the stress rods in coiled fibers – twist and tilt – have been described in this section. While fiber twist have been reduced by changes in the fabrication process, fiber tilt has been removed by a design modification of the outer cladding. The elimination of twist and tilt greatly improves the mode quality and stability of the large core fibers.

5.3 Rod-type fibers

As previously mentioned, nonlinear effects is the main limiting factor for the achievable power levels in a fiber amplifier or laser, and as some nonlinear effects are length dependent – such as SBS and SRS – it is critical to minimize the fiber length. Shorter fibers require higher pump absorption per meter, which can be realized by reducing the ratio between the pump core area and the signal core area and by increasing the numerical aperture of the pump guide. Alternatively, one can increase the concentration of rare earths incorporated in the core, but higher concentration has a negative effect on photo darkening and can lead to lower efficiency. Furthermore, extracting large amounts of power from short lengths of fiber requires very good thermal properties. The power extraction will normally be limited by damage of the polymer cladding found in standard double-clad fibers, while the air-glass design of the airclad fiber eliminates this problem. However, both polymer-clad and airclad fibers normally feature a protective coating, which can also be damaged at very high temperatures and reduce the cooling efficiency of the fiber due to the low thermal conductivity of the polymer. This problem can be overcome by simply removing the protective coating layer and instead make the fiber so thick that it has enough mechanical stability in itself without the protective coating layer. Moreover, the large outer diameter – typically 1–2 *mm* – mitigates other potential problems: macro- and micro-bending losses. When the core size is expanded beyond 40-50 μm, the index step is so small, that the bending radius needed for low loss operation becomes too large for practical systems,

but the large diameter of the rod-type fiber ensures the waveguide is not bend whereby low propagation loss is ensured. The pump absorption of the rod-type fibers is so high – typically on the order of 30 dB/m at 976 nm – that the system can often be realized with 50-70 cm of fiber making setups build with straight fiber pieces feasible. An illustration of a rod-type fiber design is shown in figure 5.33 next to an illustration of a traditional airclad fiber.

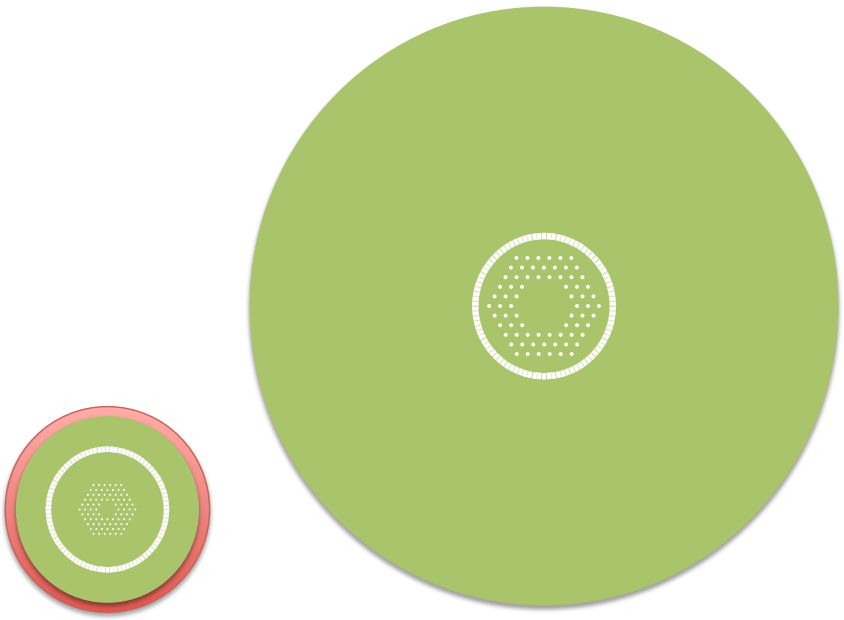

Figure 5.33: Illustration of a rod-type fiber design featuring an extremely large mode area core, a pump cladding comparable to a flexible large mode area PCF and an outer cladding with a diameter of up to 2 mm.

The biggest and newest rod-type fiber features a 100 μm 19-cell core surrounded by a PCF cladding with two embedded boron-doped regions making the rod-type fiber polarization maintaining. The signal structure is surrounded by a 285 μm pump cladding with an NA of 0.6. The fiber has a mode field diameter of approximately 76 μm and a core NA on the order of 0.02 at 1064 nm. The birefringence induced by the boron regions is on the order of $1{\cdot}10^{-4}$. The very large effective area combined with extremely high pump absorption of up to 30 dB/m pushes the nonlinear threshold to very

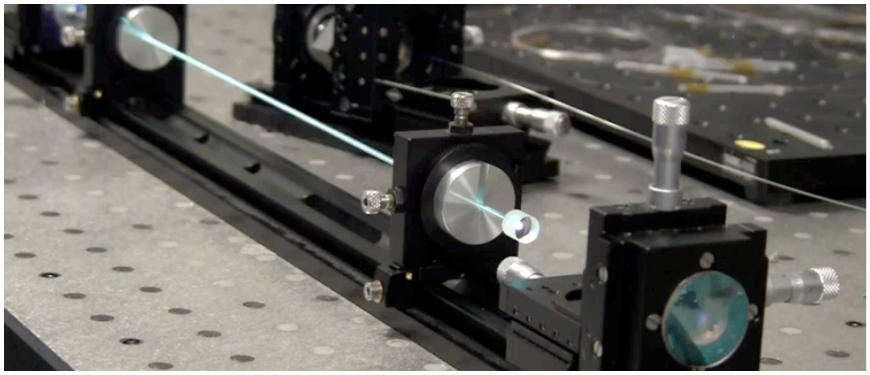

Figure 5.34: Image of the seed coupling section of the setup for characterizing rod-type fibers.

high levels and the rod-type fiber is therefore aimed at high peak-power pulsed amplifiers and has been shown to handle mega-Watt peak-power levels [11]. Additional results featuring rod-type fibers are found in [76–79].

The setup for characterizing the rod-type fiber is very similar to the setup for flexible large core fibers with a few exceptions. Due to the lower core NA of the rod-type fiber coupling of the seed light into the core becomes more difficult and extending the beam path distances in the setup is necessary to make the seed coupling easier. Furthermore, the saturation power scales with the area of the core, and due to the much larger core of the rod-type fiber 1 W of seed power is no longer enough and an additional pre-amplifier stage is necessary. Since the rod-type fiber is primarily used in the pulsed regime, a pulsed seed is preferred. Due to restrictions on the length of the fiber, 976 nm pumping is a prerequisite. A setup has been built for the rod-type fibers featuring a 1064 nm seed with 7 ps pulses, a repetition rate of 80 MHz and an average output power of $\sim$30 mW. In the near future the setup will feature a pre-amplifier, pushing the seed power to the necessary $\sim$10 W. An image of the seed coupling section of the setup is shown in figure 5.34. The rod in the image is $\sim$35 cm long and is equipped with endcaps, which are silica blocks, providing beam expansion to reduce end facet intensity and the risk of end facet damage, without compromising the high pump acceptance angle. Also, the beam expansion significantly improves the signal return loss even for a 0° angled facet. Figure 5.35 shows near field images of the output from the 100 μm core without amplification

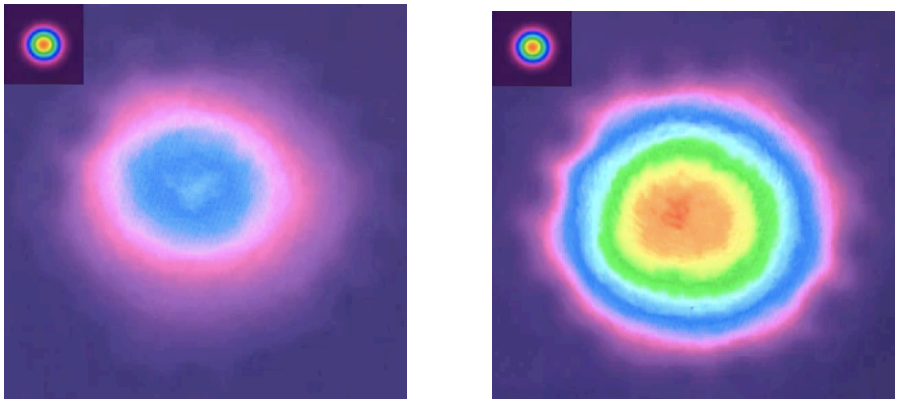

(a) (b)

Figure 5.35: Near field images of the output from the 100 μm core rod-type fiber (a) without amplification and (b) amplified to 15 W. The insert in the top left corner of both images is the output from a standard 10 μm core.

in figure 5.35(a) and amplified to 15 W in figure 5.35(b). The insert in the top left corner of both images is the output from a standard 10 μm core fiber for comparison.

5.4 Mode quality

The high beam quality is one of the virtues of a fiber laser and is often quantified through the M^2 value indicating the degree of multimode operation of the laser, where $M^2 = 1$ is pure Gaussian single-mode operation as defined in ISO standard 11146. The M^2 value is calculated from the measured beam diameter along the propagation direction. Although M^2 is a commonly used method for quantifying the degree of multimode operation in the fiber, the method does have disadvantages. The M^2 value can still be very low even when the higher-order mode content of a fiber becomes large. For example, if the fiber supports a superposition of the LP01 and LP11 modes, the M^2 value depends on the phase shift between the two modes and can still produce very low and misleading values [80]. The M^2 value has been measured for both the DC-200-40-PZ-Yb fiber and the DC-150-30-PM-Yb fiber using the Spiricon M2-200 beam propagation analyzer. For both fibers $M^2 \approx 1.15$ in both directions when the fibers are coiled at their operational diameter.

Spatially resolved spectral interferometry

Rather than using the M^2 measurement, single-modeness of a fiber is typically defined by the cut-off wavelength measured under the telecom standard TIA-455-80-C. The cut-off wavelength is the wavelength at which the higher order modes are suppressed by 19.3 dB and can be measured using a dual-coiling technique, where the differential loss between the two coils is 0.1 dB at the cut-off wavelength. The cut-off wavelength is per definition determined at a coil diameter of more than 28 cm, which for telecom purposes is far above the operational coil diameter. The second coil should be small enough to attenuate the second order mode – usually 8 cm. Thus, by definition a fiber which has more than 19.3 dB suppression of higher order modes when bent to 28 cm is single-mode.

The cut-off according to the standard is difficult to measure on the DC-200-40-PZ-Yb fiber, since the core does not guide at all at an 8 cm coil diameter – and even more so for rod-type fibers which cannot be coiled at all. An alternative is to quantify the degree of beam stability as the input beam launch is changed in the $x-$ and y-direction on a fiber of a typical device length, coiled to the operational diameter. This method was used in the characterization of the DC-200-40-PZ-Yb fiber and the DC-150-30-PM-Yb fiber, however, no official standards or definitions exists for this method.

S^2 imaging is the name of another beam quality measurement method based on resolving the image of the output of a fiber both spatially and spectrally. The basic idea of the measurement is to detect small amounts of higher-order modes that beat with the fundamental mode [28]. The main purpose of performing the S^2 imaging measurement is to quantify the exact degree of higher-order mode suppression in the fiber to ensure that a particular fiber is single-mode in practice.

An S^2 measurement has been performed on a 3 m long DC-200-40-PZ-Yb fiber coiled at a diameter of 50 cm – 3 m is the typical length of the fiber pumped with 976 nm light and 50 cm is far above the operational diameter. An illustration of the S^2 imaging setup is shown in figure 5.36. Light from a linearly polarized ASE source is launched into the slow axis of the test fiber and the output is imaged onto the end of a single-mode probe fiber, which is coupled into an OSA. The probe fiber is placed

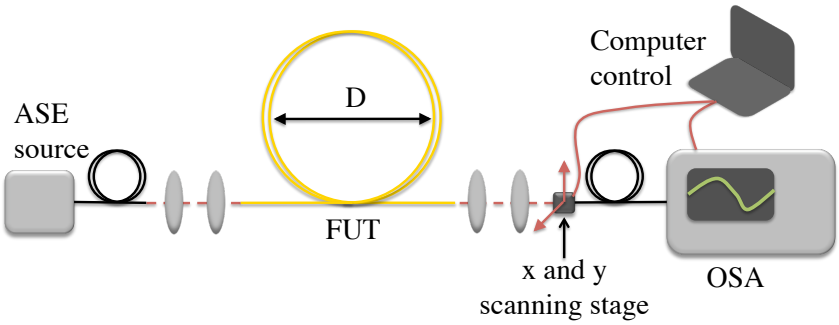

Figure 5.36: Illustration of the S^2 imaging setup.

on a translation stage, which moves the fiber in the x- and y-direction, perpendicular to the beam propagation direction, and at each (x, y)-point the optical spectrum is measured. 30×30 spectra are measured with a total acquisition time of approximately 30 minutes.

If two modes overlap spatially in the near field at a specific point, they will have an interference pattern in the optical spectrum due to the group delay difference between the modes. The interference pattern depends on the modal content and on the position (x, y) and is used to simultaneously image the different higher order modes in the fiber and to measure their relative suppression. The interference between the two modes result in a combined spectral intensity given by

$$I(x, y, \omega) = I_{FM}(x, y, \omega)[1 + \alpha^2(x, y) + 2\alpha(x, y)cos(\tau_b\omega)], \tag{5.3}$$

where I_{FM} is the intensity of the fundamental mode, ω is the angular frequency, τ_b is the period of the beat frequency between the two modes due to the group delay difference, and α is the amplitude of the higher-order mode relative to the fundamental mode. A Fourier transformation of the spectral intensity produces a DC peak with AC sidebands, where the amplitude, $f(x, y)$, of the AC sidebands relative to the DC peak is given by

$$f(x, y) = \frac{\alpha(x, y)}{1 + \alpha^2(x, y)}. \tag{5.4}$$

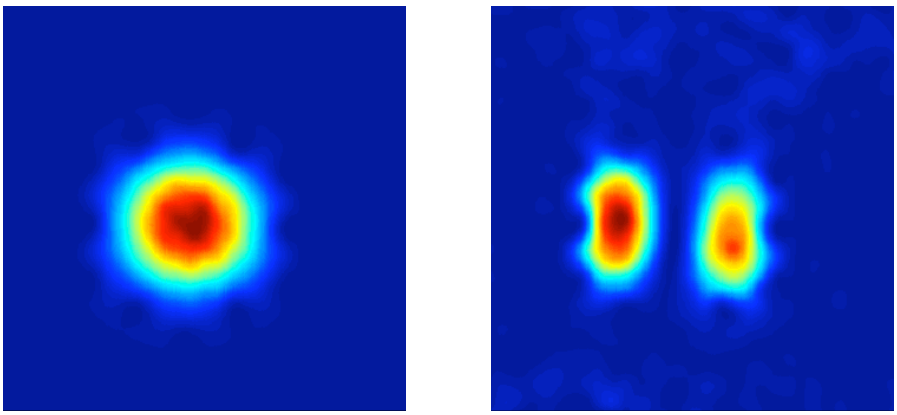

(a) (b)

Figure 5.37: Images of the two modes present in the DC-200-40-PZ-Yb fiber, (a) the fundamental LP01 mode and (b) the LP11 mode with amplified intensity. The LP11 mode is suppressed by 23 dB in this measurement.

The power of the higher-order mode relative to the fundamental mode is given by

$$\frac{P_{HOM}}{P_{FM}} = \frac{\int\int I_T(x,y)\alpha^2(x,y)/(1+\alpha^2(x,y))dxdy}{\int\int I_T(x,y)/(1+\alpha^2(x,y))dxdy}, \tag{5.5}$$

where $\alpha(x,y)$ is obtained from equation 5.4 and $f(x,y)$ is obtained from the Fourier spectrum. $I_T(x,y)$ is the total intensity integrated over the entire spectrum.

Beam profile images of the two modes present in the DC-200-40-PZ-Yb fiber is shown in figure 5.37. Figure 5.37(a) shows the fundamental LP01 mode and figure 5.37(b) shows the LP11 mode with amplified intensity. The images are obtained by integrating the measured spectrum at each point. The suppression is measured to ∼23 dB at a coil diameter of 50 cm. At a coil diameter of 28 cm the suppression is as high as 30 dB. S^2 measurements have been performed on a 70 μm core rod-type fiber in [81].

Chapter 6

Fibers with filters

Besides being used purely for amplification, photonic crystal fibers can also include filtering functions. Fibers that confine light by the photonic bandgap effect have the unique property that they only guide light in a specific wavelength region and for wavelengths outside of this region the attenuation can be hundreds of dB/m [3]. Figure 6.1 is an overview of the guidance and transmission properties of a PCF and a PBG fiber.

Combining the wavelength filtering effect of PBG confinement with a doped core and an airclad, the filtering effect can be used in many applications such as suppression of ASE in low signal systems and gain shaping for long-wavelength amplifiers. ASE filtering is important in amplifier chains, where ASE is otherwise amplified along with the signal. By introducing an ASE filter in the fiber, the gain in each stage will increase, thereby reducing the number of amplifier stages, and the cost and size of the full system. Gain shaping can for example be used for systems that operate at the long-wavelength tail of the ytterbium gain region. In the wavelength region 1150–1200 nm the gain is extremely low in ytterbium, and in a traditional amplifier the output would be dominated by the growth of ASE at around 1030 nm, resulting in parasitic lasing in this wavelength region rather than amplification in the long-wavelength region. By using a fiber with a built-in filter below the signal wavelength, one can shape the gain such that the gain peak coincides with the signal wavelength, leading to a reduction of ASE and parasitic lasing and thus more efficient amplification.

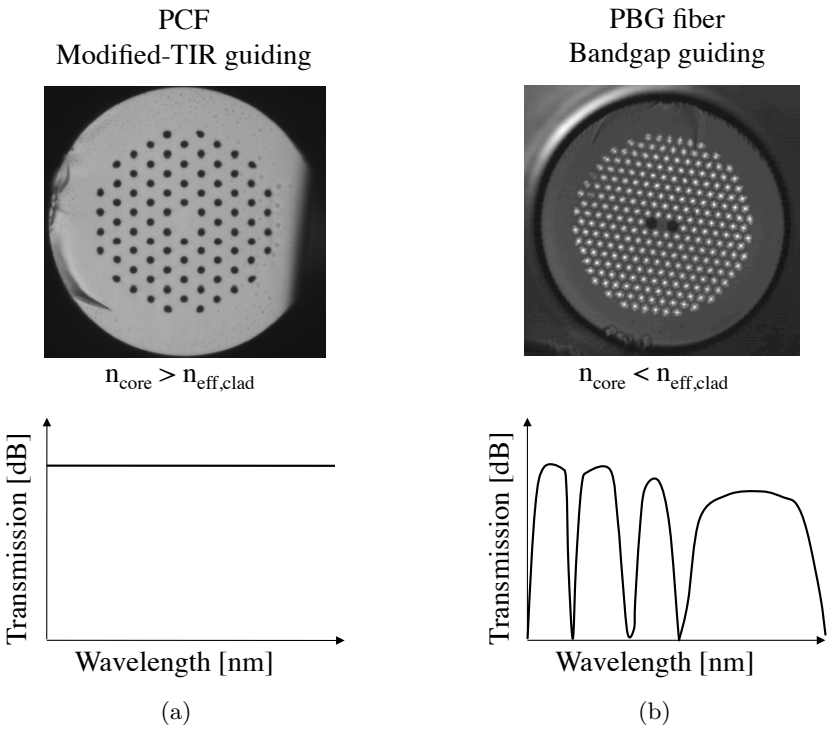

Figure 6.1: Overview of the guidance and transmission properties of (a) a PCF and (b) a PBG fiber.

Figure 6.2 shows an example of a PBG fiber where the bandgap is designed such that the region of high loss in the fiber coincides with the high gain region of ytterbium. The bandgap can also be placed in the short-wavelength region for 980 *nm* amplification or in the 1030–1080 *nm* region for suppression of long-wavelength Raman scattering.

In the first part of this chapter, the work with solid core PBG fibers for amplification in the 1100–1200 *nm* region will be presented. The work includes an experimental investigation of the design parameters at low power [82], the development of a high power 1178 *nm* amplifier with a record high output power of 167 *W* [12], an investigation of the parasitic lasing characteristics of the PBG fibers and frequency doubling of narrowband 1178 *nm* light to 589 *nm* [83].

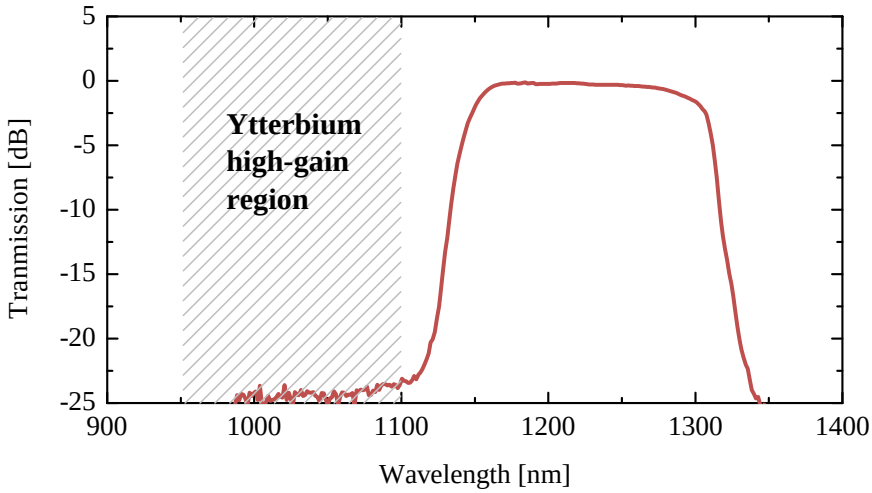

Figure 6.2: Transmission spectrum of a PBG fiber designed for long-wavelength amplification. The high loss region in the fiber coincides with the high gain region of ytterbium.

Distributed filtering in a PCF can also be achieved by placing resonant structures in a traditional PCF cladding and thereby selectively couple different modes and wavelengths out of the core [49]. In a traditional PBG fiber the core size is related by design to the operational wavelength and scaling of the core becomes difficult. With the resonant design one can design both the width and the center wavelength of the bandgap with an arbitrary core size. This type of fiber design is interesting for amplifiers where both filtering and large core sizes are needed, for example for long-wavelength narrow linewidth amplifiers, and this is a possible future design route for the 1178 nm amplifier.

In addition to distributed filtering in traditional PBG fibers or in PCFs with resonant couplers, filtering is also possible by infiltrating the airholes of a PCF with a high-index liquid material. The part of a fiber for which the airholes have been infiltrated, will guide light by the photonic bandgap effect as in a traditional PBG fiber, while the remaining part of the fiber will guide light by modified total internal reflection, thus a filter

is introduced in only a part of fiber. Among high-index liquid materials, liquid crystals exhibit a high degree of electrical and thermal tunability and can therefore be used to tune the bandgap properties of the fiber. In the second part of this chapter, a tunable fiber laser is demonstrated by infiltrating a passive large mode area fiber with liquid crystals and placing the fiber inside a fiber laser cavity [84]. The presence of a bandgap in the laser cavity will inhibit lasing at certain wavelengths, and by applying an electric field to the liquid crystal infiltrated part of the fiber, the bandgap position can be shifted, resulting in laser tunability.

6.1 Solid core photonic bandgap fiber amplifier

Lasers and amplifiers operating in the 1100–1200 nm wavelength region have been extensively developed, typically using bulk solid-state laser technology. Frequency doubling of these wavelengths produces yellow-orange light from 570 to 600 nm – a region useful for various medical applications, high-resolution spectroscopy, and laser-guide-star facilities [16]. Ytterbium-doped fibers in general have a very broad fluorescence spectrum extending up to 1200 nm and have been thoroughly investigated for long-wavelength lasers and amplifiers [45, 85–89]. The small-signal gain per unit length can be as high as 0.8 dB/m and hence the net gain can easily exceed 10 dB at 1178 nm [90]. This is an important wavelength to access 589 nm laser-guide-star sources by frequency doubling. However, the large gain between 1030 and 1100 nm creates very strong ASE and can lead to parasitic lasing. Parasitic lasing will limit the available gain at 1178 nm and thereby the power scalability. In order to overcome the problem of parasitic lasing we propose an ytterbium-doped PBG fiber amplifier in which an ytterbium-doped core is combined with the wavelength-filtering effect of PBG confinement. Efficient suppression of ASE at the conventional ytterbium gain wavelengths between 1030 and 1100 nm and a reduction in parasitic lasing outside the bandgap can be obtained. PBG fibers have previously been investigated for gain shaping at both short [91] and long [82, 92] wavelengths as well as for lasers [93–95].

Properties of the photonic bandgap fiber

Initially five solid core PBG fibers where fabricated with cladding pitches of 9.45 μm, 9.6 μm, 9.8 μm, 9.9 μm, and 10.1 μm. The fibers are

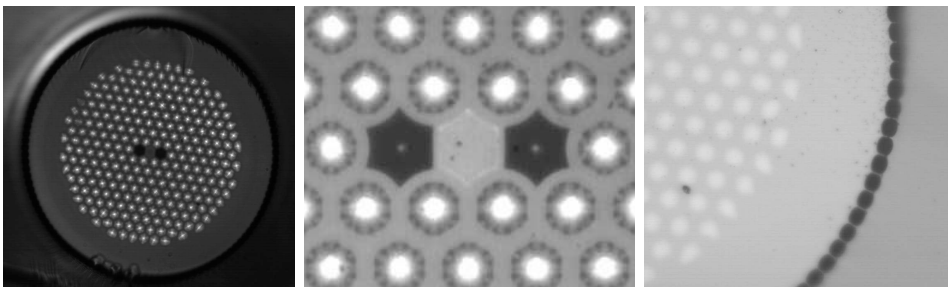

(a) (b) (c)

Figure 6.3: (a) Microscope image of the pump-cladding structure where the lighter regions are the high-index germanium-doped rods, while the two darker regions are the boron-doped rods. (b) Microscope image of the core region. (c) Microscope image of the airclad surrounding the pump-cladding structure.

named PBG-2008-9.45, PBG-2008-9.6, PBG-2008-9.8, PBG-2008-9.9, and PBG-2008-10.1, respectively. The signal cores consist of an ytterbium-doped rod, which is index-matched to the silica background and the core is surrounded by a PBG cladding structure composed of eight rings of high-index germanium-doped rods. The germanium-doped rods have a parabolic index profile with a +2.3% peak index contrast. For the fibers we measure the diameter of the cladding to between 214 μm and 225 μm, scaling with the cladding pitch.

The fibers all have a pump absorption of 1.1 dB/m at 976 nm. Furthermore, the PBG pump cladding is surrounded by an airclad structure, providing the pump guide with a large NA of 0.57 and allowing for efficient high power cladding-pumping [37, 96]. The polarization-maintaining properties of the fiber are obtained by incorporating two low-index boron-doped rods on either side of the core. The refractive index step of the rods relative to pure silica is -0.006. The boron-doped rods act as stress applying parts, inducing high birefringence in the fiber, while the low index results in confinement by total internal reflection in one direction and bandgap guiding in the other direction. The birefringence is on the order of 10^{-4}. A passive version of this type of hybrid TIR/bandgap fiber has been reported in [97]. Microscope images of the fiber structure, the core region and the airclad structure surrounding the pump cladding are shown in figure 6.3. The lighter regions are the germanium-doped rods, while the two darker

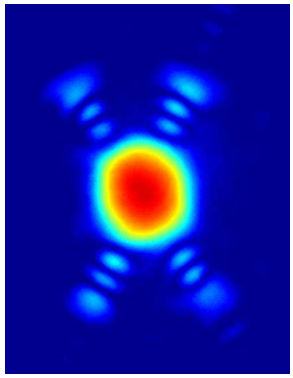

Figure 6.4: Near field image taken in the third order bandgap using 1150 nm light, where the stress rods are in the horizontal direction. An anti-resonant tail of light is visible in the surrounding high-index germanium-doped rods, but not in the boron-doped stress rods.

regions near the core are the boron-doped rods.

Core properties of the fiber design have been determined by performing measurements on a fiber which is identical to the fibers in questions in terms of cladding structure and core properties, but without the surrounding airclad. A near field measurement at 1150 nm of PBG-2008-10.1 yield at $1/e^2$ mode field diameter of 10.0 μm in the axis parallel to the stress rods, a mode field diameter of 10.8 μm and an NA of 0.1. A near field image taken in the third order bandgap using 1150 nm light is shown in figure 6.4, where the stress rods are aligned in the horizontal direction. An anti-resonant tail of light is visible in the four surrounding high-index germanium-doped rods, with the number of reflections in each tail – in this case three – indicating the bandgap order. The lack of an anti-resonant tail of light in the boron-doped stress rods on either side of the core is evidence of index-guiding in the direction of the stress rods and bandgap guidance in the other direction.

The photonic density of states have been calculated for the solid PBG fiber and is shown in figure 6.5 as a function of wavelength for a PBG fiber with a pitch of 10.1 μm. In the calculations the cladding is assumed to be infinite and periodic. The lighter the colour the more modes are guided, while black corresponds to regions with no allowed cladding modes – these regions are the photonic bandgaps.

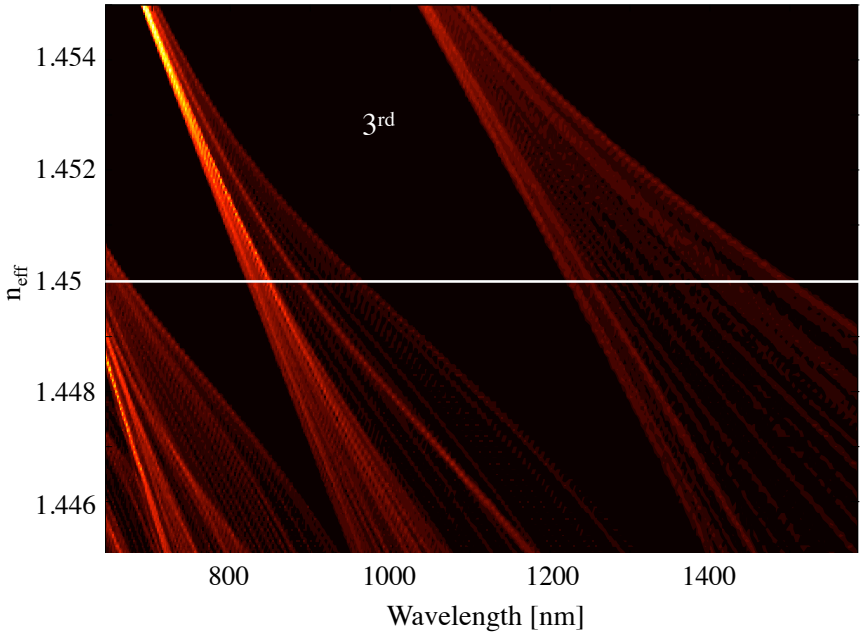

Figure 6.5: The photonic density of states calculated as a function of wavelength for a PBG fiber with a pitch of 10.1 μm. The lighter regions corresponds to guided modes, while black corresponds to regions with no allowed cladding modes.

Bandgap, loss and polarization properties

The transmission spectra of the fibers are measured using the setup in figure 6.6. In order to only transmit light in the core, light from a white light source is launched into 1 m of single-mode fiber with a core size of 10 μm, which is then butt-coupled to the 10 μm core of the solid core PBG fiber. The light from the core of the PBG fiber is subsequently collected by a high NA 10 μm core fiber in order to limit light collected by the optical spectrum analyzer to the core region. The bandgap transmission spectrum of 1 m of PBG-2008-9.9 is shown in figure 6.7, where the reduced transmission in the fourth order bandgap is due to ytterbium absorption. The transmission spectra in the third bandgap for the five fibers are shown in figure 6.8. It is evident from the measured spectra that the bandgap both widens and moves towards longer wavelengths as the pitch is increased.

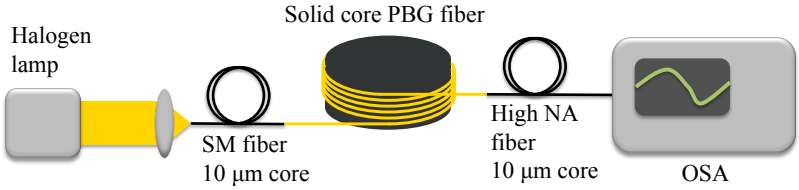

Figure 6.6: Illustration of setup for measuring the bandgap transmission spectrum. A similar setup is used for measuring the core loss.

Since the emission cross section of an ytterbium-doped fiber is significantly lower in the wavelength range 1100–1200 nm than at the conventional ytterbium gain region around 1030 nm, very low core losses in the bandgap are required in order to obtain efficient operation at longer wavelengths. The core loss is measured using a setup similar to the one in figure 6.6. Transmission spectra are recorded using an OSA for 99 m and 1 m of a PBG fiber, while keeping the butt-coupling between the singe-mode fiber and the PBG fiber constant. The two measurements were subtracted to infer the losses, which are shown in figure 6.9. The losses are 0.01–0.02 dB/m in the wavelength range 1150–1200 nm, which lies within the third order bandgap of the structure.

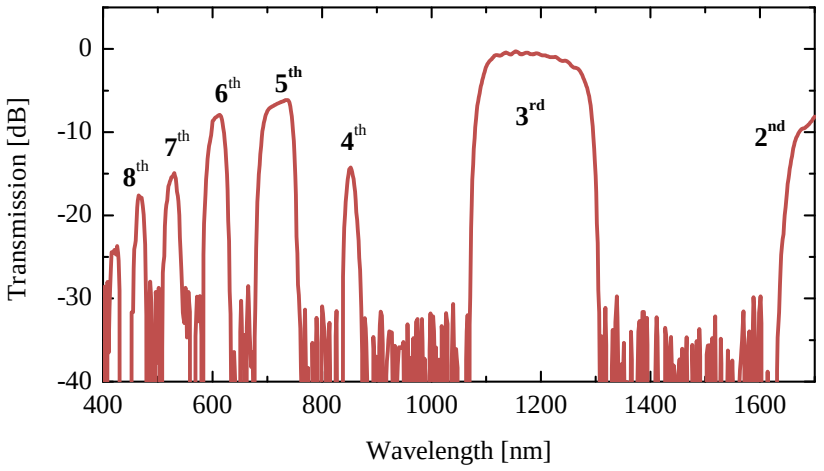

Figure 6.7: Bandgap transmission spectrum of 1 m of PBG-2008-9.9. The dip in the fourth order bandgap is due to ytterbium absorption.

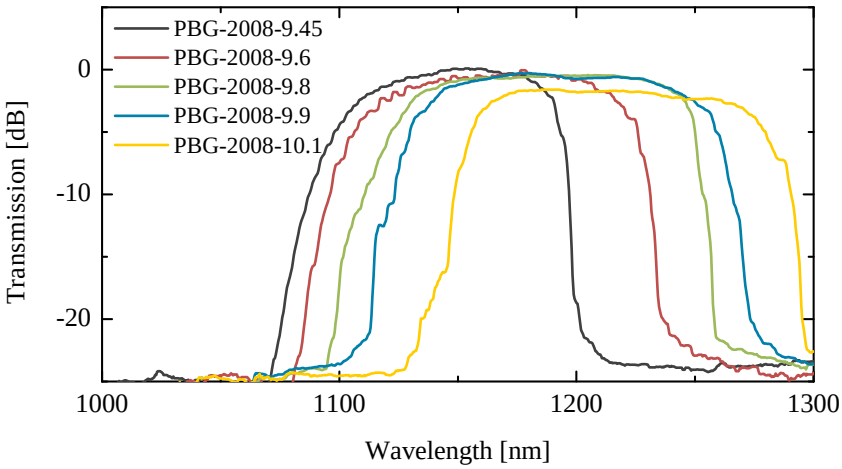

Figure 6.8: Bandgap transmission spectra in the third order bandgap for all five PBG fibers.

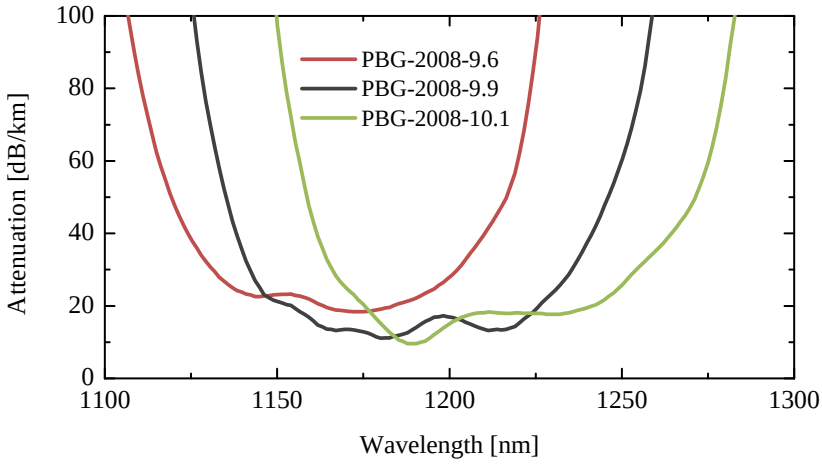

Figure 6.9: Loss spectrum of three PBG fibers obtained by subtracting transmission spectra for 99 m long fibers from transmission spectra of 1 m long fibers.

Low power amplification and laser properties

The amplification properties of the fibers are measured using the forward seeded amplification setup depicted in figure 6.10. The PBG fiber is pumped with up to 3 W of 976 nm light and seeded with 2 mW of 1080–1145 nm light from a laser cavity created from 30 m of the same PBG fiber and a laser dispersing prism. The seed laser cavity is tuned using a mirror. Furthermore, the pump light is launched at an angle in order to reduce guidance in the high-index rods and to obtain maximum pump absorption. Due to the higher index of the germanium, roughly 12% of the pump light is expected to be trapped in the rods with a straight pump coupling scheme.

The amplification results for two of the PBG fibers are presented in figure 6.11. For both fibers results show that the amplification at a given wavelength scales with the ASE power. For the specified pump power an amplification of up to 15 dB is obtained in both fibers. Peak

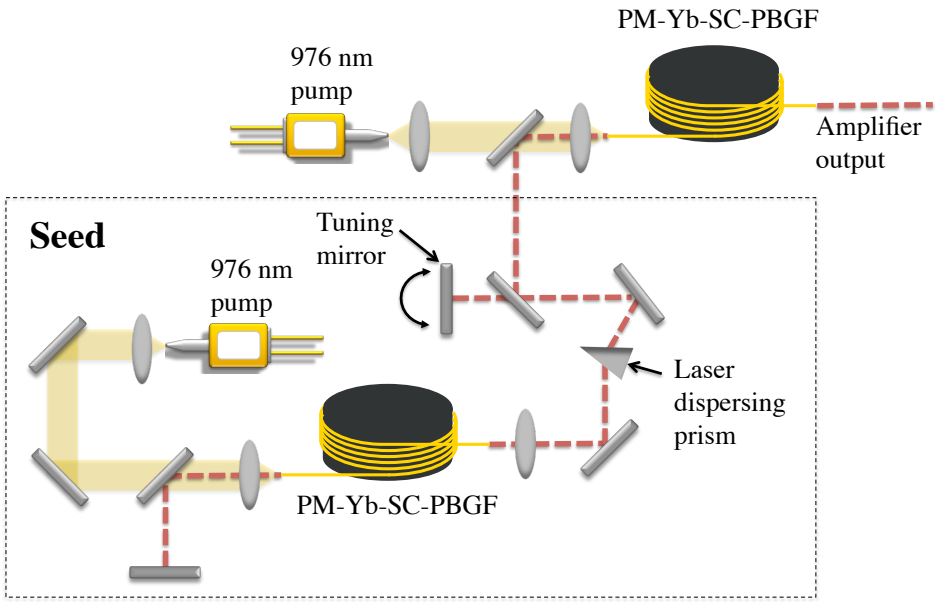

Figure 6.10: Illustration of the low power amplifier setup where the tunable seed laser is made from a cavity containing the same PBG fiber and a laser dispersing prism.

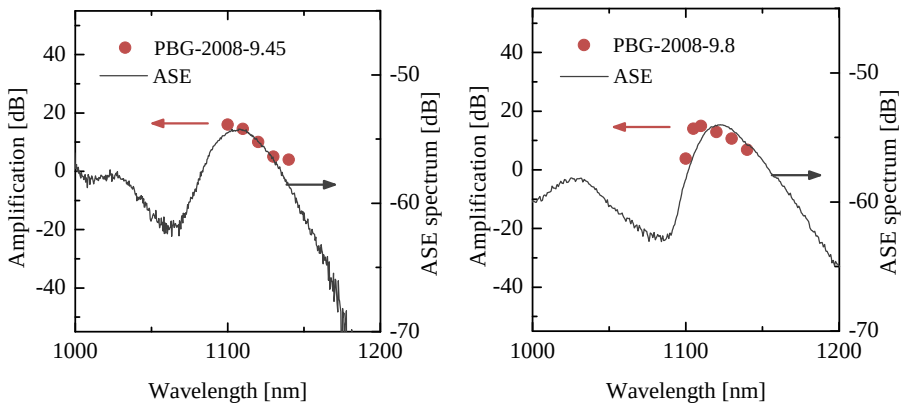

(a) (b)

Figure 6.11: Amplification (left axis) as function of seed wavelength at constant seed and pump power for (a) PBG-2008-9.45 and (b) PBG-2008-9.8. For both fibers results show that the amplification at a given wavelength scales with the ASE power (right axis).

amplification occurs at the wavelength that experiences the least loss due to the bandgap combined with the highest gain due the emission cross section. Increasing the pump power will shift the ASE peak, and hence also the peak amplification, towards the left bandgap edge.

Figure 6.12 shows the output spectrum from PBG-2008-9.8 in laser configuration, i.e. the seed part of the setup in figure 6.10. 60 dB of ASE suppression is apparent in the output spectrum outside the bandgap and the fiber is lasing at the edge of the bandgap. Furthermore, experiments were performed with the fibers in a backward pumped laser configuration without the laser dispersing prism in order to investigate the dependence of the natural lasing wavelength on the pitch. The power is kept close to the lasing threshold level and the resulting output spectra for four of the fibers are shown in figure 6.13. Figure 6.14 shows the scaling of the natural lasing wavelength with the pitch.

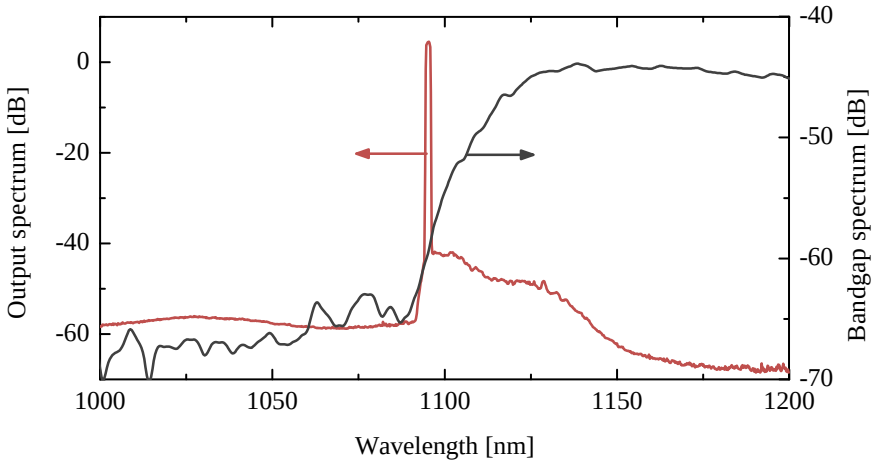

Figure 6.12: Output spectrum from PBG-2008-9.8 in laser configuration. The fiber is lasing at the edge of the bandgap and 60 dB ASE suppression is apparent in the output spectrum.

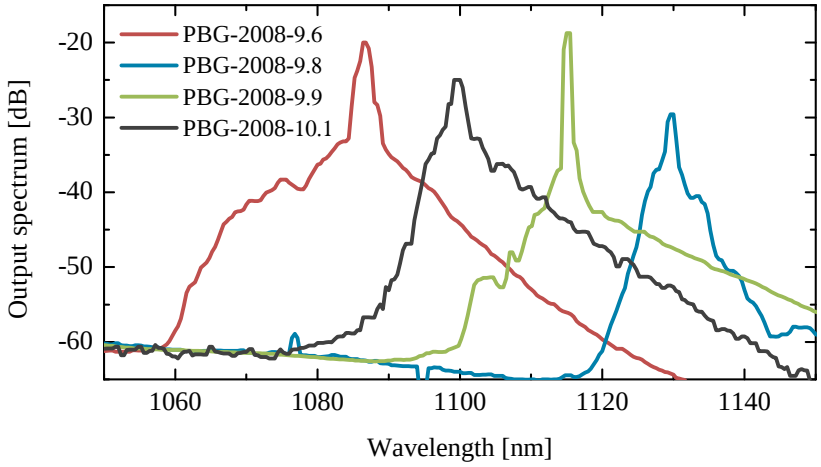

Figure 6.13: Output spectra from four of the PBG fibers to reveal the natural lasing wavelength.

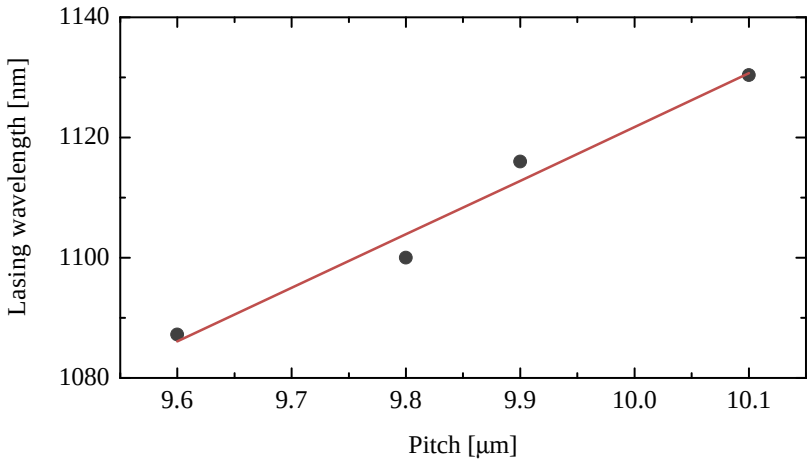

Figure 6.14: Lasing wavelength as a function of pitch for the four PBG fibers.

Engineering the gain profile for 1178 nm amplification

Based on the conclusions from the investigation at low power, three new fibers were fabricated with pitches of 10.1 μm, 10.2 μm, 10.3 μm for 1178 nm amplification. The fibers are named PBG-2009-10.1, PBG-2009-10.2, and PBG-2009-10.3, respectively. Loss measurement of the three fibers where used to determine which fiber is the most suitable for amplification at 1178 nm, keeping in mind that peak amplification occurs close to the short-wavelength bandgap edge. Loss measurements of the three fibers are shown in figure 6.15. In the measurements all fibers are kept at a bend diameter of 32 cm. In the case of 1178 nm amplification, PBG-2009-10.1 is optimum, because it has the lowest loss at this wavelength. The other two fibers will be suitable for amplification at even longer wavelengths.

The optimum length of the fiber is calculated using the model presented in section 3.3. Due to the fact that the emission cross section is extremely low at 1178 nm, the commonly used estimate of the optimum fiber length based on the pump absorption coefficient alone cannot be used. Calculations are done for PBG-2009-10.1 and are based on an ytterbium concentration of $0.38{\cdot}10^{26}$ m^{-3}, an upper state life time of 0.84 ms, the absorption and emission data presented in section 3.1, the

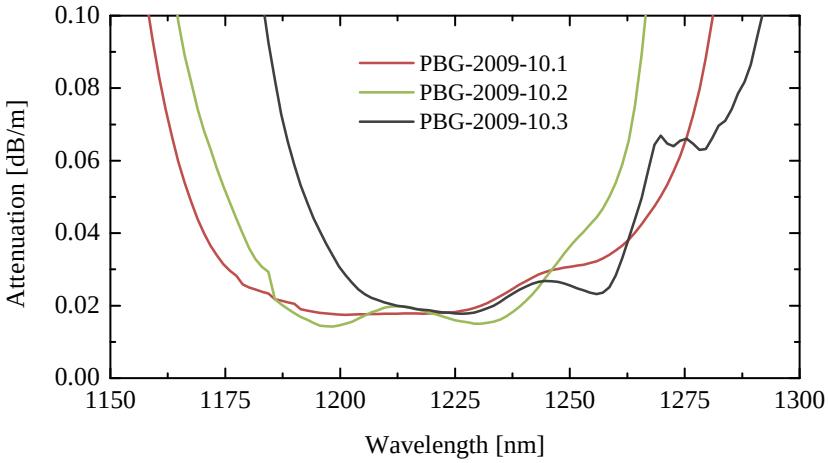

Figure 6.15: Loss spectrum of three fibers obtained by subtracting transmission spectra for 99 m long fibers from transmission spectra of 1 m long fibers.

design data from this section, the loss value from figure 6.15, 2.5 W of coupled seed power and 220 W of coupled pump power. The calculation is shown in figure 6.16 where the optimum fiber length is found to be $\sim$40 m.

As previously mentioned, in active PBG fibers the gain peak is moved inside the bandgap to the wavelength where the combination of material gain and bandgap loss gives the highest gain value. The effect of the photonic bandgap on the gain profile of an ytterbium-doped fiber is illustrated in figure 6.17. The calculated net small-signal gain of a 40 m long fiber coiled to 26 cm and pumped with 275 W of 976 nm light is plotted both with and without distributed spectral filtering incorporated. The fiber parameters for the two fibers are identical except for the absence of a bandgap for the black curve. The small signal gain is $\sim$22 dB at 1178 nm for the PBG fiber at this power level.

Based on general theories of energy extraction in gain media, the ratio of small signal gain to loss should be greater than 10 to achieve at least a 50% extraction efficiency; hence, for high-efficiency operation, the loss in the bandgap is required to be much lower than 0.1 dB/m. Thus, creating

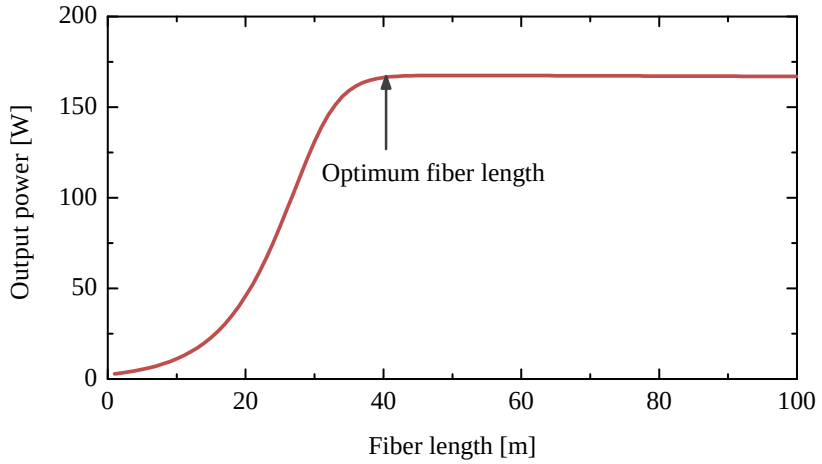

Figure 6.16: Output power as a function of fiber length for PBG-2009-10.1. The optimum fiber length is found to be $\sim$40 m.

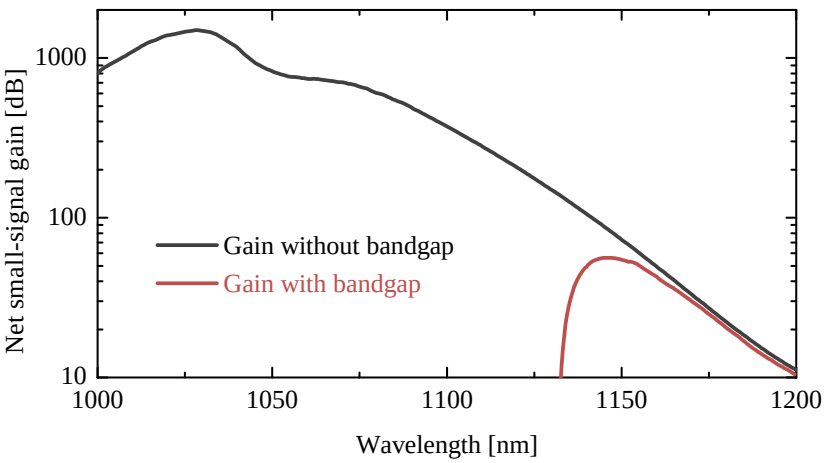

Figure 6.17: Net small-signal gain of a 40 m long ytterbium-doped fiber coiled to a diameter of 26 cm with 275 W of pump power. The black curve is the gain without distributed filtering, while the red curve is the gain with distributed filtering arising from the photonic bandgap effect.

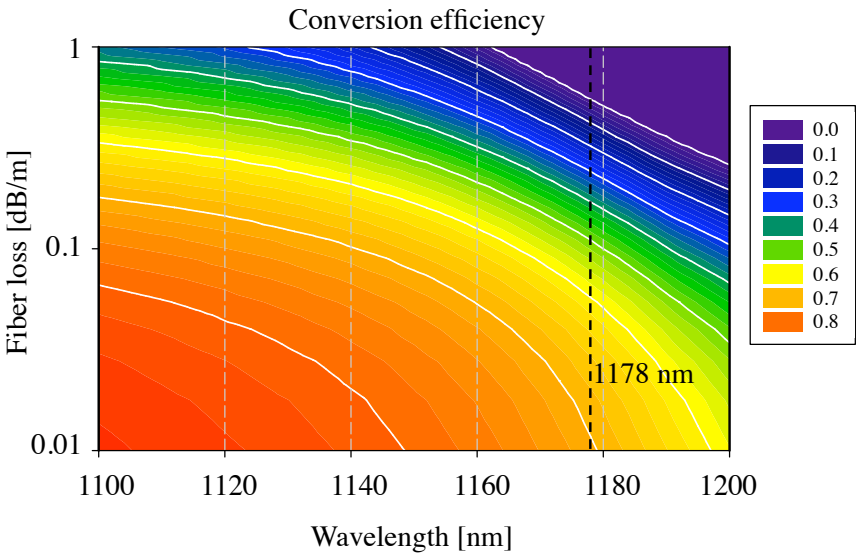

Figure 6.18: Conversion efficiency (isolines) are plotted as a function of fiber loss and wavelength. With losses below 0.1 dB/m, an efficiency of 50% can be obtained at 1178 nm, while an efficiency of 68% can be obtained with losses below 0.02 dB/m.

a highly efficient PBG fiber amplifier in the region 1150 to 1200 nm is a great challenge. The calculated conversion efficiency is plotted as function of fiber loss and wavelength in figure 6.18. With losses below 0.1 dB/m, an efficiency of 50% can be obtained at 1178 nm, while an efficiency of 68% can be obtained with losses below 0.02 dB/m.

To avoid parasitic lasing as the pump power is increased it is essential to operate the amplifier close to the wavelength of peak amplification and to ensure that the loss slope of the bandgap edge is sharp enough to cancel the steep gain slope. Figure 6.19 illustrates how the gain slope grows as the pump power is increased at long wavelengths. Thus, both the position and the steepness of the short-wavelength edge of the bandgap relative to the signal gain are crucial to the efficiency of the amplifier. In the design investigation we found that the position of the bandgap and thereby the position of peak amplification, can be shifted towards longer or shorter wavelengths by rescaling the dimensions of the fiber. Smearing of the loss slope at the bandgap edge can be caused by pitch variations along

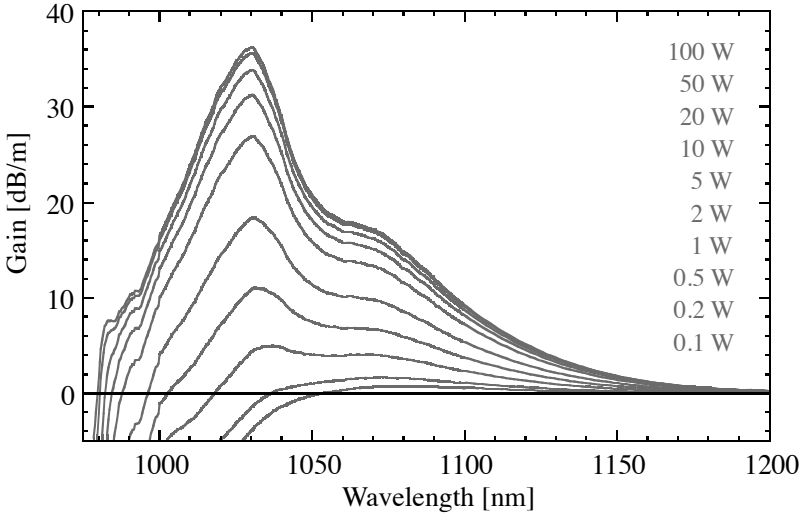

Figure 6.19: Gain as a function of wavelength as the pump power is increased. The gain slope becomes steeper at long wavelengths.

the fiber length and will impact the filtering properties significantly. From figure 6.8 we find that a 0.1 μm change in pitch can lead to a change in the position of the bandgap edge of around 10 nm. Therefore, pitch variations should be kept at a minimum. The uniformity of the fiber is an engineering challenge (yield and stability of the drawing tower and furnace conditions).

The gain of an ytterbium-doped fiber increases fast as the wavelength is decreased and in order to obtain high-efficiency power extraction at 1178 nm the loss slope needs to be steeper than the gain slope at wavelengths shorter than 1178 nm combined with ultra-low loss at 1178 nm [90]. Thus, power scaling of an ytterbium-doped PBG fiber amplifier at long wavelengths is challenging. Two PBG fibers with a pitch of 10.1 μm have been fabricated – PBG-2008-10.1 and PBG-2009-10.1. The first fiber from 2008 was presented in section 6.1 and [90, 98], while the second fiber from 2009 was introduced in the present section. Compared to PBG-2008-10.1, PBG-2009-10.1 has a steeper bandgap edge due to improved uniformity, achieved by screening and selecting a fiber section with reduced pitch variations along the fiber length. The improvements contribute to a far more efficient suppression of ASE and parasitic lasing. The short-wavelength bandgap edge of the improved fiber is compared to that of the older fiber in figure 6.20. With

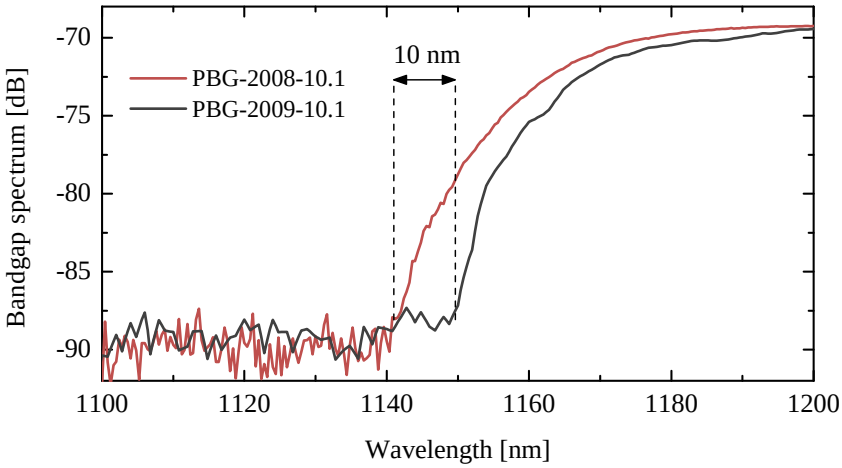

Figure 6.20: Comparison of the bandgap transmission spectra between the old and the new PBG fiber. The newer fiber is fabricated with a slight change in bandgap position and with a steeper short-wavelength bandgap edge. The length of the old PBG fiber is 36 m, while the new PBG fiber is 40 m.

nearly the same loss value at 1178 nm and a difference of almost 10 nm in the position of the short-wavelength edge the newer fiber is more efficient at suppressing ASE and parasitic lasing.

Coiling the fiber also has a substantial effect on the bandgap. The effect of coiling the fiber can be understood by treating the fiber as a straight fiber with a tilted refractive index as in [99–101]. When the fiber is coiled, core modes at the short-wavelength edge of the bandgap are resonant with radiation modes on the outside of the coil, while core modes at the long-wavelength edge are resonant with radiation modes on the inside of the coil. As a consequence the bandgap narrows. Figure 6.21 shows the transmission spectra of a 1.5 m piece of PBG-2009-10.1 at different coil diameters. This is a characteristic property of PBG fibers and can be used to fine-tune the position of the bandgap. In addition, a steeper loss slope can be achieved by coiling. In figure 6.22 the average loss of the PBG fiber is compared to the average saturated gain with 275 W of pump power and 5 W of seed power for an ytterbium-doped fiber without an incorporated PBG structure. The loss slope of the fiber is not steep enough to cancel the

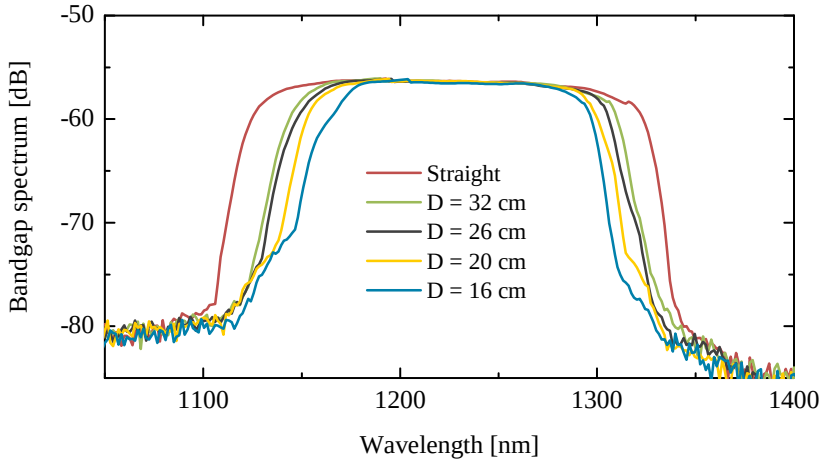

Figure 6.21: Transmission spectra of a 1.5 m long piece of PBG-2009-10.1 at different coil diameters. Coiling can be used for fine-tuning the position of the short-wavelength bandgap edge.

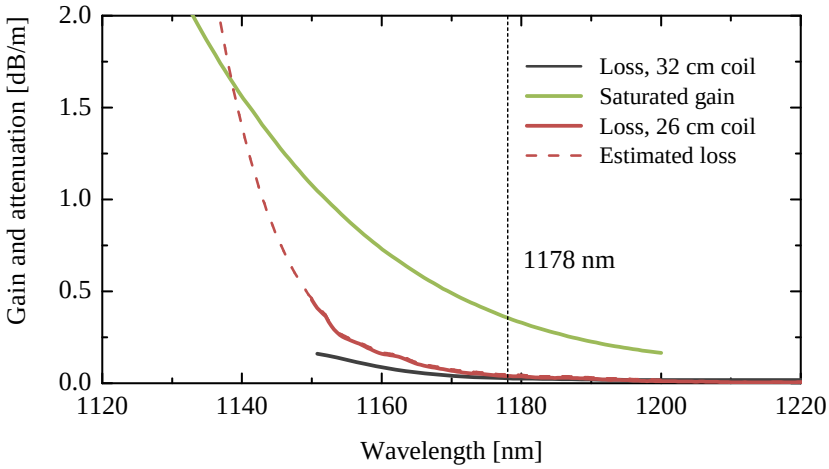

Figure 6.22: Average loss curve of 40 m PBG-2009-10.1 coiled to a diameter of 32 cm (black) and 26 cm (red) compared to the average saturated gain with no bandgap, 275 W of pump power and 5 W of seed power (green). The dashed red curve is an estimated loss slope. Only after coiling the fiber to a diameter of 26 cm the loss slope is steep enough to cancel the gain slope.

gain slope at a coil diameter of 32 *cm*, thus eventually parasitic lasing will occur. With a tighter coil at a diameter of 26 *cm* the loss slope is estimated to be steeper than the gain slope and will therefore more efficiently suppress parasitic lasing.

Amplifier setup

To determine whether forward or backward pumping is optimum for the amplifier, the model from section 3.3 is used to calculate the inversion and output power of the fiber. This has been done in figures 6.23(a) and 6.23(b) in forward and backward pumped configuration, respectively. While the output power (red curve) is the same in forward and backward pumped configuration, the inversion in the fiber differs significantly. When the fiber is forward pumped the inversion is almost 0.5 in the input end and almost zero in the output end. Hence, in a forward pumped configuration, the input part of the fiber could suffer from severe photo darkening due the high inversion. In backward pumped configuration the inversion is approximately 0.35 in the pump input (and seed output) end and 0.2 in the seed input end. While the inversion is still high compared to 1064 *nm* amplifiers, it is significantly lower and more evenly distributed in the backward pumped configuration compared to the forward pumped configuration. Thus, from a reliability point of view, the backward pumped configuration is preferred for long-wavelength amplification where the emission cross section is low.

The amplifier setup is illustrated in figure 6.24. In the experiment, the fiber was coiled to a diameter of 26 cm, and both fiber ends were sealed and angle polished by 10°, resulting in a reflection suppression on the order of 40 *dB*. An unpolarized fiber Raman laser (FRL) at 1178 *nm* was used as seed source. The amplifier was seeded with ∼5 *W*, well above the saturation power level in order to ensure gain saturation. The amplifier was backward-pumped using a 976 *nm* laser diode (LD, Laserline LDM200-350). At the seed input end two dichroic mirrors (HR $>$ 1150 *nm* and HT $<$ 1100 *nm*) are used for seed laser protection and at the signal output end a dichroic mirror (HR at 1000-1300 *nm* and HT at 976 *nm*) is used to filter out pump light in the output spectrum. The seed coupling efficiency is 50% in free space configuration, and the pump coupling efficiency is 71% due to cladding modes in the output fiber from the laser diode (∼20%) and Fresnel reflection at the fiber input end.

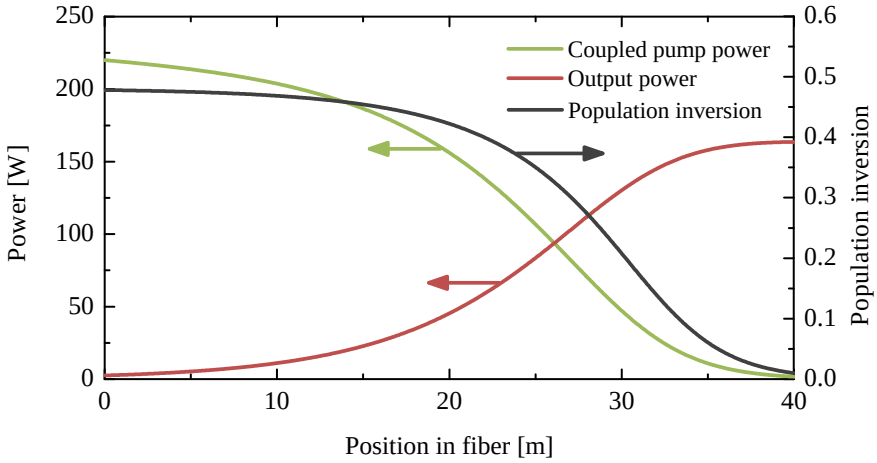

(a)

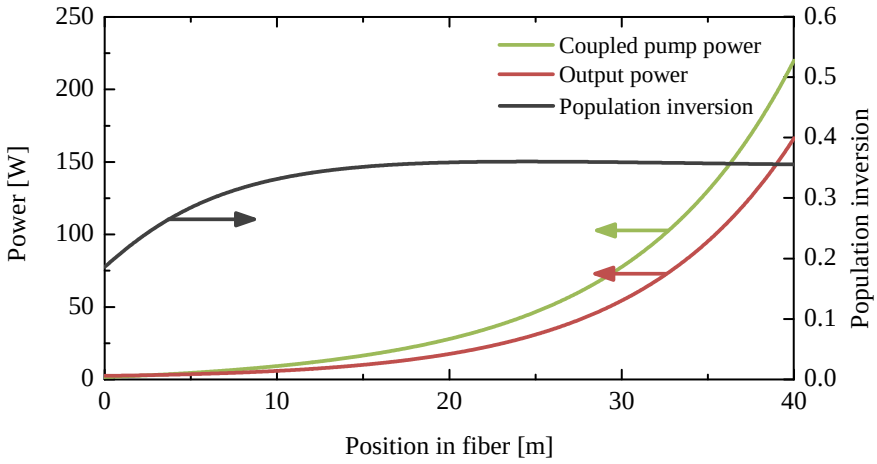

(b)

Figure 6.23: Calculated inversion and power levels as a function of position in the fiber in the case of (a) forward pumping and (b) backward pumping. Based on the lower inversion, backward pumping is preferred for 1178 *nm* amplification.

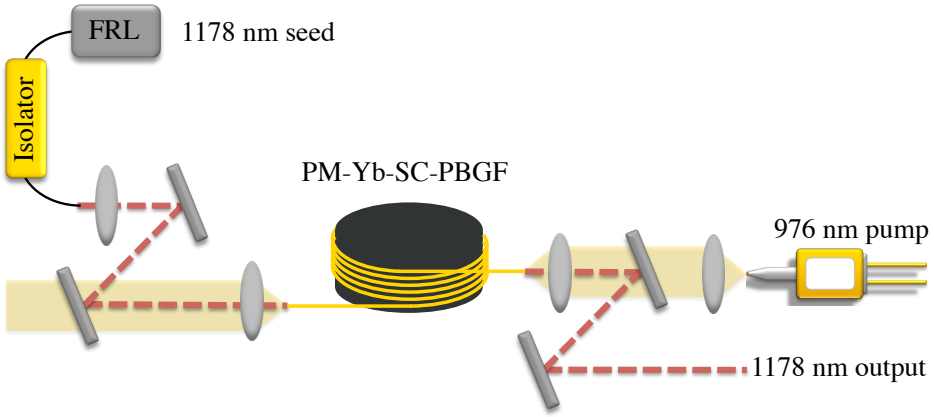

Figure 6.24: Ytterbium-doped solid core photonic bandgap fiber amplifier, seeded by an 1178 nm fiber Raman laser, and backward-pumped by a 976 nm laser diode.

High power amplification at 1178 nm

From the PBG fiber amplifier we obtained an output power of 167 W with a pump power of 275 W – a record output power for an ytterbium-doped fiber amplifier in this wavelength region as well as for PBG fiber amplifiers. The maximum output power of the amplifier was limited by the available pump power. Output power as a function of launched pump power is shown in figure 6.25. The index of the germanium rods in the cladding is higher than the surrounding silica background and as a consequence a fraction of pump light will be trapped in the germanium rods and cannot be used for exciting the ytterbium ions in the core as it passes through the fiber. The slope efficiency was measured to 61%, however considering the fraction of trapped pump light, the actual slope efficiency is as high as 69%. This value is close to the calcuated value of 68% conversion efficiency. The NA of the germanium rods is 0.29 and therefore trapping of pump light can only be reduced by avoiding pump light NAs below 0.29, for example by angled pump coupling or by using special combiners.

in figure 6.26 the output spectrum from the amplifier shows pump power limited on/off amplification of up to 16 dB. Considering amplification of coupled seed power rather than transmitted seed power, the actual gain in the amplifier is 15 dB. The linewidth before and after amplification is 1.3

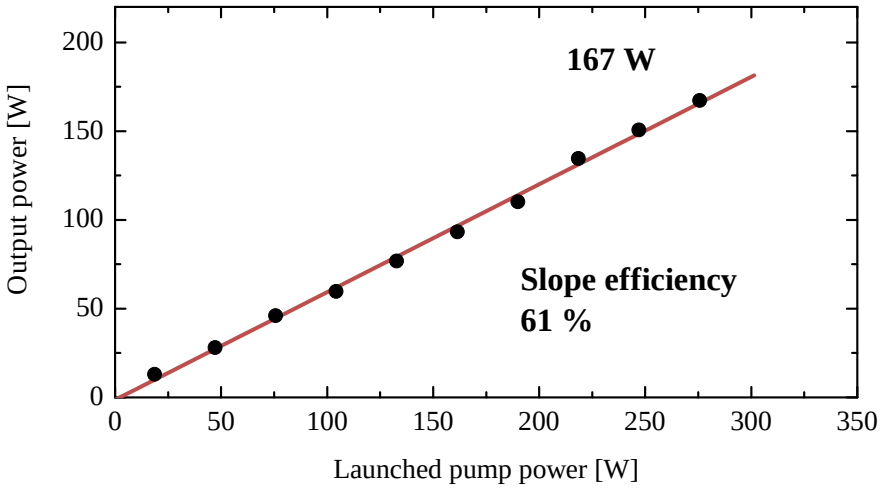

Figure 6.25: Output power at 1178 nm as a function of launched pump power. The measurement was limited by available pump power, and the output spectrum showed no sign of ASE, thus the power is scalable.

nm. A nearly complete absence of ASE in the output spectrum suggests that further power scaling can be expected. The fiber is expected to reach the parasitic lasing limit at around 17 dB, limiting the current system to ∼250 W with 5 W of seed power. However, further power scaling can be achieved e.g. by including an additional amplifier stage. An M^2 measurement has been performed with an output power of 100 W and yields a value of ∼1.1, indicating that the amplifier produces single-mode output. Figure 6.27 shows the near field image at 100 W. The mode field diameter is ∼10.3 μm.

Amplification experiments with the remaining fibers resulted in very high power as well, however, all limited by parasitic lasing. PBG-2008-10.1 reached an output power of 90.5 W and a slope efficiency of 47% with a coil diameter of 26 cm, PBG-2009-10.2 reached an output power of 132 W and a slope efficiency of 58% with a coil diameter of 32 cm, and PBG-2009-10.3 reached an output power of 61.5 W and a slope efficiency of 32% with a coil diameter of 32 cm. The output power as a function of launched pump power is shown in figure 6.28 for all three fibers. Again, the slope efficiencies

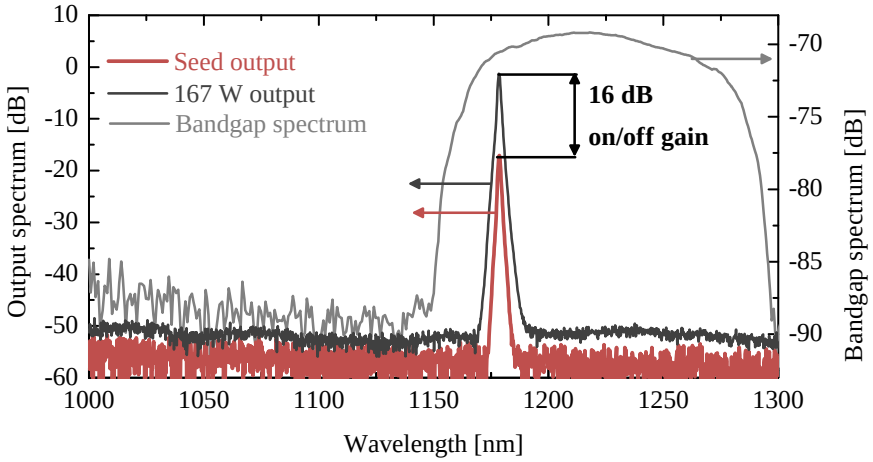

Figure 6.26: Amplifier output spectra of the seed (red) and the 167 W output (black). The bandgap position and shape (grey) is crucial to the efficiency of the amplifier. The linewidth before and after amplification is 1.3 nm.

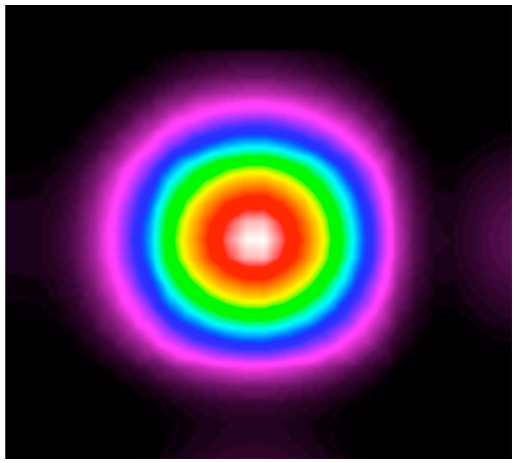

Figure 6.27: Near field image at an output power of 100 W. The output has an M^2 value of ∼1.1 and a mode field diameter of ∼10.3 μm.

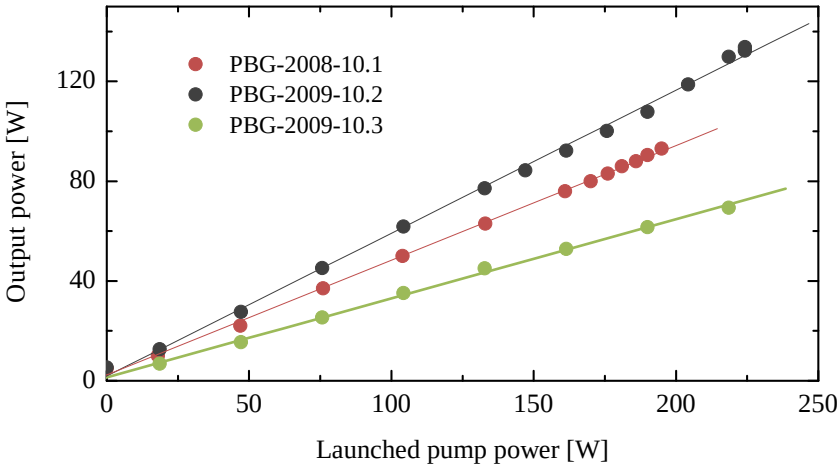

Figure 6.28: Output power as a function of launched pump power for the fibers PBG-2008-10.1, PBG-2009-10.2, and PBG-2009-10.3. The slope efficiencies are in fact higher if pump light trapped in the germanium rods is considered. The maximum power is limited by parasitic lasing in all three fibers.

should be corrected for pump light trapped in the germanium rods and they are in fact higher than the stated values. Results with these three fibers indicate that even though scalability to very high power depends strongly on the exact bandgap shape and position, still quite high powers can be extracted from fibers with far from optimum bandgap shape and position as long as care is taken to coil them properly.

Parasitic lasing investigation

Parasitic lasing has been investigated, being the most immediate limitation to the power scalability of the PBG fiber amplifiers. Figure 6.29 shows the amplified output signal relative to the bandgap position for PBG-2008-10.1 and PBG-2009-10.1, both coiled to a diameter of 26 *cm*. Though the bandgap positions are very similar, ASE is growing in PBG-2008-10.1 near the short-wavelength bandgap edge at 1144 *nm*, and eventually parasitic lasing starts just outside the bandgap at a wavelength of 1134 *nm*. In comparison, no ASE or parasitic lasing is present in the output spectrum

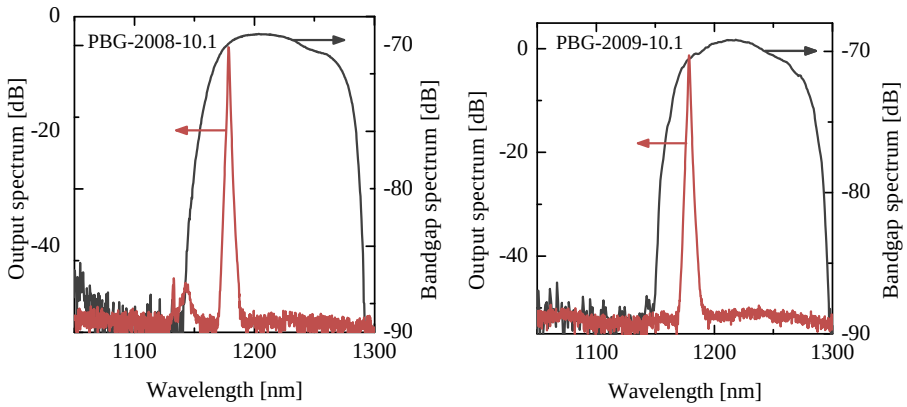

(a) (b)

Figure 6.29: Amplified output spectrum relative to the bandgap transmission spectrum for the two fibers PBG-2008-10.1 and PBG-2009-10.1. (a) For PBG-2008-10.1 parasitic lasing occurs outside the bandgap at a wavelength of 1134 nm and a power of 93 W at 1178 nm. (b) For PBG-1009-10.1 neither ASE nor parasitic lasing is present even at 167 W.

from PBG-2009-10.1. The spectrum of PBG-2008-10.1 is recorded for an output power of 93 W, while the output power of PBG-2009-10.1 is 167 W. The very small difference between the two fibers clearly illuminates the difficulty of long-wavelength amplification.

In figure 6.30(a) PBG-2008-10.1 is coiled to 25 cm. The ASE grows outside the bandgap at 1134 nm and parasitic lasing occurs more easily at an output power of only 20 W compared to the fiber coiled to 26 cm. The fact that parasitic lasing does not occur at the ytterbium gain peak but rather right outside the bandgap originates from pitch variations along the fiber length and from the quite long length of fiber used in the experiment. While a 1.5 m piece of fiber coiled to 26 cm has a bandgap span of 200 nm, the bandgap span of a 40 m long fiber is less than 150 nm, hence the wavelength of parasitic lasing can be well inside the bandgap for some shorter length of the fiber, while still being outside the bandgap for the full fiber length. This observation indicates that the road towards parasitic lasing free amplification goes through fibers with lower losses, shorter optimum lengths and smaller pitch variations along the fiber.

Figure 6.30(b) shows the amplified output spectra of PBG-2009-10.1 coiled to a diameter of 26 cm, and the fibers with pitches of 10.2 μm and 10.3 μm both coiled to a diameter of 32 cm. The spectrum of PBG-2009-10.1 does not show any ASE or parasitic lasing, while parasitic lasing arises in both PBG-2009-10.2 and PBG-2009-10.3. For PBG-2009-10.2 parasitic lasing occurs close to the bandgap edge at a wavelength of 1144 nm and an output power as high as 132 W. For PBG-2009-10.3 parasitic lasing occurs at the peak of the ytterbium gain band at a much lower power indicating that the losses at 1178 nm are much too high to sustain a good gain to loss ratio. Based on the loss measurements this behavior is expected.

Figure 6.31 shows CCD images of the output from PBG-2009-10.3 close to the parasitic lasing threshold in figure 6.31(a)and above the parasitic lasing threshold with a filter inserted to remove the amplified 1178 nm light in figure 6.31(b). The images indicate that parasitic lasing at wavelengths outside the bandgap is due to cladding modes overlapping with the ytterbium-doped core area.

Figure 6.30(c) shows the amplified output spectrum of PBG-2008-10.1 coiled to a diameter of 25 cm for different power levels – without pump power, at the parasitic lasing threshold level and above the threshold level. The parasitic lasing signal at the threshold is more than 30 dB below the amplified signal and will not cause a problem, however, above the threshold the self Q-switching nature of the laser generates giant pulses and therefore causes nonlinear broadening, mainly Raman scattering. The emission of light in unexpected directions can be very damaging to a laser system.

In spite of the challenges due the low small-signal gain at the long wavelengths, it was still possible to obtain a record-breaking high output power of 167 W at 1178 nm without any sign of ASE or parasitic lasing, and an output power of 132 W in a fiber with a less optimum bandgap position.

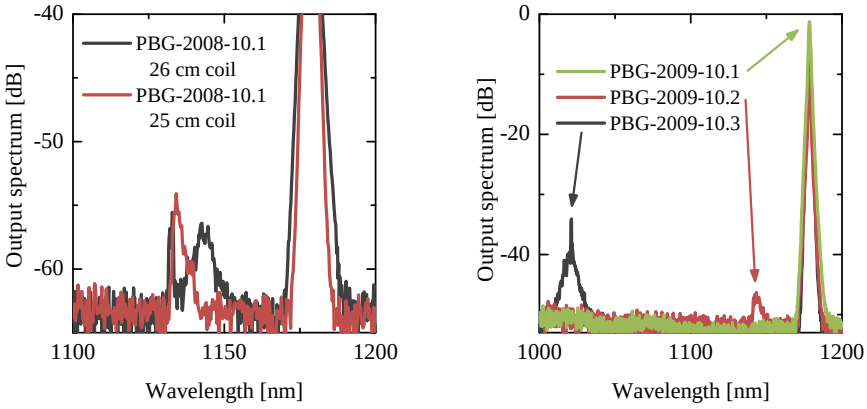

(a)

(b)

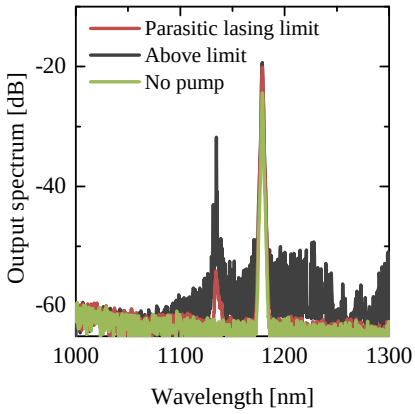

(c)

Figure 6.30: (a) Amplified output spectrum of PBG-2008-10.1 coiled to diameters of 26 *cm* and 25 *cm*. Parasitic lasing occurs more easily for the tighter coiled fiber. (b) Amplified output spectra of PBG-2009-10.1, PBG-2009-10.2, and PBG-2009-10.3. For PBG-2009-10.3 parasitic lasing occurs at the peak of the ytterbium gain band. (c) Amplified output spectra for PBG-2008-10.1 at different power levels, exemplifying the detrimental effect of parasitic lasing.

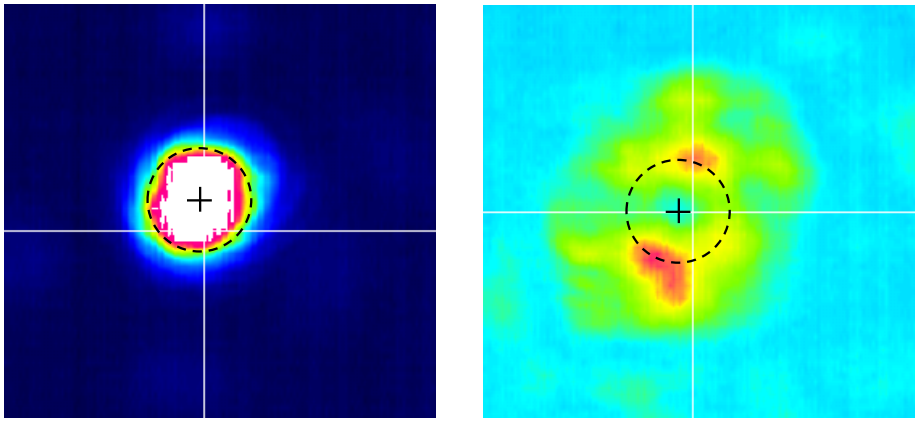

(a) (b)

Figure 6.31: (a) CCD image of the output from PBG-2009-10.3 close to the threshold for parasitic lasing. (b) Output from PBG-2009-10.3 above the threshold for parasitic lasing at a different gain setting and with a filter inserted for removing light at 1178 nm. The black cross indicates the position of the core center while the dotted ring encircles the ytterbium-doped region. Parasitic lasing occurring at wavelengths outside the bandgap is due to cladding modes with core overlap.

High power second harmonic generation at 589 nm

A natural next step is to pursue high power second harmonic generation to produce 589 nm light. Second harmonic generation is produced more efficiently with narrowband light and therefore the seed fiber Raman laser was exchanged to an all-fiber linearly polarized ytterbium-doped fiber laser [87, 102], which emits more than 2 W of output power with a 50 pm bandwidth at 1178 nm. The experimental setup is shown in figure 6.32. 1 W of launched seed power was amplified by 16 dB to 43 W by a PBG fiber amplifier based on PBG-2009-10.1. The bandwidth broadening after amplification is negligible as shown in figure 6.33, which is the 1178 nm output spectrum before and after amplification. In order to ensure efficient second harmonic generation, the polarization direction of the seed was adjusted to the slow axis along the boron-doped rods resulting in amplification with a polarization extinction ration of 17 dB. The second harmonics of the amplified 1178 nm light was generated by single-pass through a periodically-poled MgO-doped stoichiometric lithium tantalate

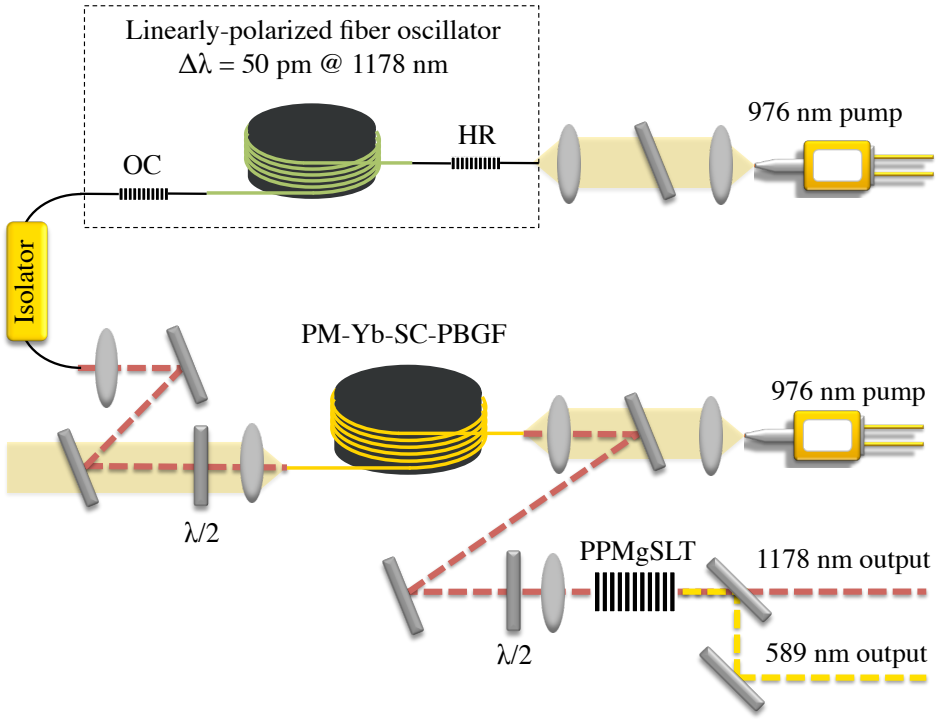

Figure 6.32: Experimental setup of the ytterbium fiber laser system for 589 nm generation consisting of a linearly polarized fiber oscillator, the PBG fiber amplifier and a PPmgSLT crystal.

crystal (PPMgSLT) [103, 104], which has the dimensions $2 \times 1 \times 30\ mm^3$, a pitch of 10.75 μm and a phase-matching temperature of $\sim 32°C$.

An output power as high as 14.5 W at 589 nm was generated from 43 W of 1178 nm light as shown in figure 6.34. The high conversion efficiency of 34% indicates that the output of the PBG fiber amplifier has excellent beam, polarization and bandwidth properties. In comparison with second harmonic generation in an LBO cavity [105], the present single-pass second harmonic generation holds advantages in terms of simplicity, robustness, and applicability to non-single frequency sources. Figure 6.35 is a photo showing the generated yellow light.

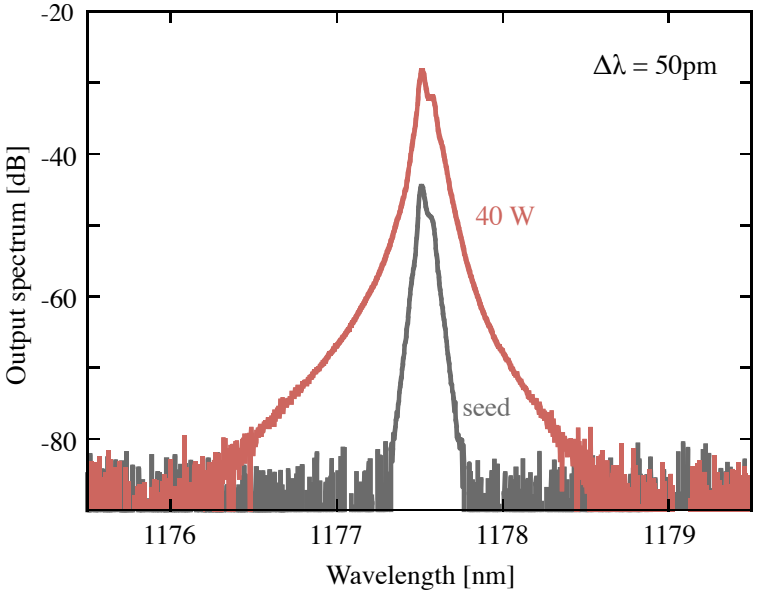

Figure 6.33: Spectra of the narrow linewidth seed and the amplified signal at 1178 *nm* showing little spectral broadening.

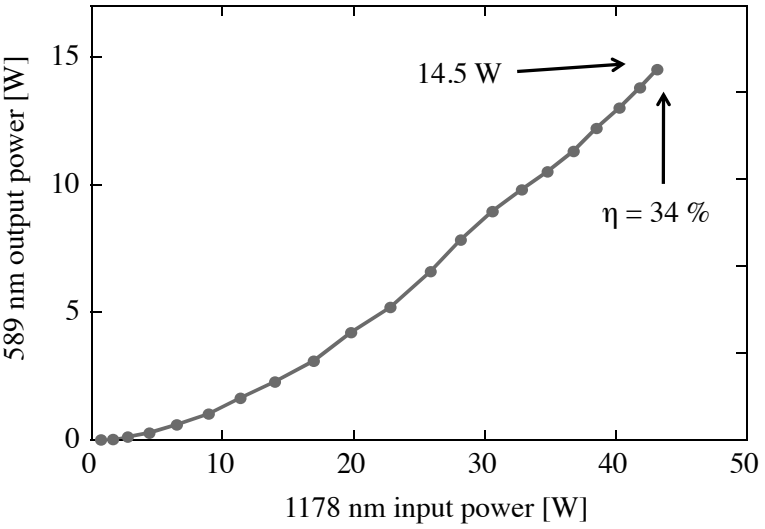

Figure 6.34: Output power at 589 *nm* as a function of 1178 *nm* input power. As high as 14.5 *W* is generated with the conversion efficiency reaching 34%.

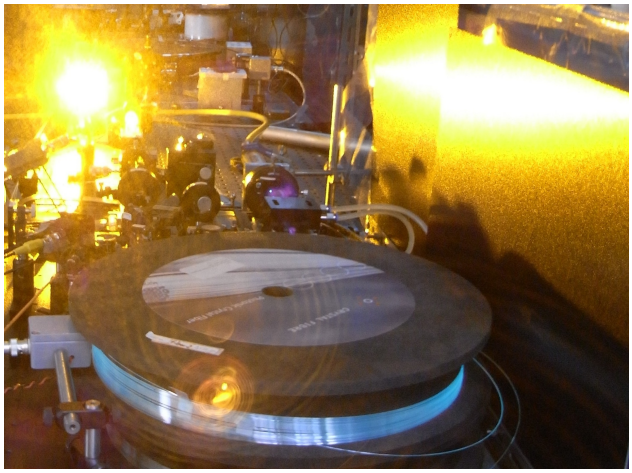

Figure 6.35: Photograph of the 589 nm light generated from the PBG fiber amplifier by single-pass through a PPMgSLT crystal.

Reliability

Due to the very high population inversion in the fiber, photo darkening poses a serious problem for the PBG fiber amplifier. Co-doping with cerium has been shown to mitigate photo darkening [65] and in an attempt to minimize the long-term degradation, a cerium co-doped PBG fiber was fabricated and tested. The fiber has very high losses on the order of 0.25 dB/m due to poor bandgap positioning and is therefore expected from calculations to produce a conversion efficiency below 40%. Amplification results with a 100 m long cerium co-doped fiber resulted in an output power of 67 W and a slope efficiency of 36% before the onset of parasitic lasing. The slope efficiency is consistent with the calculated value. The output power as a function of launched pump power is shown in figure 6.36.

A semi-long term amplifier test at 1178 nm performed with the cerium co-doped PBG fiber. To avoid drifts due to the high heat dissipation caused by the high losses in the fiber, the output power was kept below 20 W during the test. The output power as a function of time is shown in figure 6.37. During more than 8 hours the output power decreased ~5%, which can be attributed to drifts in the free space coupling as well as induced losses in the fiber. In comparison, the output power of the PBG fiber without cerium co-doping decreases by 50% in less than 30 minutes.

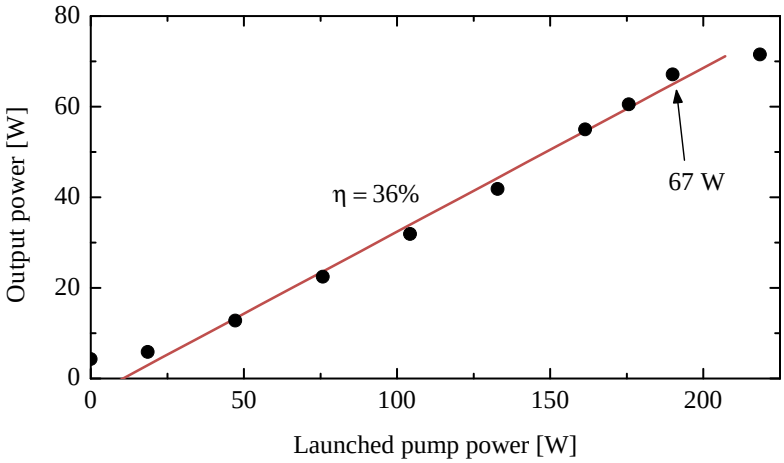

Figure 6.36: Output power as function of launched pump power for the cerium co-doped PBG fiber. The slope efficiency is consistent with the calculated value.

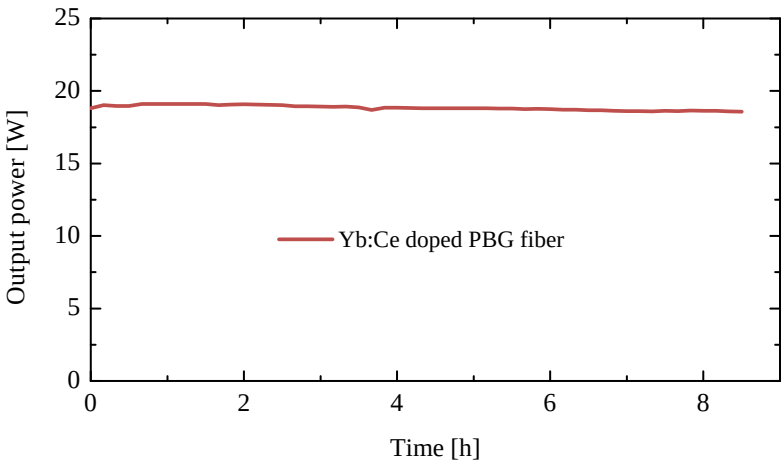

Figure 6.37: Semi-long term amplifier test of the cerium co-doped PBG fiber at 1178 *nm*. The output power is plotted as function of time and shows a decrease of around 5% over the course of more than 8 hours. The decrease can be attributed to drifts in the free space coupling as well as induced losses in the fiber.

Summary

The first part of this work demonstrates how the bandgap properties of an ytterbium-doped solid core PBG fiber can be controlled and how the ASE peak can be shifted by rescaling of the fiber design. In addition, low power amplification measurements show that the amplification scales with the ASE power and laser results show very efficient ASE suppression of up to 60 dB.

Using the amplifier model presented in section 3.3, the parameters for a high power amplifier at 1178 nm have been calculated and applied. Subsequently, a record output power of 167 W at 1178 nm and a slope efficiency of 61% using the PBG fiber amplifier has been demonstrated. The results obtained with this amplifier are, to our knowledge, the highest output powers generated from ytterbium fiber lasers and amplifiers at these long wavelengths and from PBG fibers lasers and amplifiers in general. Furthermore, since the output spectrum is free of ASE, scaling to even higher powers is possible in this fiber amplifier. The importance of exact positioning and shaping of the bandgap for optimum engineering of the ytterbium gain band has been demonstrated. In addition, other PBG fibers in which the output power at 1178 nm was limited by parasitic lasing due to less suitable bandgap shapes still reached power levels far above what has been achieved in other fiber lasers and amplifiers at this wavelength.

The good beam quality and polarization characteristics make the amplifier suitable for frequency doubling to the yellow-orange wavelengths. Second harmonic generation at 589 nm with 14.5 W of output power and a 34% conversion efficiency was demonstrated by single-pass through a PPMgSLT crystal. The second harmonic generation at 589 nm can be expected to exceed 14.5 W if a stronger seed is used.

The PBG fiber amplifier concept has shown itself very promising for high power applications and can easily be extended to other wavelengths in the ytterbium gain region – even as high as 50% conversion efficiency can be expected at 1200 nm [106]. Furthermore, gain profiling by the PBG technique can also be extended to other rare earth doped fibers. Finally, initial results with a cerium co-doped PBG fiber show great promise with respect to limiting the effect of photo darkening.

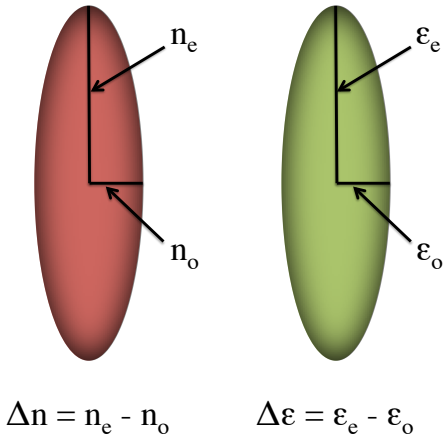

Figure 6.38: Axes of the refractive index and the dielectric permittivity in a single liquid crystal molecule.

6.2 Liquid crystal photonic bandgap fiber laser

The design structure of PCFs offers the unique possibility of infiltrating the airholes of a TIR guiding PCF with a high-index liquid material and thereby give rise to guidance by the photonic bandgap (PBG) effect. Among high-index liquid materials, liquid crystals (LCs) exhibit large electro-optic and thermo-optic effects due to high birefringence ($\Delta n \sim 0.8$) [107] and large dielectric anisotropy ($\Delta\epsilon \sim 70$) [108]. The axes of the refractive index and the dielectric permittivity in a single rod-like liquid crystal molecule are illustrated in figure 6.38.

Thermotropic LCs are LCs that exist in different temperature dependent phases where the positional and orientational order changes, giving rise to changes in the optical properties. Positional order is when the molecules are arranged in an ordered lattice and orientation order is when the molecules are pointing in the same direction.

A change in temperature induces a change in the extraordinary (n_e) and ordinary (n_o) refractive indices, which in turn causes a change in the birefringence, Δn, a feature which is exploited for making temperature tunable devices out of LCs. In addition, the LCs have a fluidity like isotropic liquids but can easily be aligned by an external electric field

due to the fact that the dielectric constants along the two molecular axes have different values. The dielectric anisotropy, $\Delta\epsilon$, can be either positive or negative depending on the LC and the applied frequency. When an electric field is applied to an LC with a positive dielectric anisotropy, the LC director – the vector representing the preferred direction of the molecule – will turn into the field direction, while an LC with a negative dielectric anisotropy will turn perpendicular to the field direction.

These features of LCs are very unique and can be exploited to control the bandgap properties of the fiber in order to fabricate all-in-fiber devices employing either thermal or electrical tunability [109–111]. A number of such liquid crystal photonic bandgap (LCPBG) devices have been demonstrated [112–123].

Combining the wavelength filtering effect of PBG confinement with an ytterbium-doped core has in the previous section been used in solid core PBG fiber lasers and amplifiers. The bandgap efficiently suppresses the amplified spontaneous emission (ASE) at the conventional ytterbium gain wavelengths around 1030 *nm* and enables both short- [91] and long-wavelength operation [90]. In this work we merge the PBG fiber laser concept with the tunability offered by LCs to create a fiber laser with electrical tunability in the range 1040-1065 *nm*. We fabricate an all-spliced laser cavity based on the liquid crystal infiltrated PCF mounted on a silicon assembly, a pump/signal combiner with single-mode signal feed-through and a single-mode ytterbium-doped photonic crystal fiber. The presence of a bandgap in the laser cavity will inhibit lasing at certain wavelengths – thus, by applying an electric field to an intra-cavity LC infiltrated PCF the bandgap position can be shifted, resulting in laser tunability. This is to our knowledge the first LC based electrically tunable fiber laser. The device holds potential as a low-cost tunable seed source for ytterbium fiber amplifiers.

Liquid crystal photonic bandgap fiber

The LC used in the present work is a dual-frequency LC (MDA-00-3969, Merck), which means that $\Delta\epsilon$ is positive at low frequencies and negative at high frequencies. Polarization microscopy studies of this LC show that it is aligned in a splay configuration with an angle of 45°at the boundary surface [114]. At room temperature the LC is in the nematic phase where

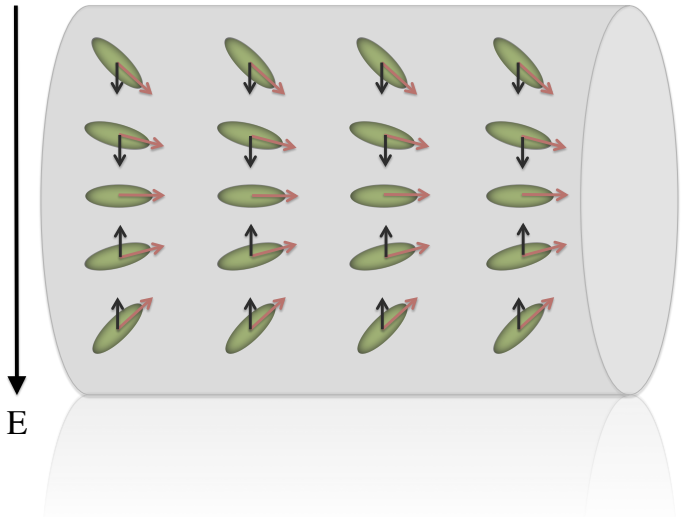

Figure 6.39: Illustration of an enlarged capillary filled with LC. The red arrows show the orientation of the LC director, while the black arrows show the direction along which the LC tends to reorient when a 1 kHz field is applied.

the molecules possess orientational order but not positional order. When an electric field is applied to the LC it exerts a torque on the LC director, which is rotated parallel or perpendicular to the field direction, depending on the sign of the dielectric anisotropy. In general, dual-frequency LCs behave differently depending on the frequency of the applied electric field. For the present LC the dielectric anisotropy is positive if the electric field is below 15 kHz and negative if the electric field is above this value, hence allowing for electric control of the spectral position of the bandgap towards both shorter and longer wavelengths in the same device. A frequency of 1 kHz is used in the experiment since we wish to operate the laser close to the short-wavelength edge of the bandgap and tune the bandgap edge towards longer wavelengths. Figure 6.39 shows an enlargement of a single capillary filled with LC. The red arrows show the orientation of the LC director, while the black arrows show the direction along which the LC tends to reorient when a 1 kHz field is applied. The LC has wavelength dependent ordinary and extraordinary refractive indices of $n_o = 1.4978$ and $n_e = 1.7192$, respectively, at $T = 20°C$ and $\lambda = 589.2\ nm$. Previous studies of this LC [114] show that the response time is in the ms range. The rise

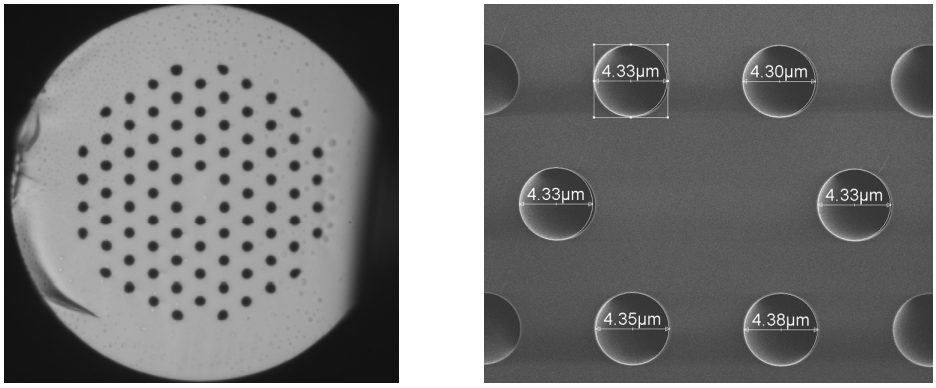

(a) (b)

Figure 6.40: (a) Microscope image of the end facet of the PCF. (b) SEM image of the first ring of airholes.

time is about 3 ms for a voltage of 100 V_{rms} at 1 kHz, while the decay time is 12 ms.

The fiber used in the experiment is a large-mode-area PCF (LMA-13) with a hole diameter of 4.3 μm, an inter-hole distance of 8.5 μm and a cladding diameter of 125 μm. The 13 μm core is surrounded by five rings of airholes arranged in a hexagonal lattice. The LC is infiltrated by capillary forces without application of external forces in order to minimize deformations of the LC alignment. The LC infiltrated section of the fiber is 13 mm long. Two images of the fiber end facet is shown in figure 6.40. A typical transmission spectrum of LMA-13 PCF infiltrated with MDA-00-3969 is shown in figure 6.41. The bandgap position is well suited for filtering around the ytterbium gain wavelengths 1030–1080 nm.

Electrically controlled LCPBG fiber device

When the LCPBG fiber is placed between electrodes, the spectral position of the bandgaps in the LC filled section of the fiber can be electrically tuned. Applying a 1 kHz sine wave in bipolar mode across the fiber causes the refractive index in the transverse plane to increase thus shifting the bandgap towards longer wavelengths as shown in figure 6.42. The short-wavelength bandgap edge is situated around the typical ytterbium gain wavelengths

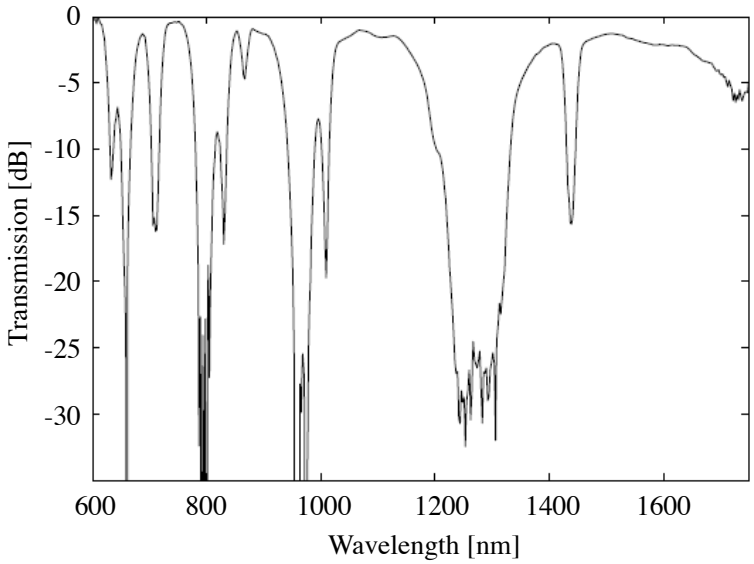

Figure 6.41: Typical transmission spectrum of an LMA-13 PCF infiltrated with MDA-00-3969.

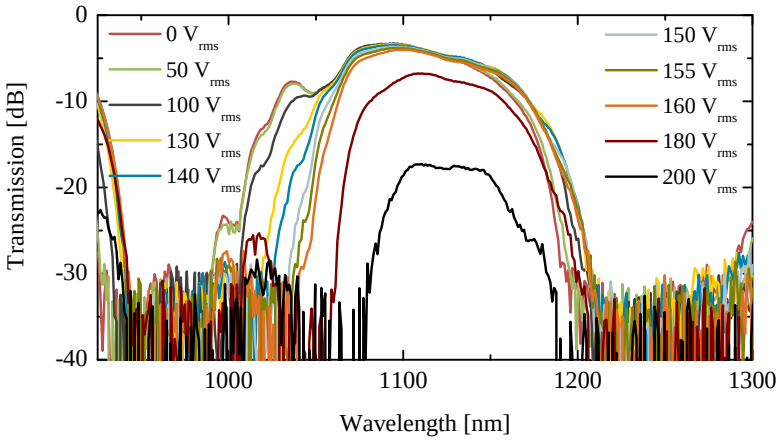

Figure 6.42: Transmission spectrum of the LCPBG device as a function of applied voltage. The frequency of the applied electric field is 1 kHz.

1030–1080 nm, which makes the device well suited for an ytterbium-doped fiber laser. This position of the short-wavelength edge of the bandgap allows for filtering of short-wavelength ASE which is the main limitation in ytterbium-doped fiber lasers. When the voltage is increased, the bandgap edge and the laser wavelength will move towards longer wavelengths. The main loss mechanism is coupling loss between the TIR mode of the unfilled fiber and the PBG mode of the filled fiber. At voltages above 160 V_{rms} the transmission becomes lossy as the PBG mode becomes less confined in the silica core.

Packaging of the LCPBG fiber device is critical in order to achieve a compact and easy-to-use device. The LC infiltrated section of the LMA-13 is placed in a v-groove fabricated on a silicon substrate and the end facet is placed just outside the chip in order to enable coupling of light as shown in figure 6.43. A front view illustration and image is shown in figure 6.44. A pair of Au electrodes is deposited on the sidewalls of the groove, and the electrode patterning is achieved by using thick photoresist coating and two-step exposure [124]. The electrodes are electrically isolated from the silicon substrate by a 2 μm SiO2 layer and a thin titanium layer is used as an adhesion layer between the electrodes and the isolation layer. A top lid containing a v-groove with the other pair of electrodes is placed on top of the fiber, forming two sets of electrodes, which fix the fiber at four orthogonal corners relative to the fiber core. In order to ensure a good contact between the LCPBG fiber and the electrodes, SU-8 fiber fixing structures are built up on the electrodes [125]. The height of each SU-8 structure is 84 μm and the distance between two neighboring structures is 126 μm, taking the small variation of the fiber outer diameter into account. The assembly is sealed with epoxy.

All-spliced laser cavity with single-mode combiner

The all-spliced fiber assembly is comprised of the LCPBG fiber device, an ytterbium-doped airclad PCF, a pump diode and a 6+1:1 pump/signal combiner for airclad fibers with polarization-maintaining (PM) single-mode signal feed-through. The combiner is designed for 0.15 NA pump diodes, and in order to utilize the high NA supported by airclad fibers, it features a special taper element [126].

An illustration of the all-spliced laser cavity is shown in figure 6.45.

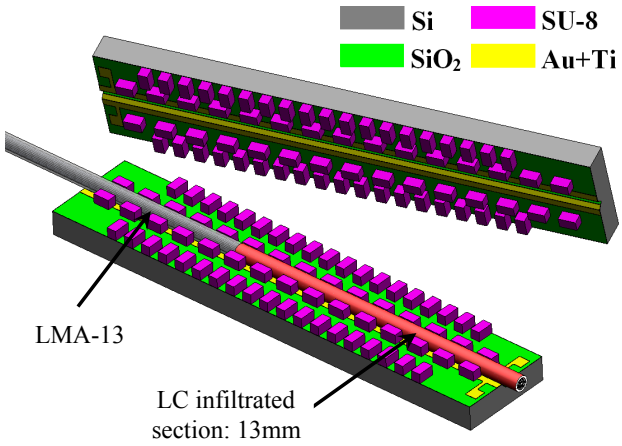

Figure 6.43: Illustration of the silicon assembly for the LCPBG device.

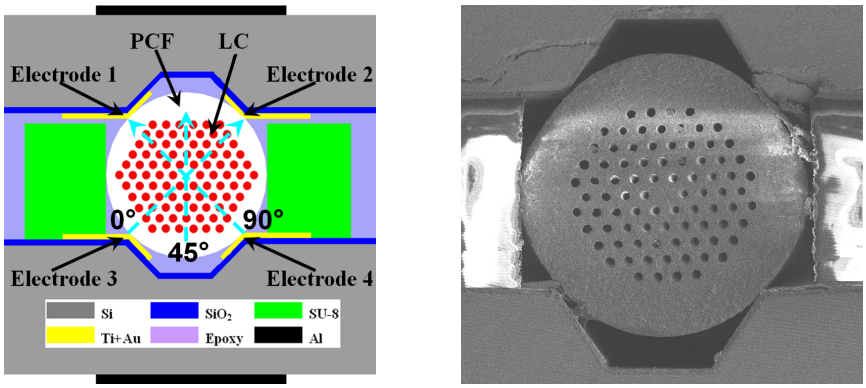

(a) (b)

Figure 6.44: (a) Front view illustration of the silicon assembly. Three different electric field directions can by applied to the LCPBG device by using different combinations of the four electrodes. (b) Front view SEM image of the LMA13 PCF placed in the silicon assembly.

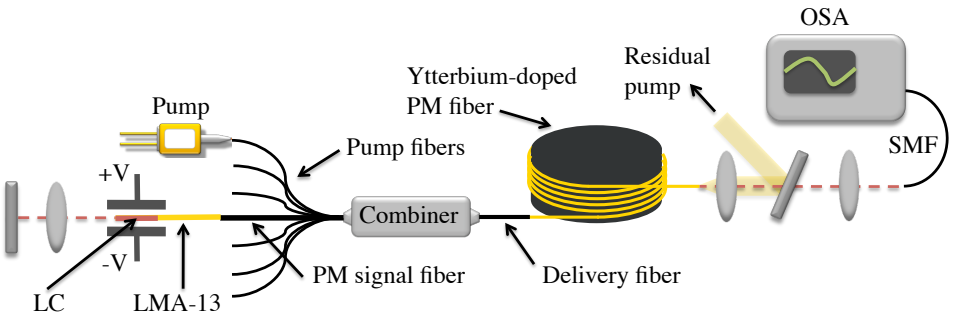

Figure 6.45: All-spliced laser cavity setup from the left: cavity mirror, LCPBG fiber mounted on a silicon assembly, pump/signal combiner with single-mode signal feed-through, ytterbium-doped PCF, long wave pass filter, and OSA.

The LCPBG fiber device is spliced to the single-mode signal feed-through of the combiner, while the delivery fiber of the combiner is spliced to a PM ytterbium-doped airclad PCF. The laser cavity is formed by a lens and silver mirror after the LCPBG fiber device and the cleaved end facet of the ytterbium-doped PCF. The ytterbium-doped PCF has a pump cladding diameter of 105 μm, a mode field diameter of 12 μm and is cleaved at a 0° angle to allow for approximately 4% reflectivity. With a pump absorption of ~3 dB/m and a length of 4 m it is optimized for 976 nm pumping. The residual pump is filtered by a long-wave pass filter at the output of the laser cavity, while the laser signal spectrum is recorded by an OSA. Besides ease-of-use and compactness, an incentive to use the pump/signal combiner rather than pumping through a dichroic mirror is that cladding-pumping directly through the LC filled section might affect the behavior of the LC.

Tunability of the LCPBG fiber laser

Bandgap tunability of the all-spliced fiber assembly is investigated by applying a voltage of up to 200 V_{rms} to the LCPBG device. Figure 6.46 shows the transmission spectra of the assembly for different voltage settings. Below 100 V_{rms} the bandgap is unchanged, from 100-160 V_{rms} the short-wavelength edge of the bandgap is shifted towards longer wavelengths by approximately 25 nm. Above 160 V_{rms} the losses in the bandgap increase dramatically. The total loss in the cavity due to the LC insertion, the combiner and splices is measured to approximately 6 dB and is mainly

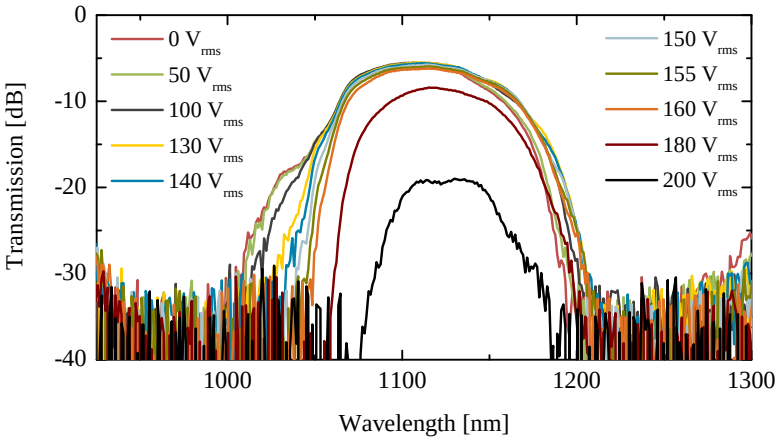

Figure 6.46: Transmission spectrum of the all-spliced fiber assembly. The short-wavelength bandgap edge is shifted towards longer wavelengths when a voltage is applied. Above 160 V_{rms} the losses in the bandgap become high.

due to mode-matching errors at the interface between the LMA fiber and the PM signal feed-through fiber and due to coupling losses between the TIR mode and the PBG mode of the LMA fiber. Considering the high losses in the bandgap above 160 V_{rms}, the laser cavity is only expected to be tunable at low voltage setting. A near field image of the single-mode output from the laser cavity is shown figure 6.47.

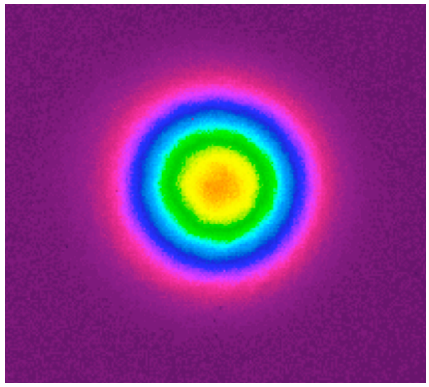

Figure 6.47: Near field image of the single-mode output from the laser cavity.

In PBG fiber lasers, lasing will occur at the wavelengths that experience the least loss due to the bandgap combined with the highest gain due to their emission cross section – these wavelengths are close to the short-wavelength edge of the bandgap. Fiber lasers based on active PBG fibers typically have distributed spectral filtering along the whole length of the fiber in order to reduce ASE, whereas in the LCPBG device the LC infiltrated section is only 13 mm long. Hence, ASE will inevitably build up in the ytterbium-doped fiber, resulting in parasitic lasing which will limit the tunability and power scalability of the LCPBG fiber laser.

Figure 6.48 shows the laser transmission spectra compared to the bandgap transmission spectra for three different voltage setting, 0 V_{rms}, 150 V_{rms}, and 160 V_{rms}. For low voltages the ASE peak is well inside the bandgap and therefore tuning of the bandgap edge does not affect the lasing wavelength significantly. For higher voltages the ASE peak is outside the bandgap, while the laser wavelength is tuned inside the bandgap. For voltages of 160 V_{rms} and higher, the loss inside the bandgap becomes too high leading to parasitic lasing outside the bandgap. Had a frequency above 15 kHz been applied instead, the bandgap edge would have moved towards shorter wavelengths, the ASE peak around 1040 nm would have remained inside the bandgap, and tuning of the laser would have been impossible.

Figure 6.49 shows the narrow laser spectra of the cavity for different voltage settings. The laser wavelength is shifted towards longer wavelengths by approximately 25 nm. The pump power is increased between each measurement to keep lasing just above threshold and as a consequence ASE builds up in the cavity when the pump power is increased. The ASE build-up causes parasitic lasing at shorter wavelengths for voltages around 160 V_{rms} and higher, eventually limiting both the power and the tuning range of the laser. The laser wavelength is plotted as a function of applied voltage in figure 6.50. The wavelength is constant at 1040 nm below 130 V_{rms} and tunable up to 1065 nm at 155 V_{rms}.

We have shown that the lasing wavelength is determined by the position of the bandgap edge of the LCPBG device, which in turn is influenced by the refractive index structure in the LC. Since the LC is splay aligned the modes in the capillaries see a spatially varying anisotropic refractive

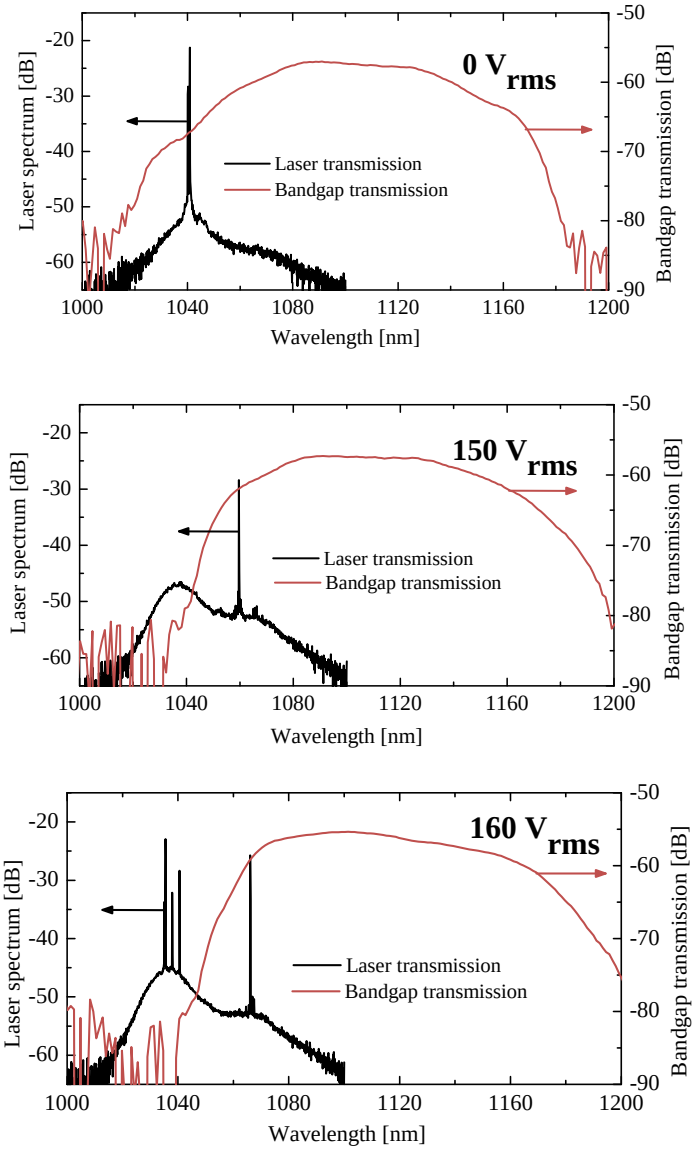

Figure 6.48: Laser transmission spectra compared to bandgap transmission spectra for two different voltage settings, 0 V_{rms}, 150 V_{rms}, and 160 V_{rms}. The plots show how the cavity is lasing close to the short-wavelength bandgap edge. Parasitic lasing outside the bandgap will limit the power and tunability of the laser at high voltages.

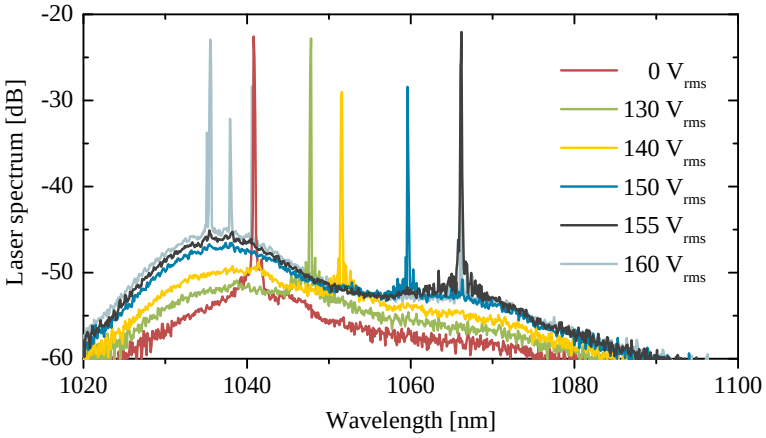

Figure 6.49: The laser wavelength is shifted towards longer wavelengths. At 160 V_{rms} parasitic lasing sets in at shorter wavelengths. A total shift of 25 nm is observed.

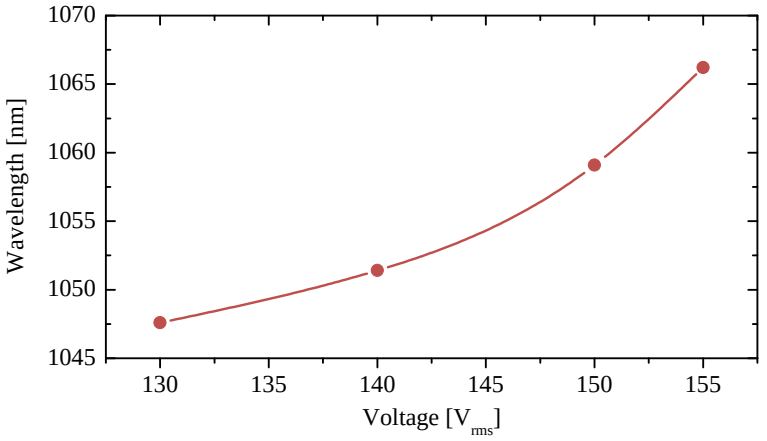

Figure 6.50: The laser wavelength plotted as a function of applied voltage. Tuning starts at 130 V_{rms}. The wavelength is constant at 1040 nm below 130 V_{rms}.

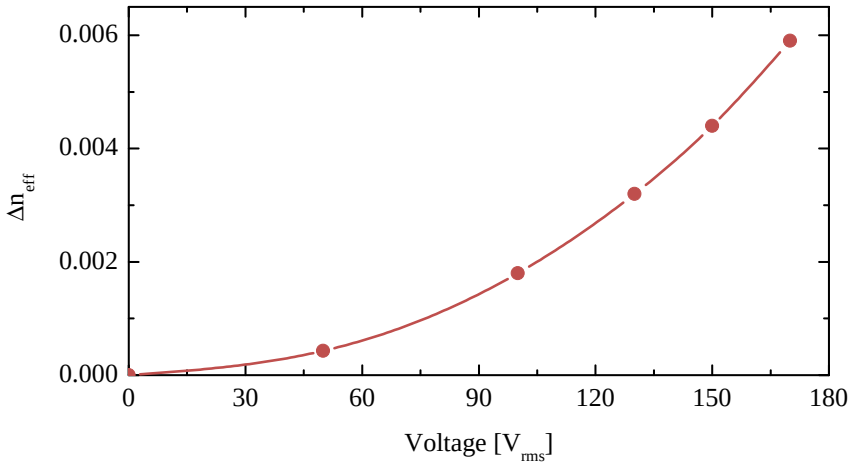

Figure 6.51: Simulated change of effective index of the capillary mode responsible for the short-wavelength bandgap edge. The dependence of the effective index shift on the applied external field is found to be quadratic.

index structure which changes when an external electric field is applied. The change in effective index is determined by the orientation of the LCs and this reorientation depends quadratically on the applied electric field [127, 128]. Figure 6.51 shows the simulated change of effective index of the capillary mode responsible for the short-wavelength bandgap edge. Also here we find a quadratic dependence of the effective index shift on the applied external electric field. Thus, as expected the tuning in figure 6.50 is not linear.

The laser cavity produced an output of $\sim$30 mW with the efficiency of the laser strongly limited by losses in the cavity. With optimization of cavity optics, fiber cleave angles, LC device, and mode-matching between fibers, losses can be reduced and potentially allow for the production of an easily tunable, single-mode output signal, which can be used to seed a fiber amplifier. The present cavity yields up to 25 dB of ASE suppression, however an improved cavity with reflectors in both ends is expected to improve the ASE suppression significantly. The polarization-maintaining properties of the device are expected to be good.

Summary

This section has described the fabrication of an all-spliced fiber laser cavity with a single-mode output, which is electrically tunable from 1040 nm to 1065 nm. The device is based on an LCPBG fiber mounted on a silicon assembly, a pump/signal combiner and an ytterbium-doped PCF. The LCPBG fiber device induces a bandgap in the cavity, which is tuned by an electric field and is used to shift the laser wavelength by 25 nm. This is to our knowledge the first LC based electrically tunable fiber laser.

With improvements to the system, the device holds potential as a low-cost, compact and easy-to-use tunable seed source for fiber amplifiers. Improvements can be obtained by reducing the cavity losses or by reducing the number of components and interfaces in the cavity, for example by infiltrating LC directly in an ytterbium-doped PCF.

Chapter 7

Conclusion

Since the first demonstration of photonic crystal fibers in 1996, the development has progressed fast towards higher powers for applications in material processing and in defense. Photonic crystal fibers hold advantages over standard step-index fibers in terms of superior index control due to the microstructuring process. This enables manufacturing of flexible single-mode fibers which are about an order of magnitude larger than step-index fibers – and larger cores allows for higher power levels and less nonlinearities. Besides enabling high power, the microstructuring process also provides the fiber designer with a unique flexibility to incorporate special features such as filtering functions into the fibers.

Pushing the limits of photonic crystal fibers – both with respect to power and to special features – entails many challenges which are all very different in nature. The work presented in this thesis has covered a range of topics within the field of photonics crystal fibers for high power applications, with the one common goal of addressing some of the challenges involved in developing better fibers for high power applications or introducing new functionality in fibers.

One issue addressed in the thesis was photo darkening. Photo darkening is found to scale with doping concentration and population inversion and is therefore detrimental to high power lasers and amplifiers. The advantages of mitigating photo darkening in fibers are considerable – with a low photo darkening material composition, the doping concentration can be increased, the fiber length can be shortened, the nonlinear effects diminished

and the power can be increased. The aim of the investigation was to develop a procedure for benchmarking different material compositions and to support the development of a model describing the photo darkening process. Fibers with different co-doping materials – mainly aluminium and phosphor – and varying doping concentrations have been tested in the investigation and the results have supported the general presumptions from the model and literature. The main conclusions are that the induced loss due to photo darkening has a second-order power dependence on the population inversion, that photo darkening increases with ytterbium concentration and decreases linearly with aluminium concentration – in a specific case the induced loss was seen to decrease by a factor of two when the aluminum concentration was increased by the same factor. Furthermore, results show that co-doping with phosphor improves the photo darkening by more than an order of magnitude compared to aluminium, but at the expense of slope efficiency. A decrease in slope efficiency of 20% has been observed, however, the right combination of aluminium and phosphor co-doping should feature the benefits of phosphor without compromising the slope efficiency. The tests have contributed to a model, which is now used to compound new material compositions that are subsequently benchmarked experimentally in the accelerated setup.

The work involved with benchmarking new material compositions is ongoing, and due to the increasing demand for higher powers and more reliable systems, the quest for better materials is important. It has recently been suggested that co-doping with cerium will mitigate photo darkening and initial tests have confirmed the tendency. Tests with new materials such as cerium is a sure part of the future work on mitigation of photo darkening and is expected to reduce the induced losses by more than an order of magnitude.

Besides mitigation of photo darkening, the road towards high powers in short fibers with high nonlinearity threshold is through more efficient pump absorption, which is the subject of the next investigation. It has been suggested that low NA light is less efficiently absorbed by the core material, but that the presence of one or more holes in the pump cladding induces chaotic behavior in the beam path, thereby improving the pump absorption. The pump absorption is also increased by periodic bending of the fiber, however this is not always practical in industrial applications.

The main conclusions from the investigation are that low NA light is in fact less efficiently absorbed as suggested by literature, that the hole structure of PCFs improves the pump absorption by more than a factor of two compared to step-index fibers to an extent that periodic bending is not necessary for PCFs. Furthermore, results show that even straight PCFs, such as rod-type fibers, absorb the pump light as well as a coiled fibers, that only a few holes or stress rods in the cladding also scramble the light and improve the pump absorption, but not nearly as well as a full PCF structure, and that the airclad structure surrounding the pump cladding holds no significant advantage over a polymer-cladding with respect to pump absorption. The findings are very relevant for high power applications as coiling of the fibers plays a significant role when packaging and thermal handling is to be optimized in the manufacturing of high power lasers and amplifiers.

The subsequent part of the work has been concerned with improving the properties of PCFs with very large cores and has involved developing a method for characterizing the fibers to ensure good beam quality and stability. Two of the largest flexible fibers were used in the investigation – a fiber with a 40 μm core and a fiber with a 30 μm core. The index of the core material is typically known with an accuracy of 10^{-5} and additional fine-tuning of the index step is done by making small changes to the hole size in the cladding. Therefore, for several different hole sizes, the stability and the single-mode behavior was tested, while the fibers were bend to different diameters in order to determine the limits for single-mode operation. The work also involved the elimination of twist and tilt in the fibers to ensure a predictable bend behavior, which is crucial to the mode quality and stability. Combined with the elimination of twist and tilt in the fibers, the characterization tools have enabled the development of one of the largest and most stable flexible LMA fibers on the market. Furthermore, development of rod-type fibers with 100 μm cores and tools to evaluate the mode quality of both flexible fibers and rod-type fibers in a more quantitative manner – for example by means of S^2-imaging – has been initiated.

The future development of fibers for high power applications is inevitably towards larger and larger single-mode cores. The core size limit of flexible fibers is close to the current 40 μm in a simple PCF design, however, further scaling may be possible through fiber designs which filter

out higher-order modes by resonant coupling rather than by bending. Initial design tests show great promise. This approach may also be applicable to rod-type fibers for even larger cores.

The largest part of the work has focused on the incorporation of filtering functions in the fibers. The wavelength filtering effect of PBG confinement has been combined with a doped core in an ytterbium-doped PBG fiber, designed to suppress ASE at the conventional ytterbium gain wavelengths and to shape the gain for amplification in the long-wavelength region of the gain band – in particular at 1178 nm. By accurate tailoring of the gain, a record high output power of 167 W at 1178 nm has been achieved. This is to our knowledge the highest output power generated from ytterbium fibers at these long wavelengths and from PBG fibers in general. In addition, the work involved narrowband 589 nm second harmonic generation in a single-pass configuration with an output power of 14.5 W and an efficiency of 34%, making the fiber amplifier promising for laser guide star applications.

Secondly, filtering was introduced by infiltrating the holes of a PCF with high-index liquid crystals, resulting in PBG guidance in the infiltrated part of the fiber. The fiber was placed in a laser cavity such that the presence of the bandgap would inhibit lasing at certain wavelengths. The bandgap position was shifted by applying an electric field to the liquid crystals, resulting in laser tunability in the wavelength region 1040–1065 nm. This is to our knowledge the first liquid crystal based electrically tunable fiber laser, and the device holds potential as a low-cost, compact and easy-to-use tunable seed source for ytterbium fiber amplifiers.

The possibilities to improve and develop the current PBG fiber amplifier concept are manifold. One prerequisite for efficient long-wavelength amplification is a material composition with low photo darkening. While a traditional ytterbium fiber amplifier operates with a population inversion of up to $\sim$0.15, the population inversion in an 1178 nm amplifier can reach more than 0.3 due to the low emission cross section at this wavelength. With a high-order dependence on the population inversion, photo darkening is much more serious at longer wavelengths and for this purpose cerium co-doping may be an option. While the current PBG fiber is very efficiently amplifying to high powers, the small core and the long length of the

fiber give rise to a low SBS threshold, when the signal linewidth becomes extremely narrow. Single-frequency amplification is only possible up to a few watts in the current design, and since efficient intra-cavity frequency doubling requires a linewidth below the MHz-level, a future challenge will be to overcome the SBS limitation, for example by increasing the core size. In the current design, the core size is related by design to the operational wavelength and scaling of the core becomes difficult, however, the same type of distributed filtering can also be achieved by placing resonant structures in a traditional PCF cladding, enabling core sizes up to 40 μm. The design with resonant structures has the additional advantage that the width of the bandgap can be tailored as well as the position. Furthermore, it has recently been suggested that the SBS threshold can be increased by inducing variation in the acoustic velocity across the core. Future work with the solid core PBG fiber for 1178 nm amplification inevitably involves work on better 589 nm generation. The PBG fiber amplifier concept could also be extended to other rare-earth materials and to other wavelength regions for suppression of other nonlinear effects such as SRS.

In general, the future of photonic crystal fibers for high power applications lies in obtaining larger cores with stable, fundamental mode operation in systems with good long-term reliability. The topics covered in this thesis have touched upon a few of the challenges involved in improving the reliability, efficiency, stability, and mode quality of the large core fibers, as well as extending the functionality of the fibers to new wavelength regions.

Bibliography

[1] S. John, "Strong localization of photons in certain disordered dielectric superlattices," Physical Review Letters **58**(23), 2486–2489 (1987).

[2] E. Yablonovitch, "Inhibited Spontaneous Emission in Solid-State Physics and Electronics," Physical Review Letters **58**(20), 2059–2062 (1987).

[3] J. C. Knight, J. Broeng, T. A. Birks, and P. S. J. Russell, "Photonic Band Gap Guidance in Optical Fibers," Science **282**(5393), 1476–1478 (1998).

[4] J. C. Knight, T. A. Birks, P. S. J. Russell, and D. M. Atkin, "All-silica single-mode optical fiber with photonic crystal cladding," Optics Letters **21**(19), 1547–1549 (1996).

[5] W. J. Wadsworth, J. C. Knight, W. H. Reeves, P. S. Russell, and J. Arriaga, "Yb3+-doped photonic crystal fibre laser," Electronics Letters **36**(17), 1452–1454 (2000).

[6] A. Tünnermann, T. Schreiber, and J. Limpert, "Fiber lasers and amplifiers: an ultrafast performance evolution," Applied Optics **49**(25), F71–F78 (2010).

[7] T. Eidam, S. Hanf, E. Seise, T. V. Andersen, T. Gabler, C. Wirth, T. Schreiber, J. Limpert, and A. Tünnermann, "Femtosecond fiber CPA system emitting 830 W average output power," Optics Letters **35**(2), 94–96 (2010).

[8] A. K. Sridharan, P. Pax, M. J. Messerly, and J. W. Dawson, "High-gain photonic crystal fiber regenerative amplifier," Optics Letters **34**(5), 608–610 (2009).

[9] F. Roeser, C. Jauregui, J. Limpert, and A. Tünnermann, "94 W 980 nm high brightness Yb-doped fiber laser," Optics Express **16**(22), 17,310–17,318 (2008).

[10] F. D. Teodoro and C. D. Brooks, "Multi-MW peak power single-transverse mode operation of a 100 micron core diameter, Yb-doped photonic crystal rod amplifier," in *Fiber Lasers IV: Technology, Systems, and Applications*, D. J. Harter, A. Tünnermann, J. Broeng, and C. H. III, eds., vol. 6453, p. 645318 (SPIE, 2007).

[11] F. D. Teodoro, M. K. Hemmat, J. Morais, and E. C. Cheung, "High peak power operation of a 100 mu m-core Yb-doped rod-type photonic crystal fiber amplifier," in *Fiber Lasers VII: Technology, Systems, and Applications*, K. Tankala, ed., vol. 7580, p. 758006 (SPIE, 2010).

[12] C. B. Olausson, A. Shirakawa, M. Chen, J. K. Lyngsø, J. Broeng, K. P. Hansen, A. Bjarklev, and K. Ueda, "167 W, power scalable ytterbium-doped photonic bandgap fiber amplifier at 1178nm," Optics Express **18**(16), 16,345–16,352 (2010).

[13] S. Jetschke and U. Röpke, "Power-law dependence of the photodarkening rate constant on the inversion in Yb doped fibers," Optics Letters **34**(1), 109–111 (2009).

[14] J. Koponen, M. Söderlund, H. J. Hoffman, D. Kliner, and J. Koplow, "Photodarkening measurements in large mode area fibers," in *Fiber Lasers IV: Technology, Systems, and Applications*, D. J. Harter, A. Tünnermann, J. Broeng, and C. H. III, eds., vol. 6453, p. 64531E (SPIE, 2007).

[15] C. B. Olausson, K. P. Hansen, and A. Bjarklev, "Pump Absorption in Airclad Step Index and Photonic Crystal Fibres for High Power Applications," in *CLEO/Europe and EQEC 2009 Conference Digest*, p. CJ1_6 (Optical Society of America, 2009).

[16] N. Saito, K. Akagawa, M. Ito, A. Takazawa, Y. Hayano, Y. Saito, M. Ito, H. Takami, M. Iye, and S. Wada, "Sodium D2 resonance radiation in single-pass sum-frequency generation with actively mode-locked Nd:YAG lasers," Optics Letters **32**(14), 1965–1967 (2007).

[17] F. Zolla, G. Renversez, A. Nicolet, B. Kuhlmey, S. Guenneau, and D. Felbacp, *Foundations of photonic crystal fibres* (Imperial College Press, 2005).

[18] T. A. Birks, J. C. Knight, and P. S. Russell, "Endlessly single-mode photonic crystal fiber," Optics Letters **22**(13), 961–963 (1997).

[19] R. Syms and J. Cozens, *Optical guided waves and devices* (McGraw-Hill, 1992).

[20] N. A. Mortensen, J. R. Folkenberg, M. D. Nielsen, and K. P. Hansen, "Modal cutoff and the V parameter in photonic crystal fibers," Optics Letters **28**(20), 1879–1881 (2003).

[21] J. Broeng, D. Mogilevstev, S. E. Barkou, and A.Bjarklev, "Photonic Crystal Fibers: A New Class of Optical Waveguides," Optical Fiber Technology **5**(3), 305–330 (1999).

[22] N. A. Mortensen and J. R. Folkenberg, "Low-loss criterion and effective area considerations for photonic crystal fibres," Journal of Optics A: Pure and Applied Optics **5**(3), 163 (2003).

[23] M. Nielsen, J. Folkenberg, and N.A.Mortensen, "Singlemode photonic crystal fibre with effective area of 600 μm^2 and low bending loss," Electronics Letters **39**(25), 1802–1803 (2003).

[24] M. D. Nielsen, G. Vienne, J. R. Folkenberg, and A. Bjarklev, "Investigation of microdeformation-induced attenuation spectra in a photonic crystal fiber," Optics Letters **28**(4), 236–238 (2003).

[25] M. D. Nielsen, N. A. Mortensen, and J. R. Folkenberg, "Reduced microdeformation attenuation in large-mode-area photonic crystal fibers for visible applications," Optics Letters **28**(18), 1645–1647 (2003).

[26] "TIA-455-80-C," (2003). Measurement Methods and Test Procedures – Cut-off Wavelength.

[27] A. Ghatak and K. Thyagarajan, *Introduction to fiber optics* (Cambridge University Press, 1998).

[28] J. W. Nicholson, A. D. Yablon, S. Ramachandran, and S. Ghalmi, "Spatially and spectrally resolved imaging of modal content in large-mode-area fibers," Optics Express **16**(10), 7233–7243 (2008).

[29] J. P. Koplow, D. A. V. Kliner, and L. Goldberg, "Single-mode operation of a coiled multimode fiber amplifier," Optics Letters **25**(7), 442–444 (2000).

[30] R. D. Meade, A. M. Rappe, K. D. Brommer, J. D. Joannopoulos, and O. L. Alerhand, "Accurate theoretical analysis of photonic band-gap materials," Physical Review B **48**(11), 8434–8437 (1993).

[31] N. M. Litchinitser, S. C. Dunn, B. Usner, B. J. Eggleton, T. P. White, R. C. McPhedran, and C. M. de Sterke, "Resonances in microstructured optical waveguides," Optics Express **11**(10), 1243–1251 (2003).

[32] K. J. Rowland, S. A. V., and T. M. Monro, "Bandgaps and antiresonances inintegrated-ARROWs and Bragg fibers;a simple model," Optics Express **16**(22), 17,935–17,951 (2008).

[33] D. Penninckx and N. Beck, "Definition, meaning, and measurement of the polarization extinction ratio of fiber-based devices," Applied Optics **44**(36), 7773–7779 (2005).

[34] E. Snitzer, H. Po, F. Hakimi, R. Tumminelli, and B. McCollum, "DOUBLE CLAD, OFFSET CORE Nd FIBER LASER," in *Optical Fiber Sensors*, p. PD5 (Optical Society of America, 1988).

[35] V. A. Bhagavatula, R. J. Bhat, G. E. Berkey, X. Chen, M. J. Dejneka, M. T. Gallagher, L. C. Hughes, K. W. Koch, J. Koh, M. Li, V. X. Liu, D. A. Nolan, H. M. Rasmussen, C. L. Tennent, N. Venkataraman, D. T. Walton, J. Wang, C. Zah, and L. A. Zenteno, "Progress in high-power fiber lasers," in *Fiber Lasers: Technology, Systems, and Applications*, L. N. Durvasula, ed., vol. 5335, pp. 210–216 (SPIE, 2004).

[36] J. LeGrange, E. Vogel, K. Quoi, D. Digiovanni, A. Hale, R. Pedrazzani, T. Strasser, and M. LuValle, "Optical reliability of cladding pump fiber for high power communication networks," in *Military Communications Conference Proceedings, 1999. MILCOM 1999. IEEE*, vol. 1, pp. 690 – 693 (1999).

[37] W. J. Wadsworth, R. M. Percival, G. Bouwmans, J. C. Knight, T. A. Birks, T. D. Hedley, and P. S. J. Russell, "Very high numerical aperture fibers," IEEE Photonics Technology Letters **16**(3), 843–845 (2004).

[38] J. Limpert, T. Schreiber, A. Liem, S. Nolte, H. Zellmer, T. Peschel, V. Guyenot, and A. Tünnermann, "Thermo-optical properties of air-clad photonic crystal fiber lasers in high power operation," Optics Express **11**(22), 2982–2990 (2003).

[39] M. J. F. Digonnet, *Rare-earth-doped fiber lasers and amplifiers* (Marcel Dekker, 2001).

[40] R. Paschotta, J. Nilsson, A. Tropper, and D. Hanna, "Ytterbium-doped fiber amplifiers," IEEE Journal of Quantum Electronics **33**(7), 1049–1056 (1997).

[41] A. Tünnermann, T. Schreiber, F. Röser, A. Liem, S. Höfer, H. Zellmer, S. Nolte, and J. Limpert, "The renaissance and bright future of fibre lasers," Journal of Physics B: Atomic, Molecular and Optical Physics **38**(9), S681 (2005).

[42] P. Moulton, G. Rines, E. Slobodtchikov, K. Wall, G. Frith, B. Samson, and A. Carter, "Tm-Doped Fiber Lasers: Fundamentals and Power Scaling," IEEE Journal of Selected Topics in Quantum Electronics, **15**(1), 85–92 (2009).

[43] H. Pask, R. Carman, D. Hanna, T. ropper, C. Mackechnie, P. Barber, and J.M.Dawes, "Ytterbium-doped silica fiber lasers: versatile sources for the 1-1.2 μm region," IEEE Journal of Selected Topics in Quantum Electronics **1**(1), 2–13 (1995).

[44] K. Lu and N. K. Dutta, "Spectroscopic properties of Yb-doped silica glass," Journal of Applied Physics **91**(21), 576–581 (2002).

[45] A. S. Kurkov, V. M. Paramonov, and O. I. Medvedkov, "Ytterbium fiber laser emitting at 1160 nm," Laser Physics Letters **3**(10), 503–506 (2006).

[46] G. P. Agrawal, *Nonlinear fiber optics* (Elsevier, 2007).

[47] C. Robin, I. Dajani, C. Vergien, C. Zeringue, and T. M. Shay, "Experimental and theoretical studies of single frequency PCF amplifier with output of 400 W," in *Fiber Lasers VII: Technology, Systems, and Applications*, K. Tankala, ed., vol. 7580, p. 75801I (SPIE, 2010).

[48] J. M. Fini, M. D. Mermelstein, M. F. Yan, R. T. Bise, A. D. Yablon, P. W. Wisk, and M. J. Andrejco, "Distributed suppression of stimulated Raman scattering in an Yb-doped filter-fiber amplifier," Optics Letters **31**(17), 2550–2552 (2006).

[49] T. T. Alkeskjold, "Large-mode-area ytterbium-doped fiber amplifier with distributed narrow spectral filtering and reduced bend sensitivity," Optics Express **17**(19), 16,394–16,405 (2009).

[50] R. L. Farrow, D. A. V. Kliner, G. R. Hadley, and A. V. Smith, "Peak-power limits on fiber amplifiers imposed by self-focusing," Optics Letters **31**(23), 3423–3425 (2006).

[51] B. Pedersen, A. Bjarklev, P. ovlsen, K. Dybdal, and C. Larsen, "The design of erbium-doped fiber amplifiers," Journal of Lightwave Technology **9**(9), 1105–1112 (1991).

[52] S. Magne, Y. Ouerdane, M. Druetta, J. Goure, P. Ferdinand, and G. Monnom, "Cooperative luminescence in an ytterbium-doped silica fibre," Optics Communications **111**(3–4), 310–316 (1994).

[53] K. E. Mattsson, S. N. Knudsen, B. Cadier, and T. Robin, "Photo darkening in ytterbium co-doped silica material," in *Fiber Lasers V: Technology, Systems, and Applications*, J. Broeng and C. H. III, eds., vol. 6873, p. 68731C (SPIE, 2008).

[54] M. Engholm and L. Norin, "Preventing photodarkening in ytterbium-doped high power fiber lasers;correlation to the UV-transparency of the core glass," Optics Express **16**(2), 1260–1268 (2008).

[55] K. E. Mattsson and J. Broeng, "Photo darkening of ytterbium cw fiber lasers," in *Fiber Lasers VI: Technology, Systems, and Applications*, D. V. Gapontsev, D. A. Kliner, J. W. Dawson, and K. Tankala, eds., vol. 7195, p. 71950V (SPIE, 2009).

[56] O. Schmidt, J. Rothhardt, F. Röser, S. Linke, T. Schreiber, K. Rademaker, J. Limpert, S. Ermeneux, P. Yvernault, F. Salin, and A. Tünnermann, "Millijoule pulse energy Q-switched short-length fiber laser," Optics Letters **32**(11), 1551–1553 (2007).

[57] T. Kitabayashi, M. Ikeda, M. Nakai, T. Sakai, K. Himeno, and K. Ohashi, "Population Inversion Factor Dependence of Photodarkening of Yb-Doped Fibers and Its Suppression by Highly Aluminum Doping," in *Optical Fiber Communication Conference and Exposition and The National Fiber Optic Engineers Conference*, p. OThC5 (Optical Society of America, 2006).

[58] Y. W. Lee, S. Sinha, M. J. F. Digonnet, R. L. Byer, and S. Jiang, "Measurement of high photodarkening resistance in heavily yb31-doped phosphate fibres," Electronics Letters **44**(1), 14–16 (2008).

[59] J. J. Koponen, M. J. Söderlund, H. J. Hoffman, and S. K. T. Tammela, "Measuring photodarkening from single-mode ytterbium doped silica fibers," Optics Express **14**(24), 11,539–11,544 (2006).

[60] S. Jetschke, S. Unger, U. Röpke, and J. Kirchhof, "Photodarkening in Yb doped fibers: experimental evidence of equilibrium states depending on the pump power," Optics Express **15**(22), 14,838–14,843 (2007).

[61] J. Koponen, M. Söderlund, H. J. Hoffman, D. A. V. Kliner, J. P. Koplow, and M. Hotoleanu, "Photodarkening rate in Yb-doped silica fibers," Applied Optics **47**(9), 1247–1256 (2008).

[62] M. A. Melkumov, I. A. Bufetov, K. S. Kravtsov, A. V. Shubin, and E. M. Dianov, "Lasing parameters of ytterbium-doped fibres doped with P_2O_5 and Al_2O_3," Quantum Electronics **34**(9), 843 (2004).

[63] I. A. Bufetov, S. L. Semenov, A. F. Kosolapov, M. A. Melkumov, V. V. Dudin, B. I. Galagan, B. I. Denker, V. V. Osiko, S. E. Sverchkov, and E. M. Dianov, "Ytterbium fibre laser with a heavily Yb^{3+}-doped glass fibre core," Quantum Electronics **36**(3), 189 (2006).

[64] J. K. Sahu, S. Yoo, A. J. Boyland, A. Webb, C. Codemard, R. J. Standish, and J. Nilsson, "Ytterbium-Doped Low-NA P-Al-Silicate Large-Mode-Area Fiber for High Power Applications," in *Conference on Lasers and Electro-Optics*, p. CTuP3 (Optical Society of America, 2010).

[65] M. Engholm, P. Jelger, F. Laurell, and L. Norin, "Improved photodarkening resistivity in ytterbium-doped fiber lasers by cerium codoping," Optics Letters **34**(8), 1285–1287 (2009).

[66] N. A. Mortensen, "Air-clad fibers: pump absorption assisted by chaotic wave dynamics?" Optics Express **15**(14), 8988–8996 (2007).

[67] M. Åslund, S. Jackson, J. Canning, A. Teixeira, and K. Lyytikäinen-Digweed, "The influence of skew rays on angular losses in air-clad fibres," Optics Communications **262**(1), 77–81 (2006).

[68] Y. Li, S. D. Jackson, and S. Fleming, "High absorption and low splice loss properties of hexagonal double-clad fiber," IEEE Photonics Technology Letters **16**(11), 2502–2504 (2004).

[69] L. Philippe, V. Doya, R. Philippe, P. Dominique, M. Fabrice, and L. Olivier, "Experimental study of pump power absorption along rare-earth-doped double clad optical fibres," Optics Communications **218**(4-6), 249 – 254 (2003).

[70] H. Zellmer, A. Tünnermann, H. Welling, and V. Reichel, "Double-Clad Fiber Laser with 30 W Output Power," in *Optical Amplifiers and Their Applications*, p. FAW18 (Optical Society of America, 1997).

[71] D. Marcuse, *Principles of Optical Fibre Measurement* (Academic Press, New York, 1981).

[72] J. Broeng, G. Vienne, A. Petersson, P. M. W. Skovgaard, J. R. Folkenberg, M. D. Nielsen, C. Jakobsen, H. Simonsen, and N. A. Mortensen, "Air-clad photonic crystal fibers for high-power single-mode lasers," in *Fiber Lasers: Technology, Systems, and Applications*, L. N. Durvasula, ed., vol. 5335, pp. 192–201 (SPIE, 2004).

[73] B. G. Ward, "Bend performance-enhanced photonic crystal fibers with anisotropic numerical aperture," Optics Express **16**(12), 8532–8548 (2008).

[74] J. M. Fini, "Bend-compensated design of large-mode-area fibers," Optics Letters **31**(13), 1963–1965 (2006).

[75] O. Lumholt, S. Agger, T. T. Alkeskjold, K. B. Bing, M. Denninger, and T. Nikolajsen, "High power fsed pump/signal combiner for reverse pumping of active double clad fibers," in *Fiber Lasers V: Technology, Systems, and Applications*, vol. 6873, pp. xxix–xxxii (SPIE, 2008).

[76] F. D. Teodoro and C. D. Brooks, "Fiber sources reach multimegawatt peak power in *ns* pulses," (2006). *http://www.lfw-digital.com/lfw/200611/templates/pageviewer_print?pg=96&pm=5*.

[77] J. Limpert, F. Roser, D. Schimpf, E. Seise, T. Eidam, S. Hadrich, J. Rothhardt, C. Misas, and A. Tunnermann, "High Repetition Rate Gigawatt Peak Power Fiber Laser Systems: Challenges, Design, and Experiment," IEEE Journal of Selected Topics in Quantum Electronics **15**(1), 159–169 (2009).

[78] J. Boullet, Y. Zaouter, R. Desmarchelier, M. Cazaux, F. Salin, J. Saby, R. Bello-Doua, and E. Cormier, "High power ytterbium-doped rod-type three-level photonic crystal fiber laser," Optics Express **16**(22), 17,891–17,902 (2008).

[79] F. Röser, T. Eidam, J. Rothhardt, O. Schmidt, D. Schimpf, J. Limpert, and A. Tünnermann, "Millijoule pulse energy high repetition rate femtosecond fiber CPA system," in *Advanced Solid-State Photonics*, p. TuA5 (Optical Society of America, 2008).

[80] S. Wielandy, "Beam Quality and Modal Content for LMA Fiber Sources," in *Conference on Lasers and Electro-Optics/Quantum Electronics and Laser Science Conference and Photonic Applications Systems Technologies*, p. CTuS4 (Optical Society of America, 2007).

[81] J. Bromage, C. Dorrer, M. J. S. III, and J. D. Zuegel, "Optimizing Injection into Large-Mode-Area Photonic Crystal-Fiber Amplifiers by Spatially Resolved Spectral Interferometry," in *Conference on Lasers and Electro-Optics/International Quantum Electronics Conference*, p. CWD3 (Optical Society of America, 2009).

[82] C. B. Olausson, C. I. Falk, J. K. Lyngsø, B. B. Jensen, K. T. Therkildsen, J. W. Thomsen, K. P. Hansen, A. Bjarklev, and J. Broeng, "Amplification and ASE suppression in a polarization-maintaining ytterbium-doped all-solid photonic bandgap fibre," Optics Express **16**(18), 13,657–13,662 (2008).

[83] C. B. Olausson, A. Shirakawa, H. Maruyama, K. Ueda, J. K. Lyngsø, and J. Broeng, "Power-scalable long-wavelength Yb-doped photonic bandgap fiber sources," in *Fiber Lasers VII: Technology, Systems, and Applications*, K. Tankala, ed., vol. 7580, p. 758013 (SPIE, 2010).

[84] C. B. Olausson, L. Scolari, L. Wei, D. Noordegraaf, J. Weirich, T. T. Alkeskjold, K. P. Hansen, and A. Bjarklev, "Electrically tunable Yb-doped fiber laser based on a liquid crystal photonic bandgap fiber device," Optics Express **18**(8), 8229–8238 (2010).

[85] J. Ota, A. Shirakawa, and K. Ueda, "High-Power Yb-Doped Double-Clad Fiber Laser Directly Operating at 1178 nm," Japanese Journal of Applied Physics **45**(4), L117–L119 (2006).

[86] S. Sinha, C. Langrock, M. J. Digonnet, M. M. Fejer, and R. L. Byer, "Efficient yellow-light generation by frequency doubling a narrow-linewidth 1150 nm ytterbium fiber oscillator," Optics Letters **31**(3), 347–349 (2006).

[87] H. Maruyama, A. Shirakawa, and K. Ueda, "1178nm linearly-polarized all fiber laser," in *Conference on Lasers and Electro-Optics/Pacific Rim 2007*, p. TuA4_3 (Optical Society of America, 2007).

[88] A. S. Kurkov, "Oscillation spectral range of Yb-doped fiber lasers," Laser Physics Letters **4**(2), 93–102 (2007).

[89] M. P. Kalita, S. Alam, C. Codemard, S. Yoo, A. J. Boyland, M. Ibsen, and J. K. Sahu, "Multi-watts narrow-linewidth all fiber Yb-doped laser operating at 1179 nm," Optics Express **18**(6), 5920–5925 (2010).

[90] A. Shirakawa, H. Maruyama, K. Ueda, C. B. Olausson, J. K. Lyngsø, and J. Broeng, "High-power Yb-doped photonic bandgap fiberamplifier at 1150-1200 nm," Optics Express **17**(2), 447–454 (2009).

[91] V. Pureur, L. Bigot, G. Bouwmans, Y. Quiquempois, M. Douay, and Y. Jaouen, "Ytterbium-doped solid core photonic bandgap fiber for laser operation around 980 nm," Applied Physics Letters **92**(6), 061113 (pages 3) (2008).

[92] R. Goto, K. Takenaga, K. Okada, M. Kashiwagi, T. Kitabayashi, S. Tanigawa, K. Shima, S. Matsuo, and K. Himeno, "Cladding-Pumped Yb-Doped Solid Photonic Bandgap Fiber for ASE Suppression in Shorter Wavelength Region," in *Optical Fiber Communication Conference and Exposition and The National Fiber Optic Engineers Conference*, p. OTuJ5 (Optical Society of America, 2008).

[93] A. Isomäki and O. G. Okhotnikov, "Femtosecond soliton mode-locked laser based on ytterbium-doped photonic bandgap fiber," Optics Express **14**(20), 9238–9243 (2006).

[94] S. Février, D. D. Gaponov, P. Roy, M. E. Likhachev, S. L. S., M. M. Bubnov, E. M. Dianov, M. Y. Yashkov, V. F. Khopin, M. Y. Salganskii, and A. N. Guryanov, "High-power photonic-bandgap fiber laser," Optics Letters **33**(9), 989–991 (2008).

[95] A. Wang, A. K. George, and J. C. Knight, "Three-level neodymium fiber laser incorporating photonic bandgap fiber," Optics Letters **31**(10), 1388–1390 (2006).

[96] K. P. Hansen, C. B. Olausson, J. Broeng, K. Mattsson, M. D. Nielsen, T. Nikolajsen, P. M. W. Skovgaard, M. H. S. rensen, M. Denninger, C. Jakobsen, and H. R. Simonsen, "Airclad fiber laser technology," in *Fiber Lasers V: Technology, Systems, and Applications*, J. Broeng and C. H. III, eds., vol. 6873, p. 687307 (SPIE, 2008).

[97] J. K. Lyngsø, B. J. Mangan, and P. J. Roberts, "Polarization Maintaining Hybrid TIR/Bandgap All-Solid Photonic Crystal Fiber," in *Conference on Lasers and Electro-Optics/Quantum Electronics and Laser Science Conference and Photonic Applications Systems Technologies*, p. CThV1 (Optical Society of America, 2008).

[98] A. Shirakawa, H. Maruyama, K. Ueda, C. B. Olausson, J. K. Lyngsø, and J. Broeng, "30W, 1178nm Yb-Doped Photonic Bandgap Fiber Amplifier," in *Conference on Lasers and Electro-Optics/International Quantum Electronics Conference*, p. CThGG3 (Optical Society of America, 2009).

[99] T. A. Birks, F. Luan, G. J. Pearce, A. Wang, J. C. Knight, and D. M. Bird, "Bend loss in all-solid bandgap fibres," Optics Express **14**(12), 5688–5698 (2006).

[100] A. Argyros, T. Birks, S. Leon-Saval, C. M. B. Cordeiro, and P. S. J. Russell, "Guidance properties of low-contrast photonic bandgap fibres," Optics Express **13**(7), 2503–2511 (2005).

[101] T. Murao, K. Saitoh, and M. Koshiba, "Detailed theoretical investigation of bending properties in solid-core photonic bandgap fibers," Optics Express **17**(9), 7615–7629 (2009).

[102] H. Maruyama, A. Shirakawa, K. Ueda, C. B. Olausson, J. K. Lyngsø, and J. Broeng, "1178 nm all Yb-fiber laser source power-scaled by solid-core photonic bandgap fiber for 589nm generation," in *Lasers and Electro-Optics 2009 and the European Quantum Electronics Conference. CLEO Europe - EQEC 2009. European Conference on*, pp. 1 –1 (2009).

[103] S. V. Tovstonog, S. Kurimura, I. Suzuki, K. Takeno, S. Moriwaki, N. Ohmae, N. Mio, and T. Katagai, "Thermal effects in high-power CW second harmonic generation in Mg-doped stoichiometric lithium tantalate," Optics Express **16**(15), 11,294–11,299 (2008).

[104] S. C. Kumar, G. K. Samanta, and M. Ebrahim-Zadeh, "High-power, single-frequency, continuous-wave second-harmonic-generation of ytterbium fiber laser in PPKTP and MgO:sPPLT," Optics Express **17**(16), 13,711–13,726 (2009).

[105] Y. Feng, L. R. Taylor, and D. B. Calia, "25 W Raman-fiber-amplifier-based 589 nm laser for laser guide star," Optics Express **17**(21), 19,021–19,026 (2009).

[106] C. B. Olausson, J. K. Lyngsø, J. Broeng, H. Maruyama, and A. Shirakawa, "FIBER AMPLIFIERS: Photonic-bandgap fiber amplifier reaches for the stars," (2009). *http://www.optoiq.com/index/photonics-technologies-applications/lfw-display/lfw-article-display/articles/optoiq2/photonics-technologies/technology-products/fiber-optics/communications-systems/2009/12/fiber-amplifiers-photonic-bandgap-fiber-amplifier-reaches-for-the-stars.html*.

[107] S. Gauza, C. Wen, S. Wu, N. Janarthanan, and C. Hsu, "Super High Birefringence Isothiocyanato Biphenyl-Bistolane Liquid Crystals," Japanese Journal of Applied Physics **43**(11A), 7634–7638 (2004).

[108] S. Wu, Q. Zhang, and S. Marder, "High Dielectric Dopants for Low Voltage Liquid Crystal Operation," Japanese Journal of Applied Physics **37**(Part 2, No. 10B), L1254–L1256 (1998).

[109] B. Eggleton, C. Kerbage, P. Westbrook, R. Windeler, and A. Hale, "Microstructured optical fiber devices," Optics Express **9**(13), 698–713 (2001).

[110] C. Kerbage, R. S. Windeler, B. J. Eggleton, P. Mach, M. Dolinski, and J. A. Rogers, "Tunable devices based on dynamic positioning of micro-fluids in micro-structured optical fiber," Optics Communications **204**(1–6), 179–184 (2002).

[111] R. Bise, R. S. Windeler, K. S. Kranz, C. Kerbage, and B. J. Eggleton, "Tunable photonic band gap fiber," in *Optical Fiber Communications Conference*, p. ThK3 (Optical Society of America, 2002).

[112] T. Larsen, A. Bjarklev, D. Hermann, and J. Broeng, "Optical devices based on liquid crystal photonic bandgap fibres," Optics Express **11**(20), 2589–2596 (2003).

[113] M. W. Haakestad, T. T. Alkeskjold, M. D. Nielsen, L. Scolari, J. Riishede, H. E. Engan, and A. Bjarklev, "Electrically tunable photonic bandgap guidance in a liquid-crystal-filled photonic crystal fiber," IEEE Photonics Technology Letters **17**(4), 819–821 (2005).

[114] L. Scolari, T. Alkeskjold, J. Riishede, A. Bjarklev, D. Hermann, A. Anawati, M. Nielsen, and P. Bassi, "Continuously tunable devices based on electrical control of dual-frequency liquid crystal filled photonic bandgap fibers," Optics Express **13**(19), 7483–7496 (2005). URL `http://www.opticsexpress.org/abstract.cfm?URI=oe-13-19-7483`.

[115] F. Du, Y. Q. Lu, and S. T. Wu, "Electrically tunable liquid-crystal photonic crystal fiber," Applied Physics Letters **85**(12), 2181–2183 (2004).

[116] T. Alkeskjold, J. Lægsgaard, A. Bjarklev, D. Hermann, A. Anawati, J. Broeng, J. Li, and S. Wu, "All-optical modulation in dye-doped nematic liquid crystal photonic bandgap fibers," Optics Express **12**(24), 5857–5871 (2004).

[117] L. Scolari, T. T. Alkeskjold, and A. Bjarklev, "Tunable Gaussian filter based on tapered liquid crystal photonic bandgap fibre," Electronics Letters **42**(22), 1270–1271 (2006).

[118] D. Noordegraaf, . Scolari, J. Lægsgaard, L. Rindorf, and T. T. Alkeskjold, "Electrically and mechanically induced long period gratings in liquid crystalphotonic bandgap fibers," Optics Express **15**(13), 7901–7912 (2007).

[119] M. N. Petersen, L. Scolari, T. Tokle, T. T. Alkeskjold, S. Gauza, S. Wu, and A. Bjarklev, "Noise filtering in a multi-channel system using a tunable liquid crystal photonic bandgap fiber," Optics Express **16**(24), 20,067–20,072 (2008).

[120] T. R. Wolinski, S. Ertman, A. Czapla, P. Lesiak, K. Nowecka, A. W. Domanski, E. Nowinowski-Kruszelnicki, R. Dabrowski, and J. Wojcik, "Polarization effects in photonic liquid crystal fibers," Measurement Science and Technology **18**(10), 3061–3069 (2007).

[121] T. R. Wolinski, A. Czapla, S. Ertman, M. Tefelska, A. W. Domanski, E. Nowinowski-Kruszelnicki, and R. Dabrowski, "Tunable highly birefringent solid-core photonic liquid crystal fibers," Optical and Quantum Electronics **39**(12–13), 1021–1032 (2007).

[122] D. Zografopoulos, E. E. Kriezis, and T. D. Tsiboukis, "Tunable highly birefringent bandgap-guiding liquid-crystal microstructured fibers," Journal of Lightwave Technology **24**(9), 3427–3432 (2006).

[123] L. Wei, W. Xue, Y. Chen, T. T. Alkeskjold, and A. Bjarklev, "Optically fed microwave true-time delay based on a compact liquid-crystal photonic-bandgap-fiber device," Optics Letters **34**(18), 2757–2759 (2009).

[124] L. Wei, E. Khomtchenko, T. T. Alkeskjold, and A. Bjarklev, "Photolithography of thick photoresist coating for electrically controlled liquid crystal photonic bandgap fibre devices," Electronics Letters **45**(6), 326–327 (2009).

[125] L. Wei, T. T. Alkeskjold, and A. Bjarklev, "Compact Design of an Electrically Tunable and Rotatable Polarizer Based on a Liquid Crystal Photonic Bandgap Fiber," IEEE Photonics Technology Letters **21**(21), 1633–1635 (2009).

[126] D. Noordegraaf, M. D. Nielsen, P. M. Skovgaard, S. Agger, K. P. Hansen, J. Broeng, C. Jakobsen, H. R. Simonsen, and J. Lægsgaard, "Pump Combiner for Air-Clad Fiber with PM Single-Mode Signal Feed-through," in *Conference on Lasers and Electro-Optics/International Quantum Electronics Conference*, p. CThGG6 (Optical Society of America, 2009).

[127] J. Weirich, J. Lægsgaard, L. Scolari, L. Wei, T. T. Alkeskjold, and A. Bjarklev, "Biased liquid crystal infiltrated photonic bandgap fiber," Optics Express **17**(6), 4442–4453 (2009).

[128] J. Weirich, J. Lægsgaard, L. Wei, T. T. Alkeskjold, T. X. Wu, S. Wu, and A. Bjarklev, "Liquid crystal parameter analysis for tunable photonic bandgap fiber devices," Optics Express **18**(5), 4074–4087 (2010).